FINDING NEW EQUILIBRIA: DIRECTED SYNTHESIS OF LANTHANIDE MATERIALS VIA SODIUM AZIDE MEDIATED PATHWAYS.

by

BRIAN FREEMAN MOORE

A Dissertation submitted to the

Graduate School- New Brunswick

Rutgers, The State University of New Jersey

in partial fulfillment of the requirements

for the degree of

Doctor of Philosophy

Graduate Program in Chemistry & Chemical Biology

written under the direction of

Professor John G. Brennan

and approved by

_____

_____

_____

_____

New Brunswick, New Jersey

May 2013

ABSTRACT OF THE DISSERTATION

FINDING NEW EQUILIBRIA: DIRECTED SYNTHESIS OF LANTHANIDE MATERIALS VIA SODIUM AZIDE MEDIATED PATHWAYS

by BRIAN FREEMAN MOORE

Dissertation Director:

Professor John G. Brennan

This dissertation covers the synthesis and characterization of three unique classes of lanthanide materials produced exclusively by the addition of sodium azide (NaN_3) into solution based lanthanide reactions. The products were achieved through transmetallation and redox reactions between rare earth chalcogenolate reagents ($Ln_x(EPh)_y$), NaN_3 and elemental chalcogenides (E = O, S, Se, Te). The products displayed atypical structural and physical properties including; unique coordination geometries, high nuclearities, tunable detonation/deflagration, strong NIR emissions, and unexpected magnetic ordering behaviors.

The introduction of NaN_3, Na_2O, Cd, elemental Se and Te into $Ln(EPh)_2$ and $Ln(EPh)_3$ pyridine (py) solutions led to the production of $(py)_2Na_2(EPh)_2$ and 5 structurally distinct azide encapsulated rare earth clusters; $(Py)_{10}Sm_6O_2(N_3)_{16}Na_2$, $(py)_8Ln_6O_2(N_3)_{12}(SePh)_2$, $(py)_{10}Ln_6O_2(Se_2)_2(N_3)_{10}$ (Ln=Er, Ho), and $(py)_{16}Sm_8Se(O_2)Na_2(Te_2)_6(N_3)_8$. Each system was

encapsulated by varieties of azide bridging moieties, while exhibiting a [Ln]/[N_3] dependent correlation with detonation and deflagration temperatures.

The inclusion of NaN_3 in $Ln(SePh)_3$ pyridine solutions with elemental Se, led to the discovery of the $(py)_{16}Ln_{17}NaSe_{18}(SePh)_{16}$; (Ln= Ce, Pr, and Nd). Emission studies of the Nd_{17} analogue, revealed a 35% quantum efficiency for the $^4F_{3/2}$ - $^4I_{11/2}$ transition (1070 nm emission), and a near solid state emission intensity for the $^4F_{3/2} \rightarrow {}^4I_{15/2}$ transition (1822 nm emission).

The novel $Eu(EPh)_4Na_2$•2DME; (E=S,Se), specimens were synthesized by the combination of $Eu(EPh)_2$ with NaN_3 in dimethoxyethane (DME). The europium coordination sphere was solvent free and resembles the coordinations of europium monochalcogenides (EuE). Comparative structural analysis and magnetic susceptibility studies of the Eu^{3+} product, $((py)_6Eu_2(\mu_4\text{-}S_2)_2(OC_6F_5)_2)$ revealed paramagnetic ordering at low temperature for $Eu(EPh)_4Na_2$•2DME; (E=S,Se), while ferrimagnetic ordering was found for $((py)_6Eu_2(\mu_4\text{-}S_2)_2(OC_6F_5)_2)$. All materials exhibited antiferromagnetic ordering above 50 K, while a Curie temperature of 18.0 K was determined for $((py)_6Eu_2(\mu_2\text{-}S_2)^{2-}(OC_6F_5)_2)$.

DEDICATION

To my father Dr. George E. Moore and my son Enzo A. Moore, I hope you two are proud of me.

ACKNOWLEDGEMENTS

To my advisor Prof. John Brennan, thank you for your patience, guidance, encouragement and wisdom through my Phd process. I recognize that I am a bit of live wire and always will be, but you allowed me to find my own way, in my own time, and on my own terms, and for that I am eternally grateful.

I would like to thank my committee, Dr. Edward Castner, Dr. Jing Li, and Dr. Richard Riman. Thank you for your perspectives, guidance and willingness to help me navigate my career, as well as serve on my committee. I could not have asked for better professional role models.

The crystallographer extraordinaire, Dr. Thomas Emge there is no question, without your help, and patience this work would not have been possible. However, what I appreciate most is our conversations on martial arts, life and crystallography. You have been a great mentor, and friend, my deepest thanks.

Dr. Eric Garfunkel, the unofficial fifth member of my committee. You gave me a chance to fulfill a life goal in South Africa, and taught me some profound lessons about the business and politics of science. it has been an sincere pleasure to learn and work with you.

I did not expect to find a brother in graduate school, I was wrong. Dr. Joseph Cuisick you made this road alot smoother and funnier. I hope i've done the same for you.

Dr. Michael Romanelli, Dr. Lisa Veliath-Houston, Dr. Gordan T. Reeves, Kieran Norton, and Melissa Davis, thank you for your assistance and support, and all of our off the wall conversations, workouts, happy hours, get togethers and road trips it has been a blast.

To my wife Joy, thank you for all your love, support, encouragement and sacrifices, while I pursued this dream. This moment would not have been possible or complete without you to share it with. I look forward to spending the rest of my life showing how much I've appreciated you being here for me.

To my parents, Dr. George E. Moore and Dianne Freeman-Moore thank you for all of your support, love, and patience as I found my way. I know I did not make it easy on you, but I couldn't have done any of this with you two...literally and figuratively, I love you both very much. To my sister Adrienne I love you very much and now that sanity has returned expect my teasing, and brotherly harassment to resume. To Grandma Sophie, every one needs an pillar of strength to emulate mine just happened to be a short, fast talking, no nonsense lady from NYC, and I wouldn't have it any other way, you are the best there is , there was or will be. I love you.

Lastly, to Dr. Michael J. Prushan and Dr. Richard Didio, you opened the doors and gave me the chance to have the career and life I wanted. I am forever in your debt.

Table of Contents

List of Tables

List of Illustrations

List of Abbreviations

Cp	C_5H_5
Cp*	$(C_5Me_5)^-$
Py or py	C_5H_5N
THF	C_4H_8O
DME	$C_4H_{10}O_2$
Ph	C_6H_5
SePh	SeC_6H_5
SPh	SC_6H_5
TePh	TeC_6H_5
DETA	$C_4H_{13}N_3$
μ_x	Coordinated to X number of species
Å	Angstrom
K	Kelvin
SMM	Single Molecular Magnet
EO	End Only
EE	End to End
QE	Quantum Efficiency
ORTEP	Oak Ridge Thermal Ellipsoid Plot Program
POV-Ray	Persistence of Vision Raytracer
NIR	Near Infrared Red
EPh	Chalcogenolate

E	Chalcogenide (S-Te)
R	Alkyl
^{o}C	Celsius
S_2CNEt_2	$S_2CN(CH_2)_4$
HSAB	Hard and Soft Acid and Base
τ_{fl}	Fluorescence Decay Lifetime
τ_{rad}	Radiative Lifetime
ΔE	Change in Energy
Oe	Oersted

Introduction

Once described as "boring"[1] and "predictable" the chemistry of the lanthanide series has led to a wave of new discoveries that capitalized on their unique coordination motifs, reactive oxidation states and distinct electronic structures. In fact, the development of a whole host of next generation materials owe their utility to the lanthanides. For example, the replacement of radioactive thorium with cerium and lanthanum oxide in tungsten arc welding electrodes, has led to greater material performance (slower electrode consumption or "burnoff") and lowered health risks for professionals due to thorium dust inhalation.[2]

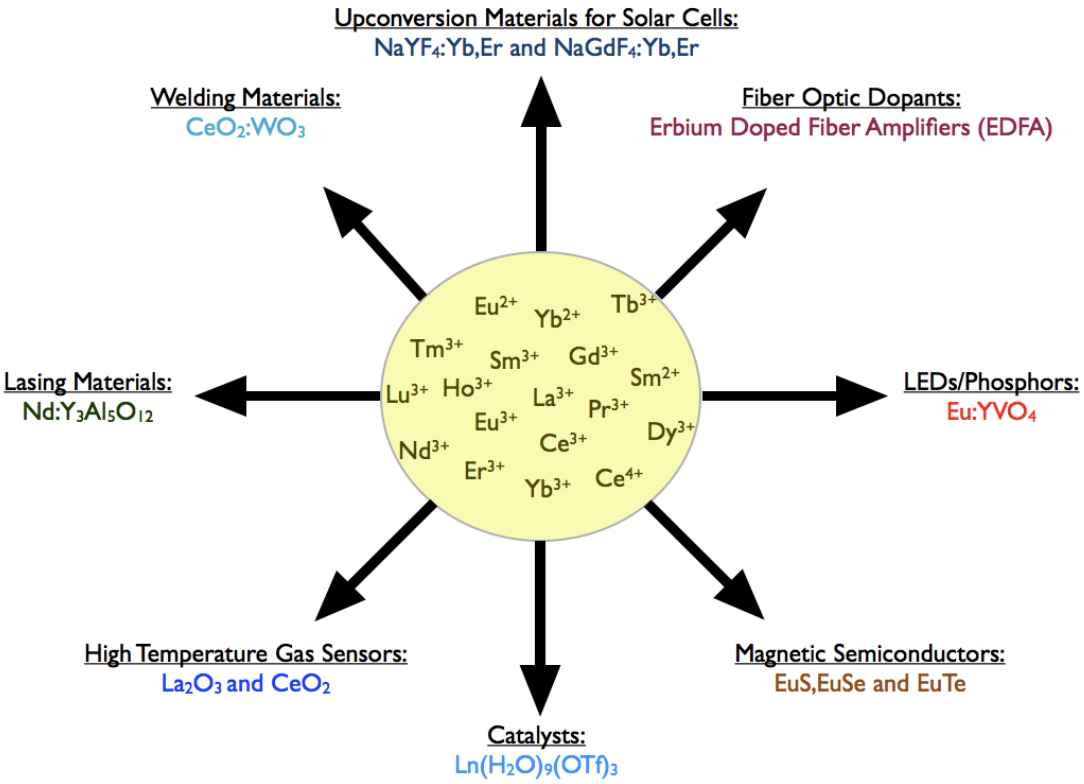

Figure I.1. Lanthanide Based Materials and Applications.

From phosphors[3] and catalysts[4] to molecular magnets[5] and chemical sensors[6] the "eccentric" chemistry of the lanthanides has found its way into applications

that are both extraordinary and diverse. This renewed interest has highlighted the need for more varied synthetic methods and a more comprehensive understanding of lanthanide chemistry in order to accommodate the complexity of new material demands.

The unique atomic structure of the rare earth metals is at the heart of their uncommon chemistry. The valence shell of the lanthanides (4f orbitals) is not the most radially extended orbitals from the nucleus In contrast to the other elements. This phenomenon results in the 4f orbitals being "shielded" by the filled $5s^2$ and $5p^6$ orbitals. Figure I.2 is a plot of the radial portion of the Nd^{3+} Schrödinger equation for 4f, 5s & 5p orbitals. The plot shows a greater probability of finding the 4f orbitals closer to the nucleus than the 5s and 5p. Consequently, the unoccupied 5d and 6s orbitals become the outermost frontier (Figure I.3). These combined phenomena result in a valence shell with a spherical electron density and virtually no potential for orbital overlap in bonding. Subsequently, this explains why lanthanide bonding is largely ionic in nature.

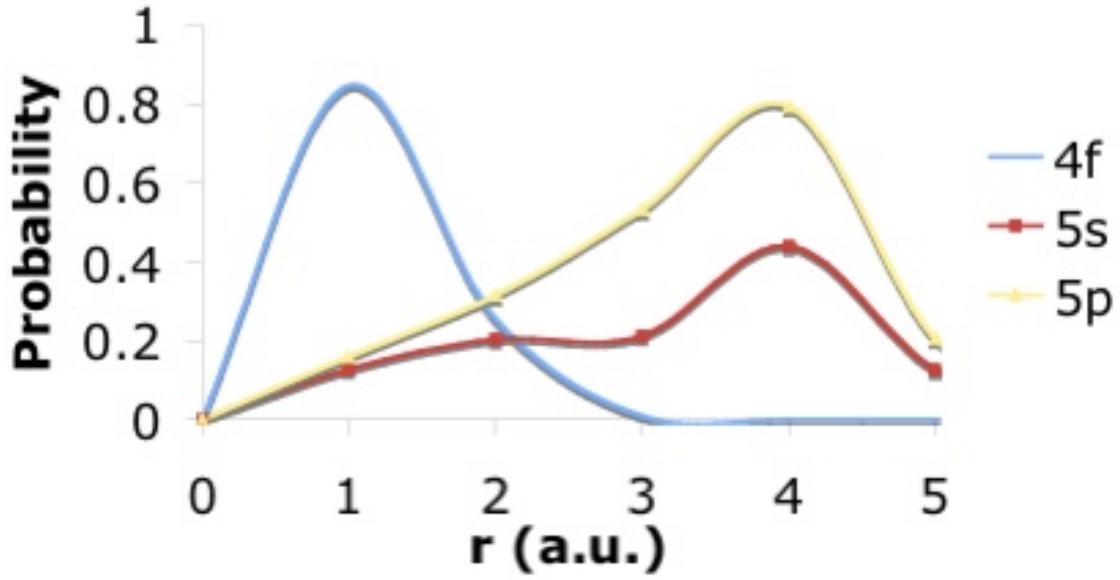

Figure I.2. Plot of Radial Functions of Nd^{3+} for 4f, 5s &5p Orbitals.

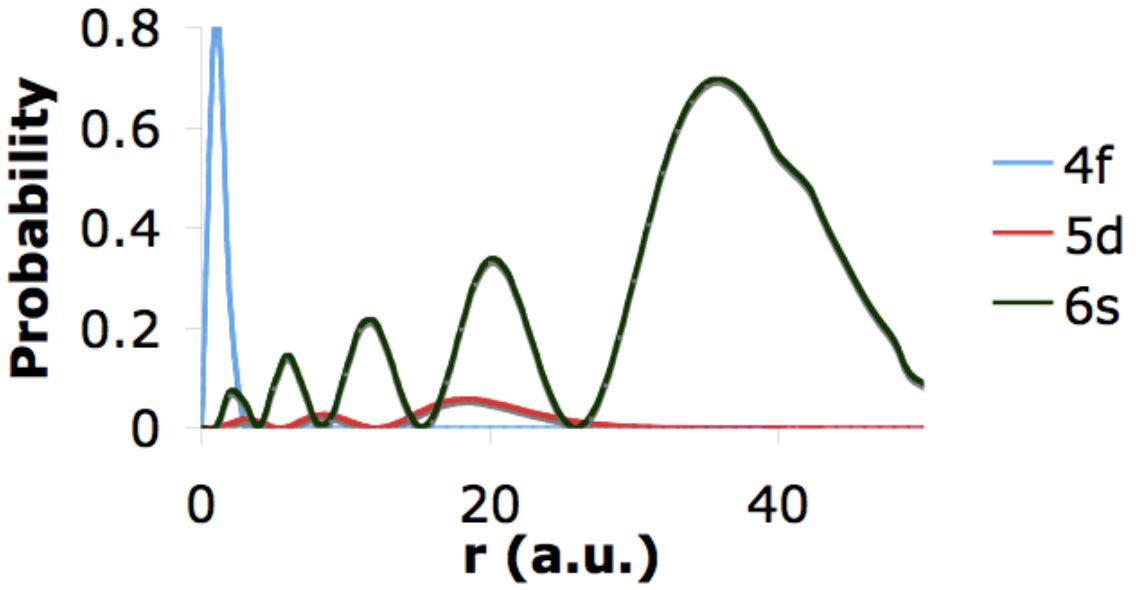

Figure I.3: Plot of Radial Distribution Functions for Nd^{3+} for 4f, 5d and 6s Orbitals.

The 4f orbital's inability to effectively shield and the electronic configuration of the series explain the characteristic dominance of the 3^{+}

oxidation state and decreasing ionic radii across the series (lanthanide contraction). 4f orbital electrons have been described as notoriously poor shielders.[7] This notion is supported in Figures I.2-I.3, by the 5s, 5p, 5d and 6s penetration of the 4f probability maxima. As a result, orbital electrons whose maxima overlap with 4f experience a greater effective nuclear charge manifesting as a reduction in ionic radii. Simultaneously, the electronic configuration of the lanthanides with their radially extended filled 6s orbitals and low ionization energies[8] (1st Ionization: 5.46-6.25 ev; 2nd Ionization : 10.5 -13.9 ev) readily lose their first two electrons. Further Ionizations originating from the 4f orbitals (3rd Ionization: 19.17-25.1 ev; 4th Ionization: 39.37-49.95 ev) donate only one electron. There are exceptions to the 3^+ preference as europium, samarium and ytterbium commonly take on a 2^+ oxidation state while a 4^+ oxidation state for cerium has been observed.[9] The observation of these alternate oxidation states can be justified by the relative stability of the half-filled and full shell electron configurations in the elements (Table I.1).[10]

(Ln)	Electron Configuration (EC)	Electron Configuration of Ln^{3+} $(EC)^{3+}$	Ground State ($^{2S+1}L_j$)
(La)	(Xe)$5d^16s^2$	(Xe)$4f^0$	$^1S_0$
(Ce)	$4f^15d^16s^2$	$4f^1$	$^2F_{5/2}$
(Pr)	$4f^36s^2$	$4f^2$	$^3H_4$
(Nd)	$4f^46s^2$	$4f^3$	$^4I_{9/2}$
(Pm)	$4f^56s^2$	$4f^4$	$^5I_4$
(Sm)	$4f^66s^2$	$4f^5$	$^6H_{5/2}$
(Eu)	$4f^76s^2$	$4f^6$	$^7F_0$
(Gd)	$4f^75d^16s^2$	$4f^7$	$^8S_{7/2}$
(Tb)	$4f^96s^2$	$4f^8$	$^7F_6$
(Dy)	$4f^{10}6s^2$	$4f^9$	$^6H_{15/2}$
(Ho)	$4f^{11}6s^2$	$4f^{10}$	$^5I_8$
(Er)	$4f^{12}6s^2$	$4f^{11}$	$^4I_{15/2}$
(Tm)	$4f^{13}6s^2$	$4f^{12}$	$^3H_6$
(Yb)	$4f^{14}6s^2$	$4f^{13}$	$^2F_{7/2}$
(Lu)	$4f^{14}5d^16s^2$	$4f^{14}$	$^1S_0$
(Y)	(Kr)$4d^15s^2$	(Kr)	$^1S_0$

Table I.1. Lanthanide Series Electron Configurations and Ground States.

The tendency for lanthanide complexes to exhibit non-directional ionic bonding is also a byproduct of electronic shielding.The greater radial extension of filled 5s and 5p orbitals generates a repulsive and spherical electron density around every lanthanide atom. This effectively removes the influence of traditional covalent bonding considerations (orbital overlap and orientation), and leads to complexes with an array of unique properties. Higher coordination numbers (3-14 with 6-9 typically),[11] coordination spheres defined by the

electrostatic and steric nature of the incoming ligands, and a negligible crystal field effect on lanthanide energy levels are a few examples.

The ability to tune the absorption and emission properties of various mediums[12] with lanthanide species is a byproduct of the interplay between two lanthanide specific electronic/quantum properties. First, the limited crystal field effect of ligands on lanthanide 4f-orbital energy states (due to electronic shielding) results in 4f energy states that are largely unaffected by their coordination environment producing a set of narrow and discrete emission wavelengths. Second, the Laporte-forbidden f-f transitions within the subshell display very low absorption coefficients[13], and gives rise to the long excited state lifetimes observed from lanthanide emissions. The available emission range within the series extends from the ultraviolet (Gd^{3+}) and the visible (Tm^{3+}, Tb^{3+}, Eu^{2+}, Sm^{3+}) to well into the NIR region (Yb^{3+}, Nd^{3+}, Pr^{3+}, Er^{3+}). When these characteristics are combined the lanthanides' role as versatile emissive sources for a variety of hosts becomes clear.

Early lanthanide coordination chemistry utilized only two types of anions/ ligand classes. Since their discovery in 1787[14] by Johan Gadolin lanthanide ions displayed an affinity for halides and oxide containing ligands. Ores such as yttria, ceria monazite and bastnäsite all possessed structures with lanthanide oxide or lanthanide halide coordinations. Pearson[15] in effort to provide a reliable method for predicting inorganic reaction products published his HSAB theory in 1963. Halide and oxide anions were classified as hard bases and the cations that preferentially formed the most stable products with them were hard acids.

Conversely in 1954, Wilkinson[16] produced the first $Ln(C_6H_5)_3$ product. This system's use of C_6H_5 group as a stabilizer without the presence of oxide or halides was a ground breaking find. This notion grew into a variety of sterically bulkier analogues including the Cp and Cp* ligands commonly seen in lanthanide organometallic chemistry today. By imposing steric bulk, mitigating ligand-ligand repulsion, and increasing solubility in organic solvents, bulky macrocycles and polydentate ligands joined the C_6R_5 class of ligands in providing an alternate precursor to previously inaccessible lanthanide products. Nevertheless, the ease of metathesis reactions with lanthanide halide starting materials and the simplicity of their production made them a cornerstone of lanthanide coordination chemistry. The work of Evans,[17] exemplifies Cp ligand utility by expanding the reductive chemistry of the series using sterically bulky Cp and Cp* ligands to stabilize reactive lanthanide centers. These trends cemented hard bases and large ligand groups as the backbones of early rare earth coordination chemistry.

Lanthanide chalcogenide (S, Se, Te) chemistry represented an interesting and challenging departure from the more established areas of rare earth chemistry. The pairing of lanthanide cations (hard acids), with the soft chalcogenide bases was a less than ideal for producing stable products according to HSAB theory. The use of chalcogenide bonds' with significant orbital overlap dependence along side the ionic lanthanide cations provided a strong theoretical rationale for avoiding such work. However, the lack of understanding about Ln-E bonds, as well as the well known emissive properties of the rare earths, made for an enticing research pursuit.

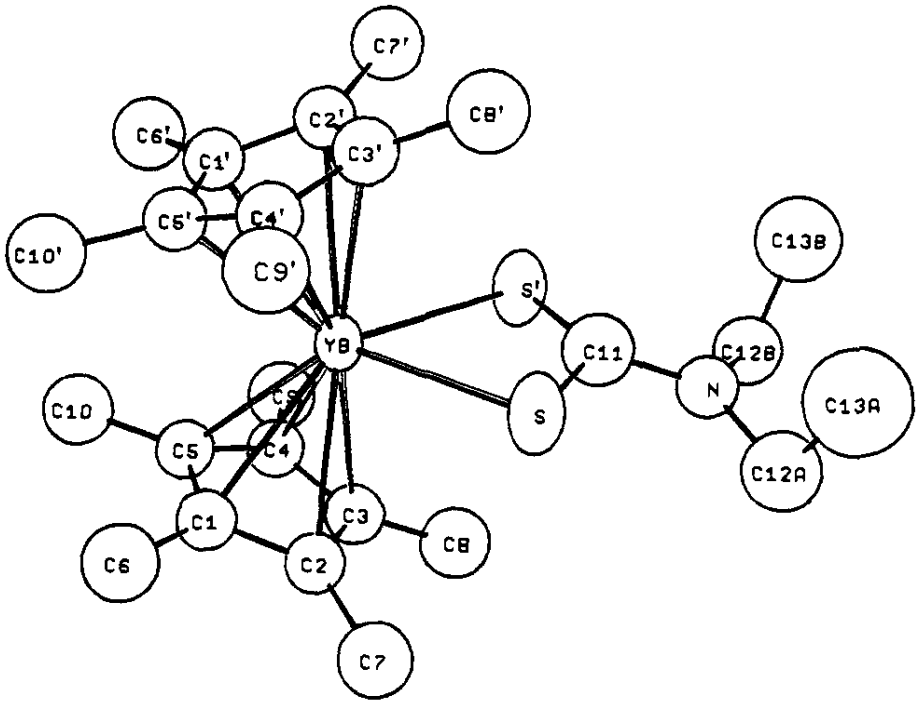

Figure I.4. Structural Image of $(Cp^*)_2Yb(S_2CNEt_2)$

In any case, approaching lanthanide chalcogenide species with bulkier ligand stabilizers and halide precursors did had their drawbacks. First, the majority of species produced contained halide impurities, even under the most meticulous reaction conditions. Second, the monomeric and dimeric structures[18] produced did little to address the nature of the Ln-E bond because of ligand-ligand repulsions dominating the structure determination. The Andersen group's, $(Cp^*)_2Yb(S_2CNEt_2)$[19] species is a clear example. Additionally these products suffered from low yield, and low purity. The first lanthanide chalcogenide cluster ever produced, $[\{(Cp^*)Sm\}_6Se_{11}]$[20], (Figure I.4) could not be fully characterized, nor could any derivatives be produced due to the above factors in the system.

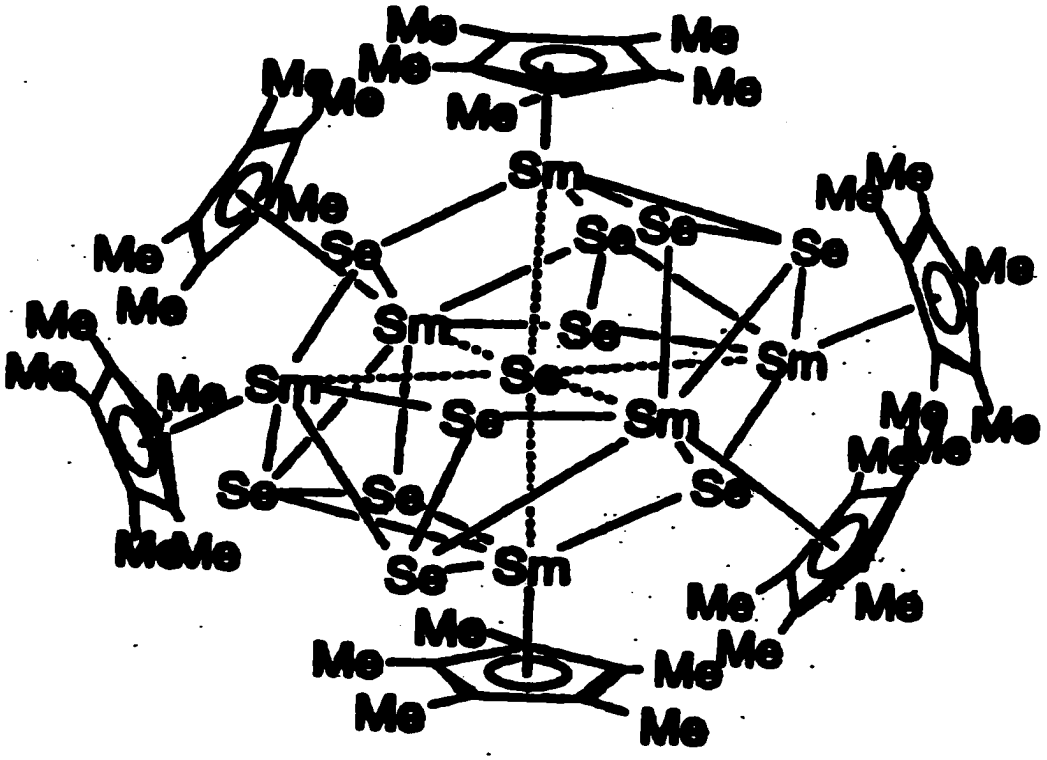

Figure I.5. Structure of [{(Cp*)Sm}$_6$ Se$_{11}$][20]

This occurred despite the presence of "stabiliizing" Cp* ligands. When the inability to completely displace halide[21] and Cp anions[22] from lanthanide systems with chalcogenides was found, the necessity for a new pathway to explore lanthanide chalcogenide chemistry became apparent.

The reaction of REER (R=C_6H_5) and rare earths in lewis base solvents (THF, DME, and Py) and catalytic amounts of mercury provided a halogen free pathway for introducing lanthanides into solution with versatile chalcogenolate anions.

$$\mathbf{Ln + 3/2\ PhEEPh \xrightarrow{Solvent/Hg} (L)_xLn(EPh)_3}$$

Scheme I.1. General Scheme for Ln(EPh)$_3$ Synthesis

The role of mercury in this reaction proceeds through two possible reaction pathways. The first involves mercury insertion into the dichalcogenide bond, and a subsequent transmetallation between the $Hg(ER)_2$ species and the lanthanide resulting in the precipitation of mercury. The second proposes the formation of a lanthanide-mercury amalgam to activate the dichalcogenide bond. The reaction can be tailored to yield a number of $Ln_x(ER)_y$ species.[23,24,25]

Product differences in nuclearity, coordination number and bridging are related to the metal ionic radii, neutral donors (solvent) and chalcogenolates used. $(py)_3Yb(SPh)_3$, $[(py)_3Ho(SPh)_3]_2$, and $[(py)_2Sm(SPh)_3]_4$ exemplify the influence of the first variable as shown by Lee[24,26]. The small Yb^{3+} ion stabilizes as a monomer with terminal thiolates while the progressively larger Ho^{3+} and Sm^{3+} ions stabilized dimer and tetramer products with bridging thiolate moieties. Beradini's synthesis of $[(THF)_3Eu(\mu\text{-}SePh)_2]_\infty$ [27] and Khasnis's $[(THF)_2Eu(TePh)_2]_\infty$[28] provide similar support for the influence of chalcogenolates on coordination numbers. Each of the Eu^{2+} centers are 7-coordinate in $[(THF)_3Eu(\mu\text{-}SePh)_2]_\infty$ and 6-coordinate in $[(THF)_2Eu(TePh)_2]_\infty$.These variances in coordination are due solely to differences in chalcogenolate coordination as all other varibales are identical. Finally, the monomeric vs polymeric structures observed in $[(Py)_5Eu(TePh)_2]$. and $[(THF)_2Eu(TePh)_2]_\infty$ undergirds the role of neutral donors in bridging determination. Ultimately, this simple reaction platform spawned a variety of $Ln_x(ER)_y$ derivative species, through careful control of of metal radii, chalcogenolate anions and neutral donors.

One of the key physical advantages to $Ln(ER)_3$ and $Ln(ER)_2$ systems is the absence of IR quenching functional groups near the metal centers. In lanthanide systems with large quantities of C-H, and O-H bonds directly coordinated to the metal centers, quenching of the lanthanides' characteristic IR emissions by the vibrational modes of these groups have been well documented[29,30,31].

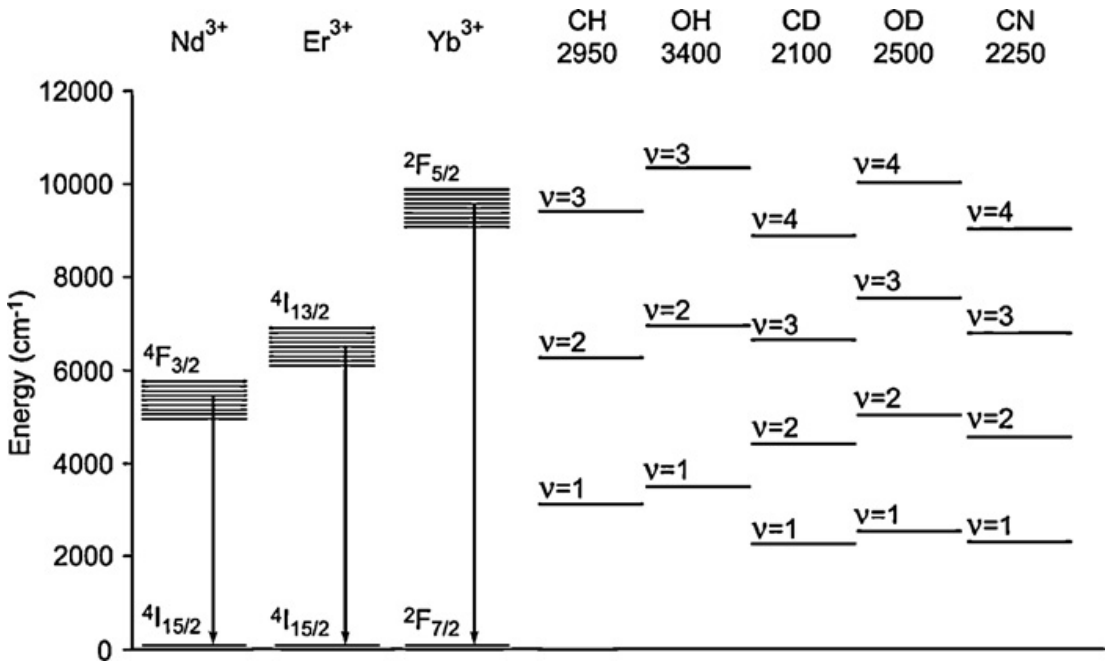

Figure I.6. Energy Gaps For NIR Emitting Ln(III) Species and Vibrational Modes For CH, OH, CD, OD and CN.[32]

Figure. I.6 displays the rationale for this phenomenon by modeling the the radiative energy transition for NIR emitting lanthanides side by side with the common vibrational quenching groups and deuterated analogues[32]. When vibrational quantum states exist at energies that are between the emissive states and the ground states of a Ln(III) species (V=3-1), non-radiative decay becomes

the likely pathway for energy dissipation. This poses a worthwhile problem since Nd^{3+} and Er^{3+} NIR emission are of great interest to telecommunication industry as dopants in fiber optics cables and optical waveguides while the Nd^{3+} and Yb^{3+} have garnered attention as candidates for in vivo luminescent imaging and laser technology.[33] Overall, the $Ln_x(ER)_y$ species provide a viable synthetic platform for the production of molecular lanthanide chalcogenide species with minimized quenching effects and improved quantum efficiencies .

The reduced presence of vibrational quenching groups in tandem to simple augmentations to the $Ln_x(ER)_y$ scheme gave rise to two new classes of emissive rare earth chalcogenide materials with unprecedented quantum efficiencies, expanded solubility and profoundly different architectures. While examining the influence fluoride anions on Ln-E materials Romanelli[34] introduced a fluoride salt into a $Ln_x(ER)_y$ method (Scheme I.3.) and isolated the largest homonuclear lanthanide chalcogenide fluoride to date, $(Py)_{24}Ln_{28}F_{68}(SePh)_{16}$.

$$Ln(SePh)_3 + 2NH_4F \xrightarrow{Py} (Py)_{24}Ln_{28}F_{68}(SePh)_{16} + NH_4SePh$$

Scheme I.2. General Scheme for $(py)_{24}Ln_{28}F_{68}(SePh)_{16}$ Synthesis.

The structure boasts a complicated core-shell architecture with a four member 12 coordinate Ln^{3+} core encapsulated by 12 fluoride anions. The core is then sheathed by 24 Ln^{3+} connected by 56 additional fluoride anions with coordinations between 2 and 4 and capped by sixteen selenolates and terminal pyridines. The 41% QE for the Nd analogue was the second largest ever obtained for a molecular rare earth species.

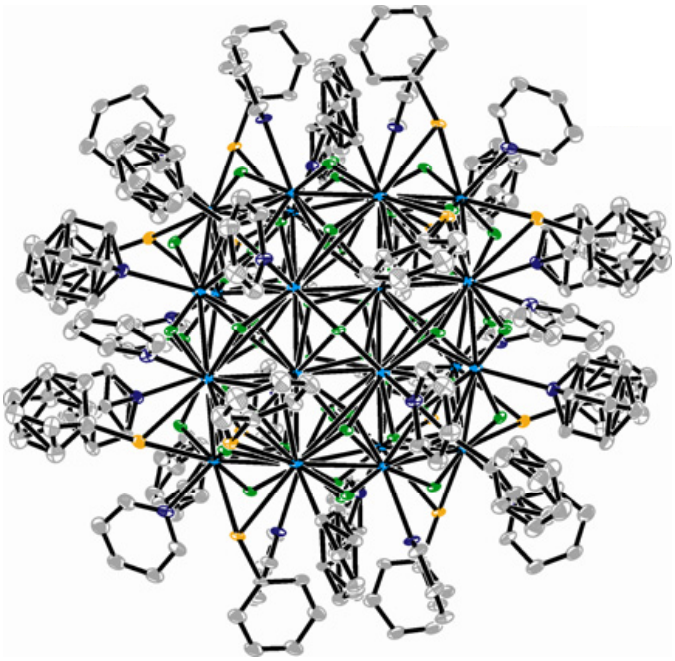

Figure I.7. ORTEP Structure of $(py)_{24}Ln_{28}F_{68}(SePh)_{16}$ (Ln=Ce,Nd, Pr).

As an added bonus, $(py)_{24}Ln_{28}F_{68}(SePh)_{16}$ exhibits a strong solubility in toluene. Similar high nuclearity species have not shown any affinity for toluene, and can be attributed to the polarizing effect of F^-. this latter attribute opened the door for full integration into fluorinated polymers and glass matrixes for the production of hybrid wave amplifiers.[35]

Around the same time Kornienko[36] used the presence of excess Hg and elemental selenium (Scheme I.4) to yield the $[(py)_{11}Ln_7Se_2HgSePh]$ (Figure I.8.).

$$Ln(SePh)_3 + Hg + Se \xrightarrow{Py} (Py)_{11}Ln_7Se_{21}HgSePh \cdot 7Py$$

Scheme I.3. General Scheme for $(py)_{11}Ln_7Se_2HgSePh \cdot 7Py$ Synthesis.

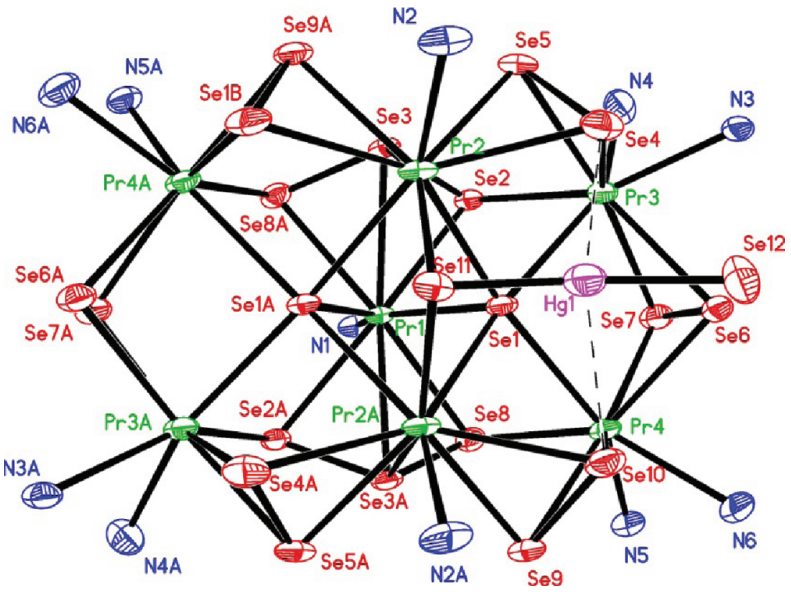

Figure I.8. Pov-Ray Molecular Structure of $(py)_{11}Ln_7Se_2HgSePh \cdot 7Py$.

The $[(py)_{11}Ln_7Se_2HgSePh]$ (Ln= Ce,Pr,Nd) is structurally less cumbersome then the $(py)_{24}Ln_{28}F_{68}(SePh)_{16}$ product and consists of a pair of edge sharing $Ln_4Se(Se_2)_4$ units and is capped by an (Se)Hg(SePh) and a 9-coordinate $(Se_3)pyLn(Se_3)$ units on the convex and concave sides of the structure. Unexpectedly, this system's Nd analogue displays the highest quantum efficiency of any molecular lanthanide chalcogenide known (43%). However, a side by side comparison of the ratios of CH bonds/Nd ions for $(py)_{24}Ln_{28}F_{68}(SePh)_{16}$ and $[(py)_{11}Nd_7Se_2HgSePh]$ reveals a lower value for the latter product. What is truly impressive is all of the physical property gains achieved in both products were accomplished by simple changes to the original reaction platform. This realization provides overwhelming support for $Ln_x(ER)_y$ as a practical route to emissive lanthanide materials with remarkable properties

A similar case can be made for the $Ln_x(ER)_y$ synthetic pathway's use in the production of synthetically challenging magnetic LnE products. Europium monochalcogenide systems' magnetic ordering and semiconducting properties have been an active research topic for some time. In 1963 Mcguire[37] found that the magnetic ordering of EuSe, and EuTe deviated (meta-magnetic and antiferromagnetic respectively) from the ferromagnetic ordering observed in EuO[38] and EuS by Van Vleck in 1961. These findings were in contrast to the accepted rationale of poor metal-ligand orbital overlap, weak magnetic couplings,[39] producing isolated unpaired 4f electrons with paramagnetic interactions. In recent studies, the diverging magnetic ordering of EuE products has been reinvestigated in nano and solid state materials as potential spin filters[40] in spintronic devices. Stoll[41] and Jin[42] have published several papers examining the the size and doping dependence of magnetic ordering in EuS, NaEuS and GdEuS nanoparticles, while Dorhout[43] Albrecht-Schmitt[44] and Meerschaut[45] examined the magnetic anisotropy and dopant dependence in ternary solid state EuE materials. Interestingly, the presence of mixed valent Eu^{2+} and Eu^{3+} was routinely confirmed via Mossbauer spectroscopy. Unfortunately, clear structure/property and valence/property relationships were inaccessible due to the lack of single crystalline products. The inability to determine precise atomic position and bond lengths through single crystal XRD. The difficulty in producing EuE systems lies in the poor solubility of sulfide products in organic solvents as well as the temperature induced phase changes imposed by the high temperature synthesis methods previously employed.

This hurdle has been partially overcome using the $Ln_x(ER)_y$ + E platform (scheme I.2).

$$Ln + 3/2\ PhEEPh \xrightarrow{Solvent/Hg} (L)_xLn(EPh)_3 \xrightarrow{3/4\ E} L_8Ln_8E_6(EPh)_{12}xL$$

Scheme I.4. General Scheme for $Ln_8E_6(EPh)_{12}$ Synthesis.

The solution based crystallization, room temperature conditions, and solubility of $Ln_x(ER)_y$ precursors in organic solvents has led to the isolation of the single crystalline Gd_7EuS_6 Ln_8Se_6 (Ln=Nd,Sm) and $(py)_9Ln_4(Te)(TeTe)_2(TeTeTe(Ph)TeTe)(Te_0TePh)$ (Ln=Sm,Tb,Ho) clusters by Melman[46] and Freedman.[47] Additionally, Norton[48] has recently showcased a pair of monomeric and mixed valence Eu^{2+} and Eu^{3+} trimers stabilized by $(OC_6F_5)^-$. These products serve as testaments to the potential of this method in yielding synthetically difficult magnetic lanthanide chalcogenide systems.

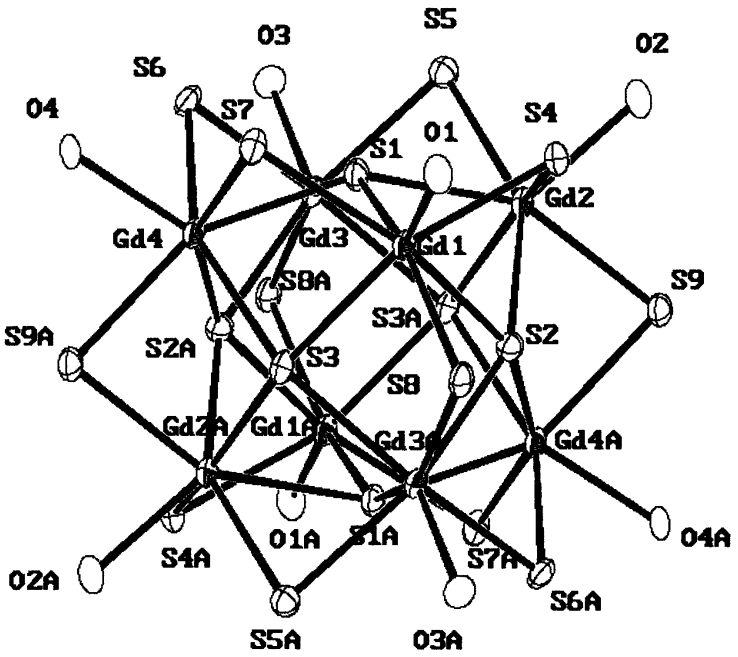

Figure I.9. ORTEP Molecular Structure of $(THF)_8Gd_8(\mu_2\text{-}S)_6(\mu_2\text{-}SPh)_{12}$.

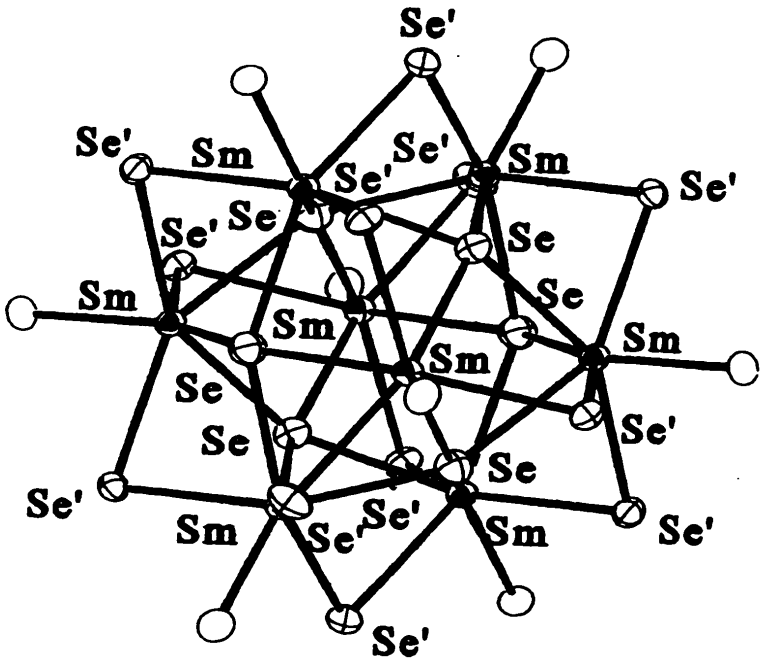

Figure I.10. ORTEP Molecular Structure of $(THF)_8Sm_8(Se)_6(SePh)_{12}$.

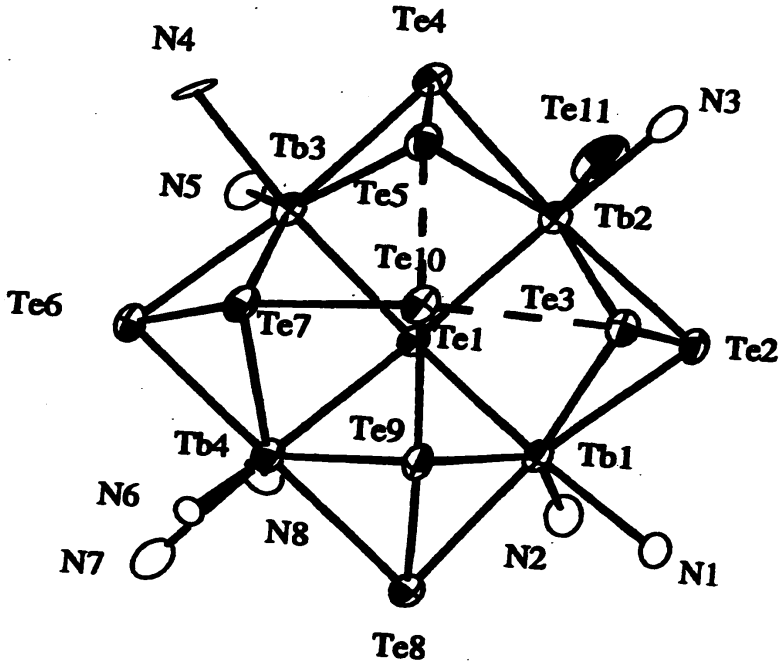

Figure I.11. ORTEP Molecular Structure of $(py)_9Tb_4(Te)(TeTe)_2(TeTeTe(Ph)TeTe)$ Cluster Core.

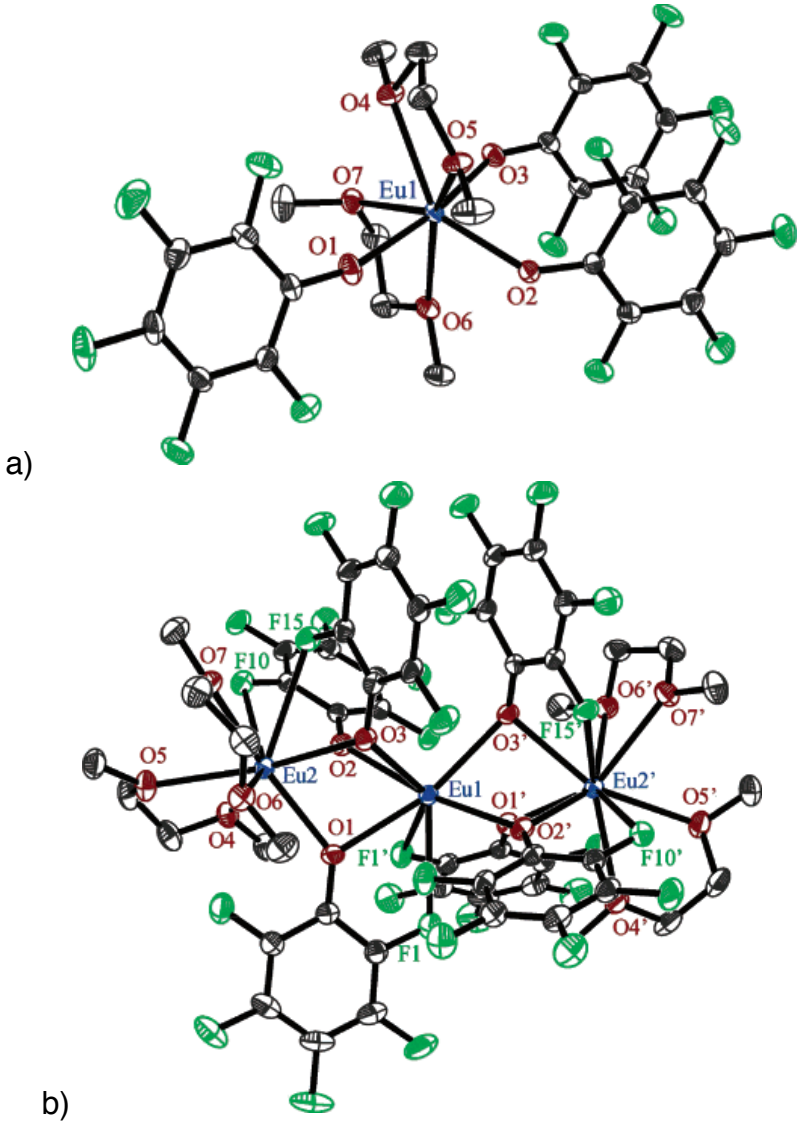

Figure I.12. ORTEP Molecular Structures of a)$(DME)_2Eu(OC_6F_5)_3$ and b) $(DME)_4Eu_3(OC_6F_5)_6$.

With this greater insight two new questions arose. For starters, could pseudohalide anions be used as functional bridges for stabilizing lanthanide chalcogenide clusters? Pseudohalides have been used with transition metals and organic species to form and stabilize a variety of reactive products through surface modification. Very little study has been done with lanthanide based

systems and even less with lanthanide chalcogenides. Since surface modification of complexes is often key to tailoring dopants for host lattices and the core applications of lanthanides rely on such capabilities, the integration of the “borderline” basic pseudohalides (as described in HSAB theory) are an attractive research target for rare earth clusters. Second, in a quest to find the upper limits of lanthanide cluster size and emission practicality, could carefully controlled ionic impurities drive lanthanide chalcogenolate/chalcogenide reactions towards new equilibria? Similar methods have been applied to solid state reactions with great success, why not try the same in solution based lanthanide chalcogenide and chalcogenolate environments?

The coupling of Ln-E chemistry to alkali metal pseudo-halides such as sodium azide offers an interesting if not potentially explosive route to addressing these questions. Azides provide a potential pathway to unique bridging and structure architectures. Metal azide species have also been used as precursors for the thermolytic formation of nitride and oxynitride materials. Such materials have been explored for their potential in the alternative energy and phosphors industries. Next, sodium ions possess a similar coordination chemistry, and a greater reduction potential when compared to their lanthanide counterparts. Their spectroscopically invisible nature in emission studies, and diamagnetic ordering tendency could make them viable anion stabilizers for emissive and magnetic rare earth materials. Finally, the inclusion of sodium to solution based lanthanide chemistry could stabilize previously unseen species with unprecedented physical properties .

The exploration of the interplay between sodium azide and the more established Ln-E chemistry, to direct syntheses and stabilize potentially novel rare earth materials and architectures with interesting physical properties was the focus of the work disclosed herein.

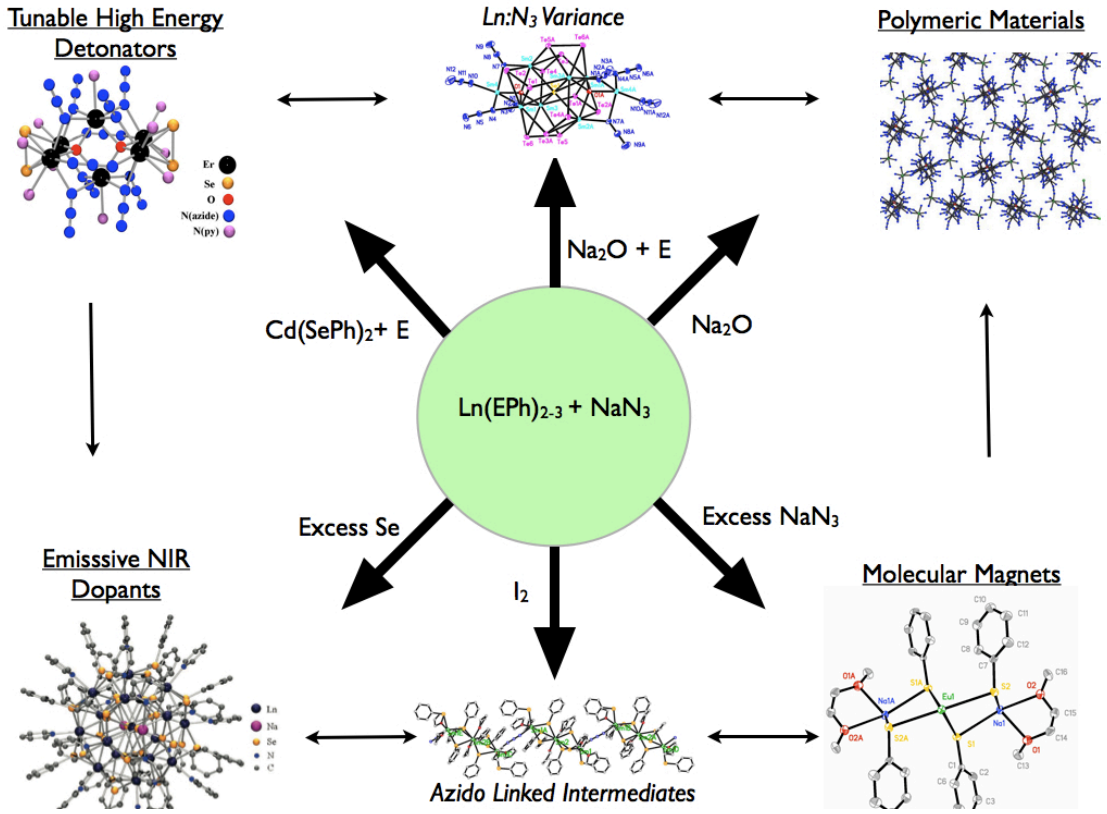

Figure I.13. Lanthanide Chalcogenolate + Sodium Azide Chemistry Summary.

Chapter 1 highlights the synthesis of azide encapsulated hexanuclear and octanuclear oxo and oxo-chalcogenido cluster systems. The synthesis, characterization, X-ray crystallographic analysis, structural analysis and thermolysis studies on these compounds will all be detailed.

Chapter 2 discusses the formation of a novel sodium capped heptadecanuclear lanthanide selenido system. The synthesis, characterization,

structural analysis and emission studies [The Nd cluster analogue displayed near solid state intensities in the (NIR) region,] will be discussed.

Finally, Chapter 3 describes the novel sodium azide mediated synthesis octahedral Eu chalcogenolate (S & Se) complexes. In conjunction with the use of an unpublished Eu^{3+} $(py)_6Eu_2(\mu_4\text{-}S_2)_2(OC_6F_5)$, these species were used as models to probe the roles of valence and structure in the expression of europium monochalcogenide magnetic properties. The synthesis, characterization, magnetic susceptibility measurements, and structural analysis will be presented in detail.

References

[1] Pimentel, G.C. Sprately R.D. *Understanding Chemistry.* Holden-Day Inc., SanFrancisco, **1971**.

[2] American Welding Society. *An American National Standard - Guide for Root Pass Welding of Pipe Without Backing.* **2007**.

[3] Wang, F; Liu, X; *Chemical Society Reviews* **2009**, *38*(4), 353.

[4] Li, H.; Zhu, Y.; Cheng, M.; Ren, Z.; Lang, J. *Coordination Chemistry Reviews* **2006**, *250*, 2059-2092.

[5] Sessoli, R.; Powell, A. K. *Coordination Chemistry Review* **2009**, *253*, 2328.

[6] Knapton, D; Burnworth, M.; Rowan, S.J.; Weder, C *Angew. Chem., Int. Ed* **2006**, *45* ,35, 5825

[7] Pitzer, K.S. *Accounts Chem. Res.*, **1974**, 12, 271.

[8] Lang, P.F. Smith, B.C. *J. Chem. Educ.*, **2010**, *87* 8, 875.

[9] Li, G.; Smith, R.L. Jr. Inomata, H.; *J. Am. Chem.Soc.* **2001**,123,44, 11091.

[10]Cotton, S. *Lanthanides and Actinides.* London: Macmillan Education Ltd, **1991**.

[11] **a)** Schumann, H.; Herrmann, K.; Muehle, S. H.; Dechert, S. *Zeitschrift fuer Anorganische und Allgemeine Chemie* **2003**, 629, 1184. **b)** Wang, S., Li, H., Xie, Z. *Organometallics* **2001**, 20, 3842. **c)** Berube, C.D.; Yazdanbakhsh.; Gambarotta, S.; Yap, G.P.A. *Organometallics* **2003**, 22, 3742. **d)** Bunzli, J.C.G.; Klein, B., Chapuis, G.; Schenk, K.J. *Inorg. Chem* **1982**, 21, 808.

[12] a) Skakle, J. M. S.; *Materials Science & Engineering, R: Reports* **1998**, R23,1, 1. b) Rocha, J.; Carlos, L.D.; *Current Opinion in Solid State & Materials Science* **2003**, 7,3, 199. c)Auzel, F.; Baldacchini, G. *Journal of Luminescence* **2007**, 125,1-2, 25. d) Evans, R.C.; Douglas, P.; Winscom,C.J.; *Coordination Chemistry Reviews* **2006**, 250,15+16, 2093. e) Armelao, L.; Bottaro, G.; Quici,S.; Cavazzini, M.; Scalera, C.; Accorsi, G.; *Dalton Transactions* **2011**, 40,43, 11530.

[13] Binnemans, K. *Chem. Rev*. **2009**, 109, 4283.

[14] chemwiki.ucdavis.edu/Inorganic...Metals.../The_Lanthanides

[15] a)Pearson, R.G.; *Journal of Chemical Education* **1968,** 45, 581. b) Pearson, R. G. *Journal of Chemical Education.* **1968** ,45,643.

[16] Birmingham, J.M.; Wilkinson, G. *J. Am. Chem. Soc.* **1954**, 76, 6210

[17] Evans, W.J.; *Inorg. Chem.* **2007**, 46(9), 3435.

[18] a) Cary, D.; Ball, G.; Arnold, J. *J. Am. Chem.Soc* **1993**, 115, 2520. b) Cary, D.; Arnold, J. *I Inorg. Chem.* **1994**, 33, 1791. c) Janik, J.;Wells, R.; Young Jr., V.; Rheingold, A.; Guzei, I. *J. Am. Chem.Soc.* **1998**, 120, 532.

[19] Tilley, T.; Andersen, R.; Brock, S.; Zalkin, A. *Inorg. Chem.* **1982**, 21, 2647.

[20] Evans, W.J.; Rabe, G.; Ansari, M.; Zilller, J.; *Angew. Chem., Int. Ed.* **1994**, 33, 2110.

[21] Lissner, F.; Schleid, T. *Zeitschrift fuer Anorganische und Allgemeine Chemie.* **2007**, 633,11-12, 1973-1978.

[22] Evans, W.J.; Perotti, J.M.; Kozimor, S.A.; Champagne, T. M.; Davis, B. L.; Nyce, G.W.; Fujimoto, C.H.; Clark, R.D.; Johnston, M. A.; Ziller, J. W.*Organometallics* **2005**, 24,16, 3916.

[23] Berardini, M.; Lee, J.; Freedman, D.; Lee, J.; Emge, T. J.; Brennan, J. G. *Inorg. Chem.* **1997**, 36(25), 5772.

[24] Brewer, M.; Khasnis, D.; Buretea, M.; Berardini, M.; Emge, T. J.; Brennan, J. G. *Inorg. Chem.* **1994**, 33, 2743.

[25] Lee, J.; Freedman, D.; Melman, J.H.; Brewer, M.; Sun, L.; Emge, T. J.; Long, F.H.; Brennan, J.G. *Inorg. Chem.* **1998**, 37, 2512

[26] Lee, J.; Brewer, M.; Emge, T.; Beradini, M.; Brennan, J.G. *Inorg. Chem.* **1995**, 34, 3215.

[27] Beradini, M.; Emge, T.; Brennan, J.G. *J. Am. Chem.Soc.* **1993**, 115, 8501.

[28] Khasnis, D.V.; Brewer, M.; Lee, J.; Emge, T.J.; Brennan, J.G. *J. Am. Chem. Soc.* **1994**, 116, 7132.

[29] Oueslati,I.; Sa Ferreira, R. A.; Carlos, L. D.; Baleizao, C.; Berberan-Santos M.N.; de Castro B..; Vicens, J.; Pischel, U. *Inorg. Chem.* **2006**, 45, 6, 2652.

[30] Artizzu,F.; Mercuri,M.L.; Serpe,A.; Deplano,P. *Coordination Chemistry Reviews* **2011**, 255, 21-22, 2514.

[31] Marks, S.; Heck, J. G.; Habicht, M. H.; Ona-Burgos, P.; Feldmann, C.; Roesky, P. W. *J. Am. Chem.Soc.* **2012**, 134,41, 16983.

[32] Artizzu, F.; Mercuri, M.L.; Serpe, A.; Deplano, P. *Coord. Chem. Rev.* **2011**, 255, 2514.

[33] Zhu, X.; Wong, W-K.; Wonf, W-Y.; Yang, X *Eur. J. Inorg. Chem.* **2011**, 4651.

[34] Romanelli, M.; Kumar, G. A.; Riman, R.E.; Emge, T. J.; Brennan, J. G. *Angew. Chemie.* **2008**, 47, 6049.

[35] Becker,P.C.; Olsson,N.A.; Simpson,J.R. *Erbium Doped Fiber Amplifiers Fundamentals and Technology*; Academic Press: San Diego, CA, **1999**.

[36] Kornienko, A.; Moore, B. F.; Kumar, G. A.; Tan, M-C.; Riman, R.E.; Brik, M. G.; Emge, T. J.; Brennan, J. G. *Inorg. Chem.* **2011**, 50,18, 9184.

[37] Mcguire, T.R.; Argyle, B.E.; Shafer, M.W.; Smart, J.S. *J. Appl. Phys.* **1963**, 34, 1345.

[38] Matthias, B.T.; Bozorth, R.M.; Van Vleck, J.H. *Phys. Rev. Letters.***1961**, 7, 160.

[39] Vogt, O.; Mattenberger, K. *J. Alloy. Compd.* **1995**, 223,226.

[40] (a) Hao, X.; Moodera, J. S.; Meservey, R. *Phys. ReV. B* **1990**, 42,13, 8235. (b) Muller, C.; Lippitz, H.; Paggel, J. J.; Fumagalli, P. *J. Appl.Phys.* **2004**, 95,11, Pt. 2, 7172.

[41] Kar, S. ; Boncher, W. L.; Olszewski, D.; Dollahon, N.; Ash, R.; Stoll, S. L. *J. Am. Chem. Soc.* **2010**, 132, 13960.

[42] Selinsky, R. S.; Han, J. H.; Perez, E. A. M.; Guzel, I. A.; Jin, S. *J. Am. Chem. Soc.* **2010**, 132, 15997.

[43] Choudhury,A.; Grandjean,F.; Long, G.J.; Dorhout, P.K. *Inorg. Chem.* **2012**, 51, 11779.

[44] Jin, G.B.; Choi,E.S.;Guertin, R.P.; Albrecht-Schmitt, T.E. *J. Solid. State. Chem.* **2007**, 181, 14.

[45] Cario,L.; Palvadeau, P.; Lafond, A.; Deudon, C.; Moelo, Y.; Corraze, B.; Meerschaut, A. *Chem. Mater.* **2003**,15, 943.

[46] Melman, J.H. Molecules, clusters, and solid-state materials with lanthanide-sulfur bonds :synthesis, structure, and reactivity. Ph.D. Dissertation, Rutgers the State University of New Jersey, New Brunswick, NJ, **2004**.

[47] Freedman, D.; Emge, T.J.; Brennan, J. *Inorg. Chem.* **1999**, 38, 4400.

[48] Norton, K.; Emge, T.J.; Brennan, J.G. *Inorg. Chem.* **2007**,46, 4060.

Chapter 1. Azide Encapsulated Lanthanide Clusters

1.1 Introduction

Inorganic azide chemistry stands as an intimidating and potentially hazardous gateway to novel functional materials. The azide anion (N_3^-) consists of a linear three nitrogen atom structure described by a resonance form (Figure 1.1). N_3^- readily releases nitrogen gas upon heating,[1] forms the explosive hydrazoic acid upon acidification,[3,8] and detonates due to simple "jarring" of its heavy metal products, (e.g. lead azide).[3,8]

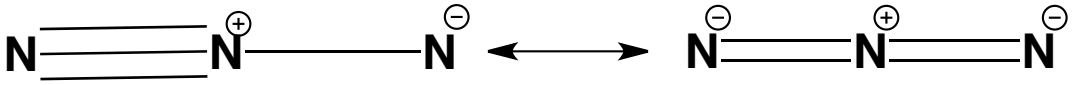

Figure 1.1 : Azide Anion Resonance Forms

Simultaneously, inorganic azide systems have garnered significant research interest as reactive precursors to mutifunctional metal nitrides ,[2] surface modifiers for nanomaterials,[3] and photochemical deactivators in incendiary systems.[4]

The rationale for the production of metal azide systems is rooted in three unique attributes of the azide anion. First, the azide ligand introduces a diverse array of bonding modes and, provides a versatile set of linkers and end caps for constructing unique polymer and cluster architectures (Figure 1.2) . the mono and polydentate ligand behavior observed is due to the fluctuating bond polarity explained by the resonance stabilized structure.

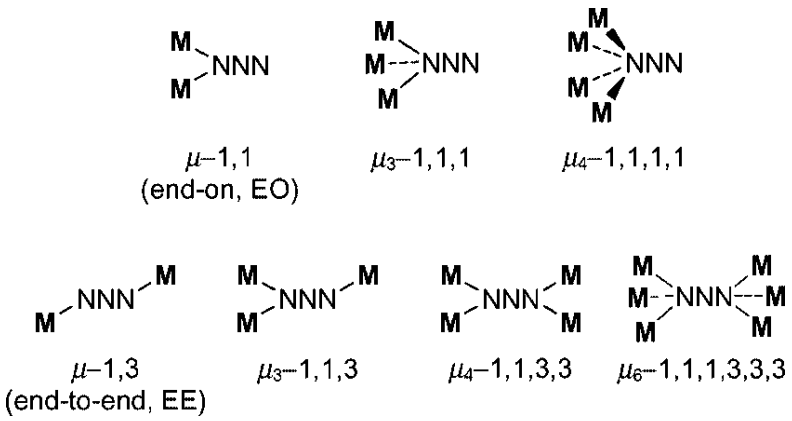

Figure 1.2. Azide Bonding Moieties for Transition Metals[5]

Maunter[6] as well as Christou[7] have provided unique examples of manganese azido polymers and clusters utilizing a variety of azide bridging modes. Second, the azide linkage between metal centers, (EE, and EO), displays the ability to preferentially mediate antiferromagnetic,[8]EE and ferromagnetic[9] EO interactions as super-exchange pathways. The presence of available π orbitals on the azide creates the possibility of orbital overlap with metal D or F type orbitals containing unpaired electrons. When coupled with the inherent interest in the magnetic properties of Fe, Ni, Mn & Cu, clusters, a plethora of new large nuclearity magnetic azide complexes[10,11] and a resurgence of single molecular magnets (SMM) research has resulted. Finally, the instability of the azide anion has been employed in the reduction and thermolytic synthesis of terminal and bridging nitrides.[12] The heats of formation of inorganic azide species[13] NaN_3 (80 cal/g) and PbN_3 (397 cal/g) when compared to N_2 (0 cal/g) clearly indicate a thermodynamic drive towards azide elimination in favor of N_2. Since azide reduction produces gaseous N_2 and MoN^{3-} species, nitride materials became a

sought after byproduct. An example is the use of uranium azide, $[U(N_3)_n]$ products as precursors for the formation of uranium nitride. Evans,[14] reported a novel octanuclear uranium complex comprising alternating nitride and azide bridges, while King[15] and Kiplinger,[16] both demonstrated the ability to reduce sterically crowded uranium azides to terminal nitrides and amines respectively. These three properties combine to make inorganic azide chemistry a widely varied and potentially viable route towards products with unique physical properties.

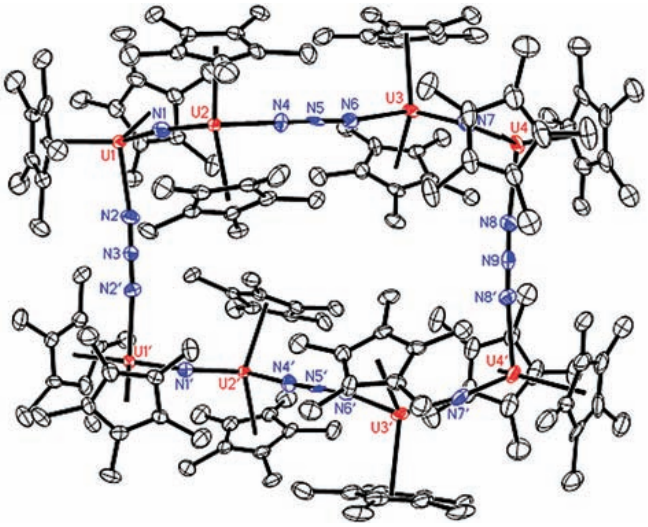

Figure 1.3. Evans et al. Alternating Uranium Azide Nitride Species.[48]

The diverse applications of metal nitrides provided the need for low cost azide precursors to produce them. Uranium nitride is continually sought after as a more efficient fuel source in next generation nuclear reactors. The higher fissionable material density of uranium nitride when compared to the currently used uranium oxide ($U0_2$) is a key reason for the intense interest in the former. However, direct methods of production have been hampered by impurities in the materials[17] and high production costs. Similarly, transition metal nitrides and

oxynitrides have become the source of great interest as semiconductors, tool coatings[18] and phosphors.[19]

Despite the utility of the previously mentioned materials, and the potential of lanthanide azide and oxyazide complexes to produce lanthanide nitride materials and unique azide stabilized structures little to no attention has been paid to the area. This oversight was the motivation for this work.

1.2 Oxy-Azide Clusters: Synthesis, Structure, and Discussion

Initially, $Sm(SePh)_2$ was reacted with undried sodium azide (NaN_3) in pyridine in an effort to investigate the azides ability to stabilize lanthanide complexes. Single crystals of $(py)_{10}Sm_6O_2(N_3)_{16}Na_2(py)_8 7(py)$ (Figure 1.3) were isolated. The initial product could only be episodically reproduced using these conditions (scheme 1.1a). The system was reliably reproduced by using an alternate oxo source. $Sm(SePh_2$, dried sodium azide (NaN_3) and sodium oxide (Na_2O) were combined to give the targeted material, (Figure 1.5) in low yield (8.3%).

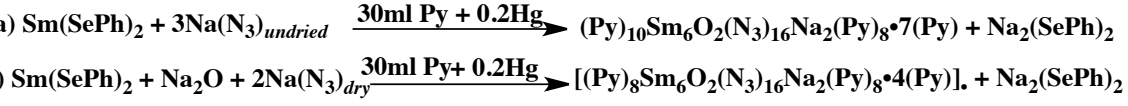

Scheme 1.1.General Schemes for the Synthesis of a)$(Py)_{10}Sm_6O_2(N_3)_{16}Na_2(py)_8$ 7(py) and b) $(py)_8Sm_6O_2(N_3)_{16}Na_2(py)_8$ 4(py).

The two methods produce clusters with isostructural cores consisting of 2 central μ_4 oxo ligands surrounded by six Sm^{3+} ions in a distorted tetrahedral

geometry (Figure 1.4). The Sm_6O_2 units are encapsulated by azides in three different modes, μ_2 EO, μ_3 EO, and μ_2 EE. The products diverge in the geometries about the Na capping groups. Scheme 1.1a produces a terminal cluster with a pair of $Na(py)_4$ each with one μ_3-azide bridging to two Sm^{3+} and a μ_2 N_3^- bridging to a single samarium metal center (Figure 1.4).

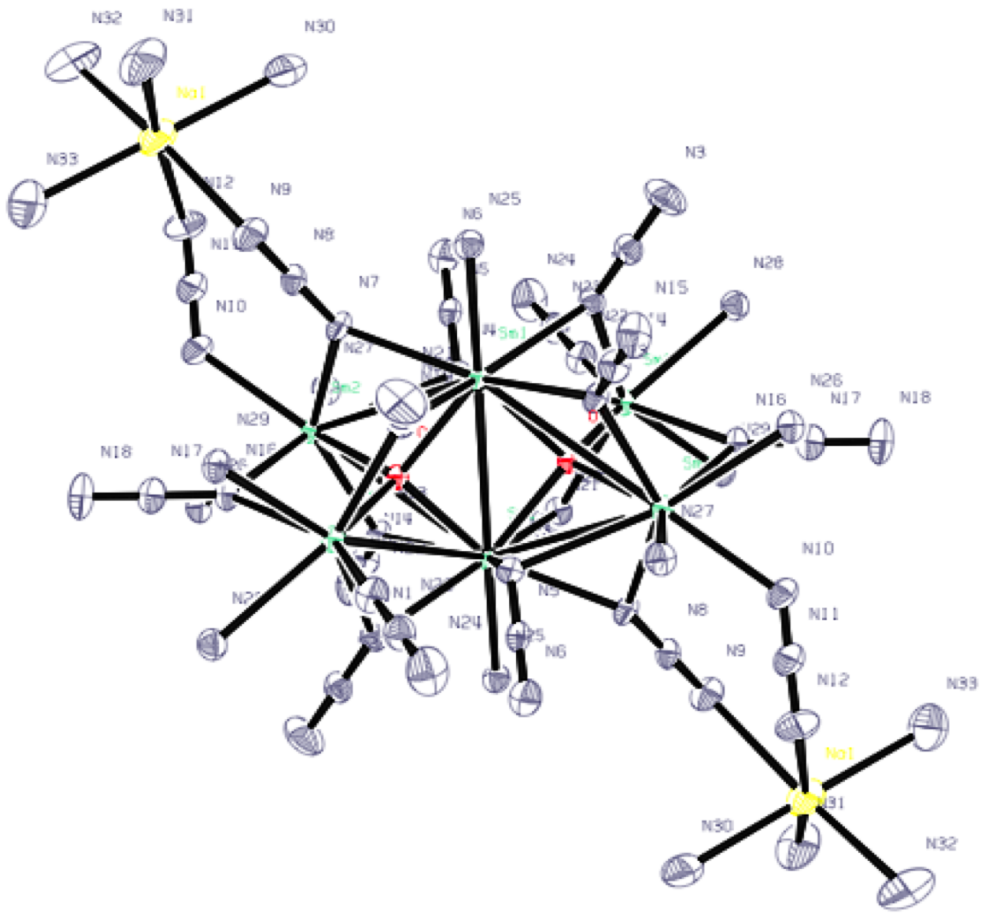

Figure 1.4. ORTEP Molecular Structure of $(py)_{10}Sm_6O_2(N_3)_{16}Na_2(py)_8 \cdot 7(py)$, **(1a)**.

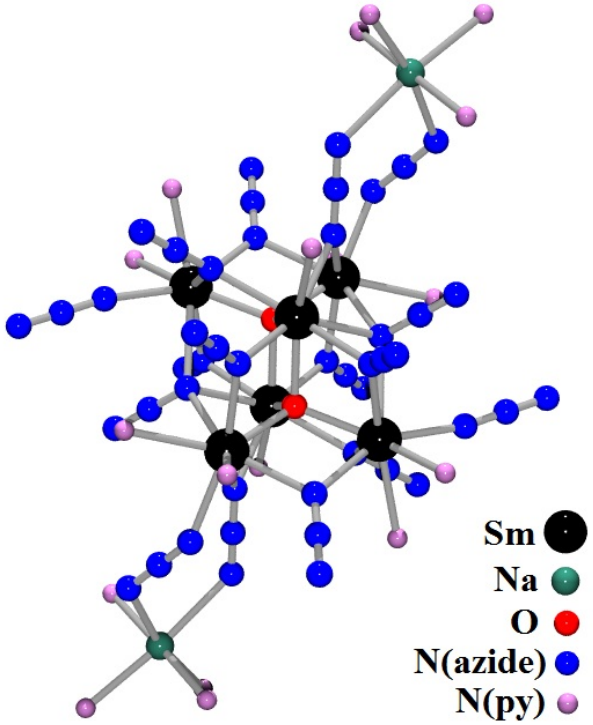

Figure 1.5 Pov-Ray Molecular Structure of $(py)_8Sm_6O_2(N_3)_{16}Na_2(py)_8 \cdot 4(py)$, **(1b)**.

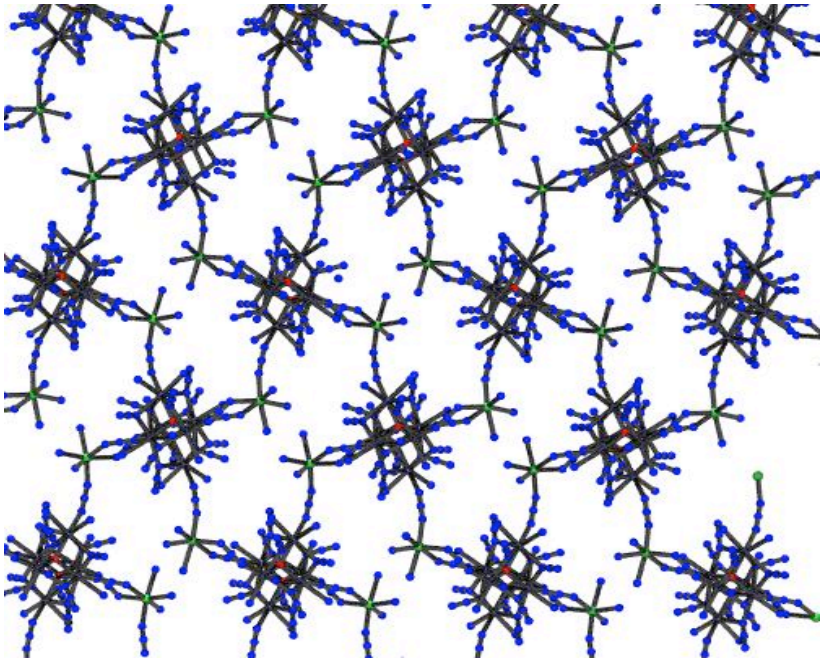

Figure 1.6. Polymer Structure of $(py)_8Sm_6O_2(N_3)_{16}Na_2(py)_8 \cdot 4(py)$.

Empirical formula	C_{125} H_{125} N_{73} Na_2 O_2 Sm_6 molecular	C_{100} H_{100} N_{68} Na_2 O_2 Sm_6 polymer
Formula weight	3630.06	3234.56
Temperature (K)	100(2)	100(2)
Wavelength (Å)	0.71073	0.71073
Crystal system	Monoclinic	Monoclinic
Space group	C2/c	P2(1)/c
a (Å)	25.523(3)	15.8237(8)
b (Å)	18.9410(18)	17.1525(9)
c (Å)	33.039(3)	23.3421(12)
α (deg)	90°	90°
β (deg)	112.106(2)	97.599(1)
γ (deg)	90	90
Z	4	2
Volume ($Å^3$)	14798(2)	6279.8(6)
Density (calculated) (g/cm^{-3})	1.629	1.711
Final R indices	R1 = 0.0529, wR2 = 0.1160	R1 = 0.0272, wR2 = 0.0625

Table 1.1. Crystal Data and Structure Refinement for $(py)_{10}Sm_6O_2(N_3)_{16}Na_2(py)_8 \cdot 7(Py)$ (Molecular) and b) $(py)_8Sm_6O_2(N_3)_{16}Na_2(py)_8 \cdot 4(py)$ (Polymer) .

.

Bond	Bond Distances (Å) Molecule	Bond Distances (Å) Polymer
Sm(1)-O(1)	2.305(3)	2.3093(16)
Sm(1)-O(1)#1	2.316(3)	2.3226(17)
Sm(1)-N(19)#1	2.478(4)	2.467(2)
Sm(1)-N(13)#1	2.490(4)	2.503(2)
Sm(1)-N(7)	2.510(4)	2.505(2)
Sm(1)-N(1)	2.580(4)	2.561(2)
Sm(1)-N(4)	2.603(4)	2.635(2)
Sm(2)-O(1)#1	2.288(3)	2.418(2)
Sm(2)-N(13)	2.478(4)	2.556(2)
Sm(2)-N(7)	2.553(5)	2.687(2)
Sm(2)-N(27)	2.649(5)	2.2792(17)
Sm(2)-N(4)	2.672(4)	2.423(2)
Sm(2)-N(26)	2.684(4)	2.471(2)
Sm(3)-O(1)	2.301(3)	2.491(2)
Sm(3)-N(22)	2.371(5)	2.557(2)
Sm(3)-N(19)	2.483(4)	2.842(2)
Sm(3)-N(16)#1	2.496(4)	2.3093(16)
Sm(3)-N(1)	2.530(4)	2.483(3)
Na(1)-N(12)	2.501(6)	2.488(3)
Na(1)-N(9)	2.601(6)	2.584(3)
Sm(3)-N(4)	2.847(4)	2.842(2)

Table 1.2. List of Significant Bond Distances for $(py)_{10}Sm_6O_2(N_3)_{16}Na_2((py)_8 \cdot 7$ (py) and $(py)_8Sm_6O_2(N_3)_{16}Na_2((py)_8 \cdot 4(py)$.

1b's core is capped by a pair of $Na(py)_3$ units with two μ_2 azides bridging to a single samarium, and a μ_2-azide bridging to a samarium of another cluster. This results in the formation of a two dimensional polymeric structure (Fig 1.6).

Bond Types	Single Molecule (Å)	Polymer (Å)
Sm-O	2.28-2.32	2.28-2.32
Sm-N_3 (μ_3)	2.50-2.87	2.64-2.84
Sm-N_3 (μ_2)	2.47-2.49	2.47-2.55
Na-N_3 (μ_3)	2.60	2.48
Na-N_3 (μ_2)	2.50	2.53
Na-N_3 polymer bridging	------	2.49
Sm-N_3 polymer bridging	------	2.42
Sm-N_3 (terminal)	2.37	------

Table 1.3. Bond Length Comparison for $(py)_{10}Sm_6O_2(N_3)_{16}Na_2\ (py)_8 \cdot 7(py)$ and $(py)_8Sm_6O_2(N_3)_{16}Na_2\ (py)_8 \cdot 4(py)$.

The bond lengths for both phases are nearly identical with the exception of the Na-N_3 (μ_3) bond which differ by approximately 0.1Å. The remaining differences pertain to the bonds associated with bridging in the polymeric species. A comparison of torsion angles (Table 1.7) also displays nearly identical coordination characteristics.

Bond Angle	Single Molecule (º)	Polymer (º)
Sm-O-Sm	105-115	104-115
Sm-N_3 (μ_3)-Sm	88-144	87-145
Sm-N_3 (μ_2)-Sm	103	102
Sm-N_3 (μ_3)Na-Sm	93	95
N_3 (μ_3)-Na-N_3 (μ_2)	80	78
Na-N_3 (μ_2)-Sm polymer	------	162

Table 1.4. Torsional Angle Comparison of $(py)_{10}Sm_6O_2(N_3)_{16}Na_2$ $(py)_8 \cdot 7(py)$ and $(py)_8Sm_6O_2(N_3)_{16}Na_2$ $(py)_8 \cdot 4(py)$.

1.3 Oxy-Chalcogen Azide Clusters: Synthesis, Structure, and Discussion

In an effort, to further explore lanthanide azide chemistry varying amounts of elemental chalcogenide and chalcogenolate sources were introduced into the previous reaction conditions. This resulted in the discovery of several unique azide clusters with chalcogen and chalcogenolate motifs incorporated into their structures. The first method (Scheme 1.2) substituted divalent samarium with the radially smaller trivalent erbium and holmium.

$$\mathbf{2Ln(SePh)_3 + Na_2O + 2Na(N_3) \xrightarrow[Ln= Ho, Er]{Py + .08Hg} (Py)_8Ln_6O_2(N_3)_{12}(SePh)_2 + Na_2(SePh)_2}$$

Scheme 1.2.General Synthesis of $(py)_8Ln_6O_2(N_3)_{12}(SePh)_2$, (**2**).

The resulting products shown in Figure 1.7 are a hexanuclear cluster with an Ln_6O_2 core, consisting of two μ_4-oxos, with two 7 coordinate metal centers and 4

8-coordinate metal centers. The core is encapsulated by 2 μ_2 EE azide ligands, and 10 μ_2 EO azides. Two μ_2 -SePh ligands with their phenyl rings oriented inward towards the cluster, cap the ends. Their orientation when combined with the 8 pyridines of solvation contributes to a seemingly stable packing mode.

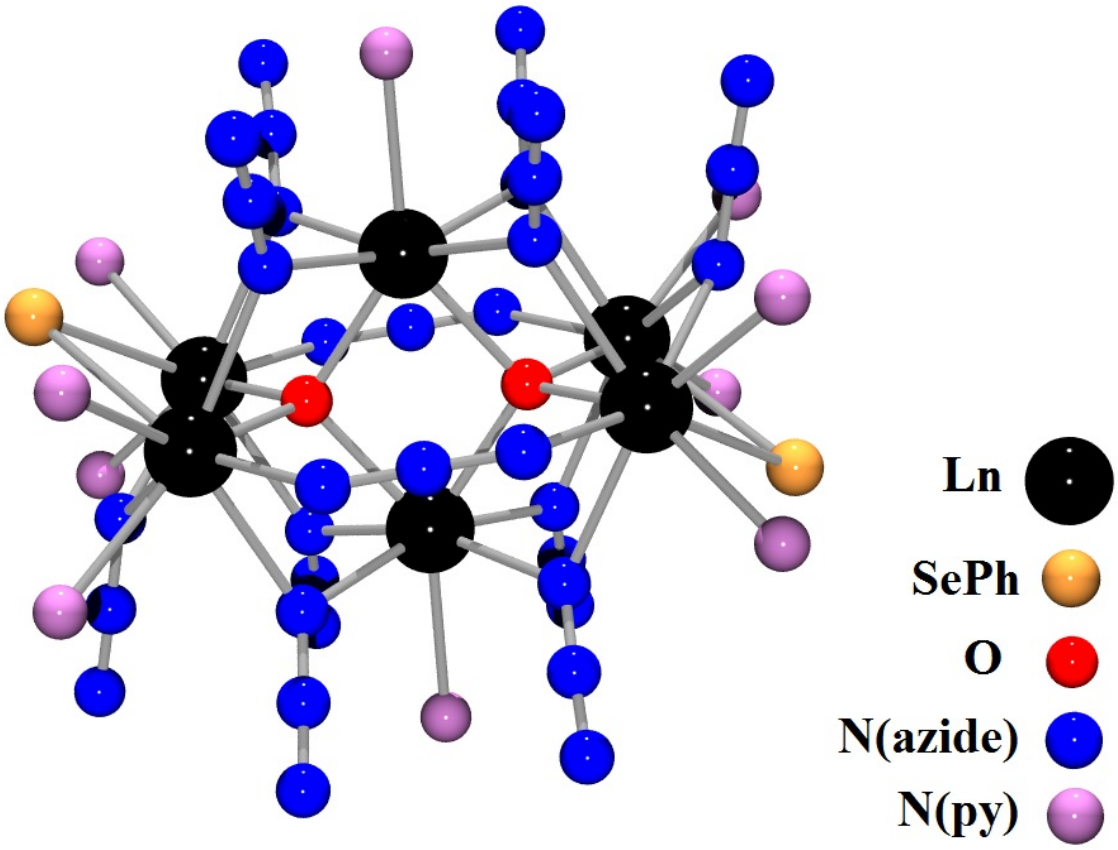

Figure 1.7. POV-Ray Molecular Structure of $(py)_8Ln_6O_2(N_3)_{12}(SePh)_2$, (Carbon and Hydrogen Removed).

The isostructural holmium analogue $(py)_8Ho_6O_2(N_3)_{12}(SePh)_2$ displayed bond distance ranges of 2.46-2.47 Å for the 2 Ho-N(EE-azido), 2.39-2.48 Å, for the 10 Ho-N(EO-azido); 2.51-2.64 Å and 2.24-2.28 Å for the 4 Ho-O bonds.

These were larger than the related bond lengths in the selenolate capped erbium system (difference of ~.03 Å) and were consistent with the larger ionic radii of holmium versus erbium.

Investigation of the interaction between $Cd(SePh)_2$, selenium and erbium, was initially undertaken to establish if N_3^- anion would have a dramatic impact on heterometallic chemistry. The experiment resulted in the formation and isolation of a diselenido capped analogue of the previous system as, $(py)_{10}Er_6O_2(Se_2)(N_3)_{10}$ (**3**) using the scheme shown (Scheme 1.3).

$$2Cd + 4(SePh)_2 + Er + 2Se + Na_2O + 2Na(N_3) \xrightarrow{Py + .02Hg} (Py)_{10}Er_6O_2(Se_2)_2(N_3)_{10}$$

Scheme 1.3. Synthesis of $(py)_{10}Er_6O_2(Se_2)(N_3)_{10}$

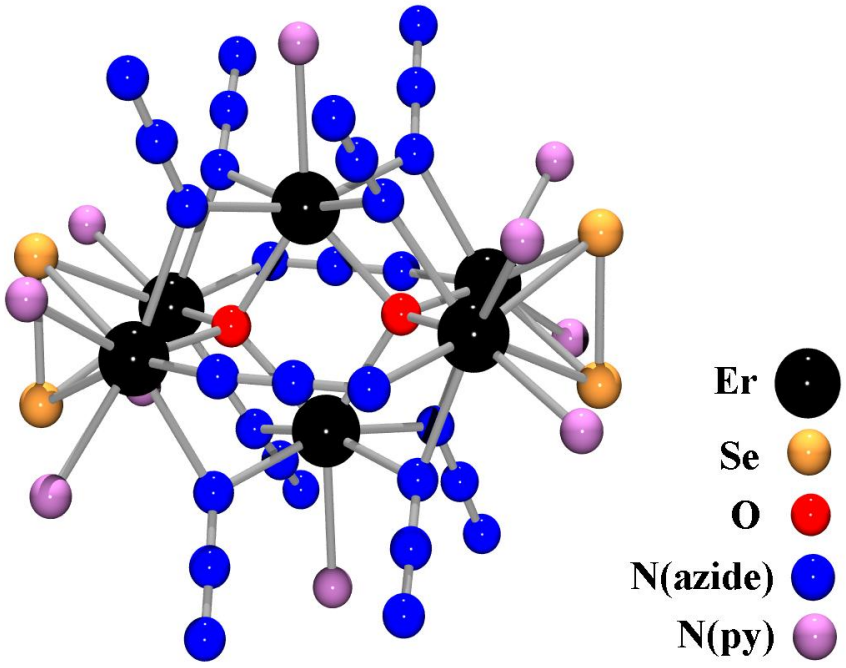

Figure 1.8. POV-Ray Crystal Structure of $(py)_{10}Er_6O_2(Se_2)_2(N_3)_{10}$, (Product 3).

Empirical formula	C_{102} H_{100} Er_6 N_{54} O_2 Se_2	C_{65} H_{65} Er_6 $N_{39.07}$ O_2 $Se_{5.31}$
Formula weight	3275.84	2848.38
Temperature (K)	100(2)	100(2)
Wavelength (Å)	0.71073	0.71073
Crystal system	Triclinic	Triclinic
Space group	P-1	P-1
a (Å)	14.3072(12)	13.2354(8)
b (Å)	15.5856(13)	13.5062(8)
c (Å)	16.380(2)	15.3672(9)
α (deg)	115.349(2)	113.675(1)
β (deg)	103.765(2)	93.405(1)
γ (deg)	104.963(2)	115.494(1)
Z	1	1
Volume ($Å^3$)	2923.9(5)	2179.4(2)
Density (calculated) (g/cm^{-3})	1.860	2.170
Final R indices	R1 = 0.0296, wR2 = 0.0628	R1 = 0.0269, wR2 = 0.0598

Table 1.5. Crystal data and Structure Refinement for $(py)_8Er_6O_2(N_3)_{12}(SePh)_2$, (**2**) and $(py)_{10}Er_6O_2(Se_2)_2(N_3)_{10}$ (**3**).

Bond	Bond Distance
Er(1)-O(1)	2.248(2)
Er(1)-N(13)#1	2.440(3)
Er(1)-N(4)	2.443(3)
Er(1)-N(12)#1	2.446(3)
Er(1)-N(1)	2.449(3)
Er(1)-Se(1)	2.9589(4)
Er(2)-O(1)	2.241(2)
Er(2)-N(16)#1	2.412(3)
Er(2)-N(1)	2.445(3)
Er(2)-N(7)	2.458(3)
Er(2)-N(10)	2.463(3)
Er(2)-Se(1)	2.9471(4)
Er(3)-O(1)#1	2.235(2)
Er(3)-O(1)	2.254(2)
Er(3)-N(4)	2.382(3)
Er(3)-N(7)	2.383(3)
Er(3)-N(16)	2.386(3)
Er(3)-N(13)	2.392(3)
O(1)-Er(3)#1	2.235(2)
N(12)-Er(1)#1	2.446(3)
N(13)-Er(1)#1	2.440(3)
N(16)-Er(2)#1	2.412(3)

Table 1.6 List of Significant Bond Distances for $(py)_8Er_6O_2(N_3)_{12}(SePh)_{2,}$ (**2**).

Bonds	Bond Distances (Å)
Er(1)-O(1)	2.263(2)
Er(1)-N(20)	2.415(3)
Er(1)-N(11)	2.433(4)
Er(1)-N(14)	2.472(4)
Er(1)-Se(1)	2.8937(4)
Er(1)-Se(2)	2.9260(4)
Er(2)-O(1)#1	2.240(2)
Er(2)-O(1)	2.245(2)
Er(2)-N(20)	2.357(3)
Er(2)-N(8)	2.370(3)
Er(2)-N(17)	2.377(3)
Er(2)-N(11)#1	2.396(4)
Er(3)-O(1)	2.240(2)
Er(3)-N(8)	2.420(3)
Er(3)-N(16)#1	2.422(4)
Er(3)-N(17)#1	2.454(3)
Er(3)-Se(2)	2.8767(4)
Er(3)-Se(1)	2.9239(4)
O(1)-Er(2)#1	2.240(2)
N(11)-Er(2)#1	2.396(4)
N(16)-Er(3)#1	2.422(4)
N(17)-Er(3)#1	2.454(3)

Table 1.7. List of Significant Bond Distances for $(py)_{10}Er_6O_2(Se_2)_2(N_3)_{10}$.

A comparison of the bond lengths in **2** & **3** (Table 1.11) shows that the cores are isomorphous. In $(py)_{10}Er_6O_2(Se_2)_2(N_3)_{10}$ there is evidence of site disorder at the diselenide ligand position for a pair of EO azides, and a single EO azide at a third site. This occurs in 3% (sites 1&2) and 20% (site 3) and accounts for the range of Er-Se bond lengths observed (2.85 -3.14 Å).

Bond types	**$(py)_8Er_6O_2(N_3)_{12}(SePh)_2$ Bond Lengths (Å)**	**$(py)_{10}Er_6O_2(Se_2)_2(N_3)_{10}$ Bond Lengths (Å)**
Er-SePh	2.95-2.96	------
Er-N_3 (EE)	2.44-2.46	2.42-2.47
Er-N_3 (EO)	2.39-2.44	2.38-2.45
Er-O (7 coordinate)	2.24-2.25	2.23-2.26
Er-O (8 coordinate)	2.24-2.25	2.24
Er-Se_2	------	2.89-2.93

Table 1.8. Comparison of Select Bond Lengths for $(py)_8Er_6O_2(N_3)_{12}(SePh)_2$ and $(py)_{10}Er_6O_2(Se_2)_2(N_3)_{10}$.

The Ln_6O_2 cores of **2** and **3** also appear to be very similar to the core of **1a**. Their Ln-N_3 and Ln-O bonds are within the same ranges, (2.42-2.48 Å), and (2.23-2.30 Å) respectively. However, there are a few differences. The absence of sodium in the erbium structures, and their subsequent replacement by SePh and Se_2 serves as an example of the possibility to direct Ln/azide cluster formation without the inclusion of sodium. These analogous structures owe their formation, to the removal of sodium ions via NaSePh isolation. This serves the dual role of eliminating starting anions from the targeted rare earth centers, and provides a

facile way for introducing the azide ligand while eliminating its counterparts. Another divergence between the two structure families is the presence of the two Ln-Ln μ_2 EE azide ligands, in the erbium structures. The absence of this motif in the samarium system (μ_2 EE motifs are between Na and Ln cations), opens up the potential to control azide bonding patterns in lanthanide clusters without the use of bulky ligands via careful ion radii selection, azide to metal ratio control, and chalcogenide vs chalcogenolate selection.

Finally, in an attempt see if the weakly binding tellurium ion (Te^{2-}) would competitively bind in the presence of azide anions, a novel lanthanide tellurido azide cluster was produced by the introduction of tellurium (Scheme 1.4).

$$3Sm(SePh)_2 + 4Te + Na_2O + 2Na(N_3) \xrightarrow{Py + .02Hg} (Py)_{16}Sm_8Se(O)_2Na_2(Te_2)_6(N_3)_8$$

Scheme 1.4. Synthesis of $(py)_{16}Sm_8Se(O_2)Na_2(Te_2)_6(N_3)_8$.

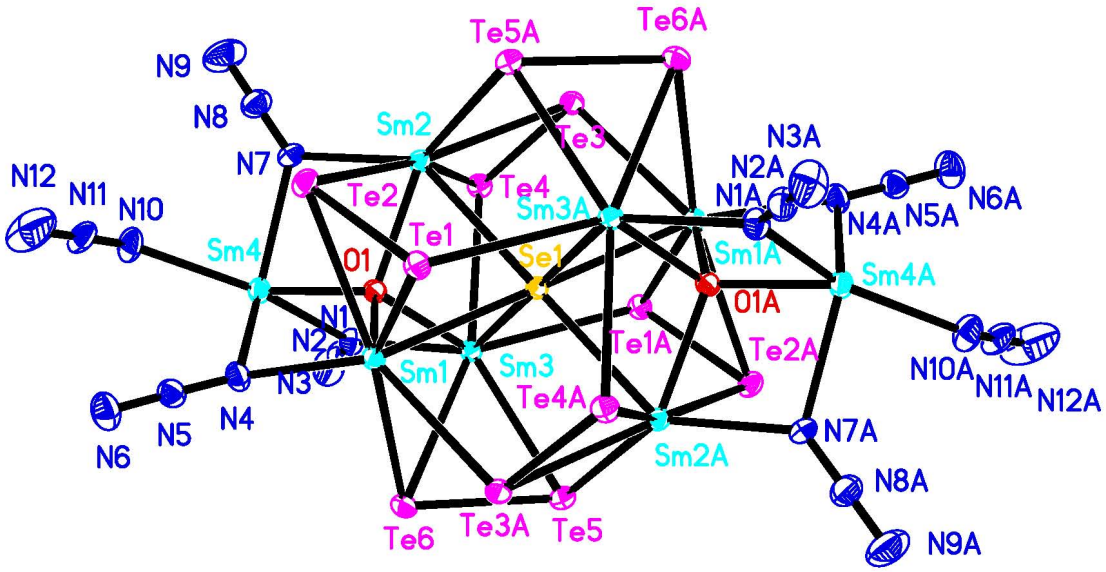

Figure 1.9. ORTEP of $(py)_{16}Sm_8Se(O_2)Na_2(Te_2)_6(N_3)_8$ Core, Drawn at 50%. (**4**)

Empirical formula	$C_{120.27}$ H_{120} $N_{46.94}$ Na_2 O_2 $Se_{1.27}$ Sm_8 Te_{12}
Formula weight	5135.29
Temperature (K)	100(2)
Wavelength (Å)	0.71073
Crystal system	Triclinic
Space group	P-1
a (Å)	15.7784(8)
b (Å)	16.5562(9)
c (Å)	17.3804(9)
α (deg)	94.035(1)
β (deg)	113.759(1)
γ (deg)	108.125(1)
Z	1
Volume ($Å^3$)	3848.0(3)
Density (calculated) (g/cm^{-3})	2.216
Final R indices	R1 = 0.0291, wR2 = 0.0713

Table 1.9. Crystal Data and Structure Refinement for

$(py)_{16}Sm_8Se(O_2)Na_2(Te_2)_6(N_3)_8$, (**4**).

Bond	Bond Distance (Å)	Bond	Bond Distance (Å)
Sm(1)-O(1)	2.351(2)	Sm(4)-N(1)	2.468(3)
Sm(1)-N(4)	2.526(3)	Sm(4)-N(4)	2.472(3)
Sm(1)-Se(1)	3.0318(2)	Sm(4)-Se(2)	3.085(6)
Sm(1)-Te(1)	3.1101(3)	Na(1)-N(12)	2.435(6)
Sm(1)-Te(2)	3.1716(3)	Na(1)-N(6)	2.503(5)
Sm(1)-Te(3)#1	3.2066(3)	Te(1)-Sm(3)#1	3.2161(3)
Sm(1)-Te(6)	3.2597(3)	Te(3)-Sm(1)#1	3.2066(3)
Sm(2)-O(1)	2.376(2)	Te(5)-Sm(2)#1	3.2783(3)
Sm(2)-N(7)	2.469(3)	Se(1)-Sm(1)#1	3.0319(2)
Sm(2)-Se(1)	3.0393(2)	Se(1)-Sm(2)#1	3.0393(2)
Sm(2)-Te(3)	3.1183(3)	Se(1)-Sm(3)#1	3.0470(2
Sm(2)-Te(4)	3.2426(3)	Sm(3)-Te(5)	3.1300(3)
Sm(2)-Te(2)	3.2535(3)	Sm(3)-Te(6)	3.2118(3)
Sm(2)-Te(5)#1	3.2783(3)	Sm(3)-Te(1)#1	3.2160(3)
Sm(3)-O(1)	2.364(2)	Sm(3)-Te(4)	3.2317(3)
Sm(3)-N(1)	2.514(3)	Sm(4)-O(1)	2.242(2)
Sm(3)-Se(1)	3.0469(2)	Sm(4)-N(10)	2.401(4)
Sm(4)-N(7)	2.428(3)	------	------

Table 1.10. List of Significant Bond Distances for $(py)_{16}Sm_8Se(O_2)Na_2(Te_2)_6(N_3)_8$, (**4**).

This octanuclear system (**4**), consists of a central μ_6 Se^{2-} linked to six 8-coordinate samarium centers. Each Sm^{3+} is coordinated to three μ_4 Te_2^{-2} units,

and a μ_2 EO azide. The $Ln_6Se(Te_2)_6$ core is capped at both ends by 2 μ_4 oxos. The oxos form a tetrahedral unit, coordinating to three samarium core atom, and an additional 7-coordinate Sm^{3+} center. The 7-coordinate samarium cations, are bound to 2 pyridine ligands, 2 μ_2 EO azides, a μ_2 EE azide and a μ_3 EE azide. The latter two azides are connected to a $Na(Py)_3$ capping unit.

Bond types	**$(Py)_{16}Sm_8Se(O_2)Na_2(Te_2)_6(N_3)_8$. Bond Lengths (Å)**
Sm-Te	3.11-3.27
Sm-Se	3.03-3.05
Sm-N_3 (EO)	2.39-2.44
Sm-O (7 coordinate)	2.24
Sm-O (8 coordinate)	2.35-2.38
Sm-N_3 (EE)	2.40
Sm- μ_3 N_3 (EO)	2.47-2.53
Na-μ_3 N_3	2.50
Na-μ_2 N_3	2.44

Table 1.11. Summary of Bond Distances by Bond Type for $(py)_{16}Sm_8Se(O_2)Na_2(Te_2)_6(N_3)_8$, (**4**).

1.4 Thermolysis Studies

Thermolysis studies were done to investigate the solid state phase products of the previously described systems and the potential for rare earth azide clusters as precursors for lanthanide nitrides. Samples of **1-4** were sealed in quartz tubes, placed under vacuum and heated to 600°c for five hours at a rate of 20°C/min in a tube furnace. The end of each tube was placed in liquid nitrogen

during the experiments. Products **1a, 2** and **4** were the only samples to produce any microcrystalline products. Samples of **1b** and **3** detonated consistently, and obliterated their respective reaction vessels leaving only amorphous powders that did not diffract. **1a and 1b** decompositions produced small fires melting portions of the reaction tubes (deflagration). This distinction in detonation process is explainable by the comparatively larger quantity of flammable Py ligands in the clusters. The heat released from azide decomposition likely ignited the solvent molecules resulting in the observed deflagration. In each case, detonation occurred at the previously determined melting point temperatures for each system. **4** did not detonate up and through 600^{o}c. Black powders were recovered from **1a 2** & **4**. These were analyzed by powder X-Ray diffraction, while the cold part of the tube was washed with dry acetonitrile, and analyzed by GCMS spectrometry. In place of the hypothesized oxynitride and seleno-nitride products, Sm_2O_3 and Er_2O_3 phases were identified for **1a** and **2** while products from **4** were amorphous. Ph_2Se was identified by GCMS in **2**. A comparison of detonation temperatures and Ln metal to azide ratios (table 1.15) revealed clusters with greater azide concentrations were more prone to detonation. However, when metal ions were in equal quantity the clusters failed to detonate at all.

Compound	Detonation Temperature (°C)	Ln/N_3 Ion Ratio	Explosion Type
$(py)_{10}Sm_6O_2(N_3)_{16}Na_2(Py)_8 \cdot 7(Py)$	295	3:8	Deflagration
$(py)_8Ho_6O_2(N_3)_{12}(SePh)_2$	310	1:2	Detonation
$(py)_8Er_6O_2(N_3)_{12}(SePh)_2$	336	1:2	Detonation
$(py)_{10}Er_6O_2(Se_2)_2(N_3)_{10}$	312	3:5	Detonation
$(py)_{16}Sm_8SeO_4Na_2(TeTe)_6(N_3)_8$	NA	1:1	NA

Table 1.12. Summary of Detonation Temperatures, Lanthanide to Azide Ratios and Explosion types.

1.5 Conclusion

In conclusion, a new class of lanthanide oxyazide and oxychalcogenido azide cluster have been synthesized and fully characterized. Metathesis of Ln $(EPh)_x$ with NaN_3, and Na_2O produced hexanuclear systems encapsulated by azides. Additions of $Cd(SePh)_2$ elemental selenium and tellurium into the previously described reaction gave both hexanuclear and octanuclear systems. These species incorporated the chalcogenide in both the inner and outer coordination spheres, while failing to incorporate cadmium into the final structure. Finally, thermolysis studies lead to the isolation of Sm_2O_3 and Er_2O_3 phases. Decomposition methods varied between deflagration and detonation, while all azide clusters with Ln:N_3 ratios < 1.0 detonated/deflagrated, but those with Ln:N_3 ratios ≥1.0 were stable up to and through the typical sodium azide decomposition temperature.

References

[1] Committee on Prudent Practices for Handling, Storage, and Disposal of Chemicals in Laboratories, Board on Chemical Sciences and Technology, Commission on Physical Sciences, Mathematics, and Applications, National Research Council. (**1995**).Washington, D.C.: National Academy Press.

[2] Choi, J.; Gillan, E. G. *Inorg.Chem.* **2005**, 44,21, 7385.

[3] Su, Q.-N.; Tang, H.; Liu, Z-D *Huagong Keji* **2012**, 20,2, 58.

[4] Sima, J. *Coord. Chem. Rev.* **2006**, 250, 17, 2325.

[5] Escuer,A.; Aromi,G. *Eur. J. Inorg. Chem.* **2006**,23, 4721.

[6] Mautner, F. A.; Sudy, B.; Berger, C.; Fischer, R. C.; Vicente, R. *Polyhedron* **2012**, 42, 1, 95.

[7] Stamatatos,T. C.; Christou, G.;*Inorg.Chem.* **2009**, 48,8, 3308.

[8] Ribas, J *Coord. Chem. Rev.* **1999**, 195, 1027.

[9] Meyer, F.;Kozlowski, H.*Comprehensive Coordination Chemistry Review* **2003**, 6, 247.

[10] Tandon, S. S.; Bunge,S. D.; Sanchiz, J.; Thompson, L.K. *Inorg.Chem.* **2012**, 51, 5, 3270.

[11] Adhikary, C.; Koner, S. *Coord. Chem. Rev.* **2010**, 254, 2933.

[12] Schurz, C.; Schleid, T. *J. of Solid State Chem.* **2010**, 183, 2253.

[13] https://engineering.purdue.edu/~propulsi/propulsion/comb/propellants.html

[14] Evans, W. J.; Kozimor, S. A.; Ziller, J. W. *Science* **2005**, 309,1835.

[15] King, D. M.; Tuna, F.; McInnes, E. J. L.; McMaster, J.; Lewis, W.; Blake, A. J.; Liddle, S. T. *Science* **2012**, 337, 717.

[16] Thomson,R. K.; Cantat, T.; Scott, B. L.; Morris, D. E.; Batista, E. R.; Kiplinger, J. L. *Nat. Chem.* **2010**, 2, 9, 723.

[17] Arai, Y.; Morihira, M.; Ohmichi, T. *J. Nucl. Mater.* **1993**, 202,1, 70.

[18] Zerr, A.; Miehe, G.; Riedel, R. *Nat. Mater.*, **2003**, 2,185.

[19] Razeghi, M.; McClintock, R. *J. Cryst. Growth* **2009**, 311,10, 3067.

CHAPTER 2. Sodium Capped Lanthanide Selenido Clusters

2.1 Introduction

Lanthanide materials offer a number of distinct advantages as emission sources. Long lifetimes, consistent emission spectra, and low phonon energies in chalcogenide systems are but a few of them. The applications for rare earths range from upconversion nanocrystals[1] to fiber optic wave guide amplifiers (FOWA).[2] In the case of FOWAs, lanthanides are employed as dopants in a variety of host matrices.[3,4,5,6] Excitation of the lanthanide doped material is achieved through a pumping system (Figure 2.1),[7] pushing the Ln^{3+} into an excited emissive state that can amplify a desired signal within a specific wavelength region. The region of amplification is determined by a combination of the emission spectrum for selected lanthanides, and the allowed transmission window of the host material.[8] The most commonly used lanthanides erbium [9] and neodymium,[10] amplify in the 1.5 & 1.8 μm regions of the spectrum respectively. The former serves as a standard in the telecommunication industry.

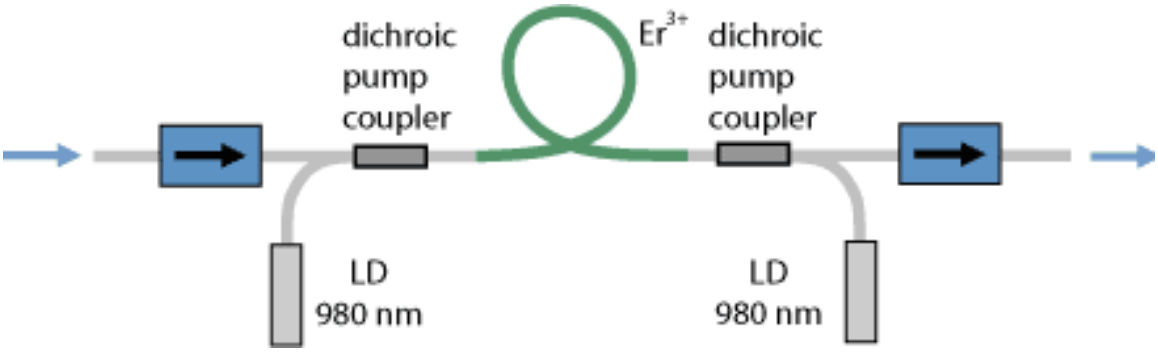

Figure 2.1. Erbium-Doped Fiber Amplifier Schematic.

In an effort to lower production costs and broaden the available transmission window, polymer based fibers have been studied as an alternative host to glasses.[11] This shift brought several complications. To begin with, previously used solid state lanthanide sources (lanthanide halides and nitrides) displayed a tendency to aggregate[12] and phase separate in the nonpolar polymer matrixes. Attempts at developing alternative molecular based lanthanide sources varied the ligand functional groups to improve dispersion.[13] Unfortunately, these materials displayed emissions intensities too low for application.[14] This was attributed to two factors. First, stabilizing ligands used to impart greater solubility in the host materials possessed large quantities of vibrational quenching groups (C-H ,O-H, N-H) near the emissive centers. Second, the bulkier ligand groups occupied significant volumes in the polymer matrixes while possessing very few emissive centers. This resulted in systems suffering from deleterious emissive effects due to higher ligand concentrations[15] and low concentrations of lanthanide (changes in the refractive index of the polymers).

Lanthanide chalcogenide clusters offer a sound solution to these problems. The well documented low phonon energies of Ln-E bonds,[16] the high lanthanide concentrations,[17] and the versatile cluster surface modification abilities, resulted in systems with quantum efficiencies that approached solid state intensities[15] while displaying the desired matrix compatibility. In addition, the capacity to selectively express lanthanide emissions wavelengths by varying the phonon energy environment[18] offered a powerful tool for designing industry specific materials. In an effort to explore the possibility of preparing higher

nuclearity lanthanide chalcogenide clusters and to understand the relationships between nuclearity, surface anions, and emissions quantum efficiencies, sodium azide was introduced into a chalcogenide rich lanthanide environment to improve reagent solubility and increase product nucleation time.

2.2. $(py)_{16}Ln_{17}NaSe_{18}(SePh)_{16}$: Synthesis, Structure, and Discussion.

The title family of clusters was produced by two related schemes. Initially $Ln(SePh)_3$ in the presence of excess lanthanide was reacted with selenium and sodium azide to produce $(py)_{16}Ln_{17}NaSe_{18}(SePh)_{16}$ [Ce=(**1**), Pr=(**2**), Nd= (**3**)]. In order to evaluate the role of NaN_3 in driving this chemistry, the same reaction with Na(SePh) substituted for sodium azide was performed and resulted in the formation of the identical products. The two schemes shown in Scheme 2.1 did display distinct crystallographic and chemical features.

$$\textbf{a) } 6.7Ln + 3.0(SePh)_2 + .1Hg \xrightarrow[3NaN_3 + 5.7Se]{40ml\ Py} (Py)_{16}Ln_{17}NaSe_{18}(SePh)_{16}$$

$$\textbf{b) } 6.7Ln + 3.0(SePh)_2 + .1Hg \xrightarrow[3NaSePh + 5.7Se]{40ml\ Py} (Py)_{16}Ln_{17}NaSe_{18}(SePh)_{16}$$

Ln= Ce, Pr, Nd

Scheme 2.1. Synthesis of $(py)_{16}Ln_{17}NaSe_{18}(SePh)_{16}$.

Products from **1a** displayed diffraction patterns extending near the 0.7 Å, limit of the radiation source, (Mo kα). This resulted in crystals with a high degree of order, very low R factors and disordering (Fig. 2.2). Conversely, the polyycrystalline products from **1b**, displayed poorer crystallinity and were identified by unit cell comparison with **1a** products only. However, a comparison

of the percent yields for the **1a** products (**17, 42 & 35**), with the **1b** products (**81, 93, 76**), clearly showed a higher product yield for **1b**. Additionally, no azide species was ever recovered from the **1a** scheme, however the presence of $(Py)_2Na_2(SePh)_2$ was confirmed in **1b** by the isolation and XRD of colorless rod like crystals.

The core of the $(py)_{16}Nd_{17}NaSe_{18}(SePh)_{16}$ system (Figure 2.3. **3**), is a spherically shaped cluster built upon a central neodymium ion that rests on a crystallographic two-fold axis and is surrounded by 8 μ_5-selenido ligands. The selenido ligands are then encapsulated by 16 neodymium, ions eight of which are 8 coordinate while the other eight are 7 coordinate. In both cases the encapsulating neodymium ion coordination spheres are saturated by μ_5 selenido, μ_3-selenido, μ_3 -selenolates, μ_4-selenolate, and pyridine ligands. A sodium ion occupies a surface site where it is bound on one side to an exposed selenido and two SePh ligands (bridging two neodymium ions) while two pyridine ligands are coordinated on the opposing side. The cluster consists of two crystallographically equivalent sodium ion occupation sites, that are partially occupied (50%). These sites sit on a two-fold axis, and depending upon the sodium ion's occupation, the two SePh ligands and pyridine ligands display varying amounts of disorder. If the sodium site is unoccupied the phenyl groups of two SePh ligands are directed inward toward the sodium ion void or outward when the ion is present. The pyridine ligands display similar disorder, acting as lattice solvents within the void when sodium is not present.

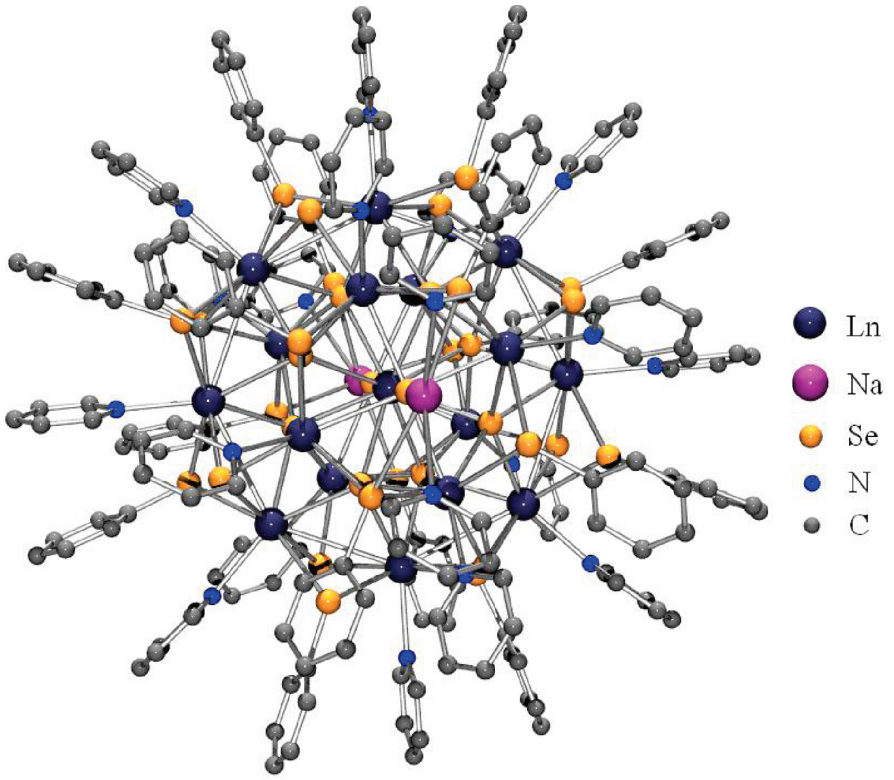

Figure 2.2. POV-Ray Crystal Structure of $(py)_{16}Ln_{17}NaSe_{18}(SePh)_{16}$.

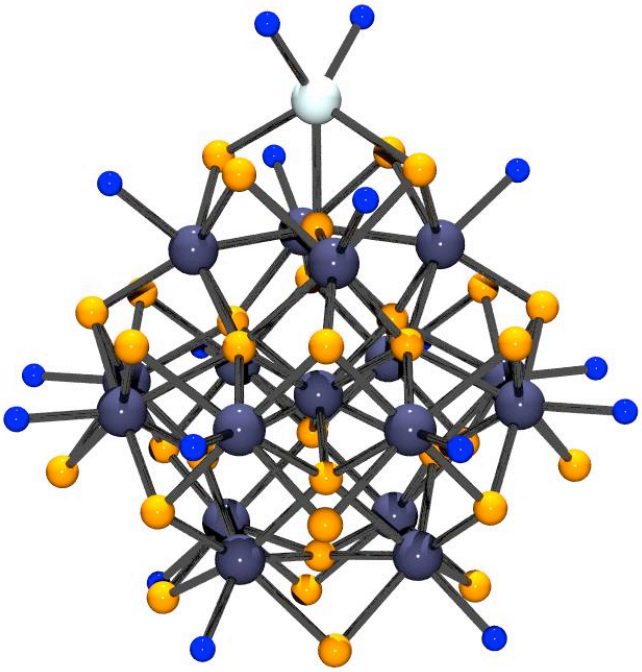

Figure 2.3. POV-Ray Crystal Structure of $(py)_{16}Nd_{17}NaSe_{18}(SePh)_{16}$ Core Side View.

Empirical Formula	$C_{231}H_{215}N_{27}NaCe_{17}Se_{34}$	$C_{231}H_{215}N_{27}NaNd_{17}Se_{34}$
Formula Weight	8458.97	8529.01
Temperature (K)	100	100
Wavelength (Å)	0.71073	0.710703
Crystal System	monoclinic	monoclinic
Space Group	C2/c	C2/c
a (Å)	22.5455(11)	22.4939(13)
b (Å)	42.056(2)	41.963(2)
c (Å)	31.0886(16)	30.9247(17)
β (deg)	108.099(1)	108.129(1)
volume ($Å^3$)	28019(2)	27741(3)
Density (calculated) (g/cm^{-3})	2.005	2.042
Z	4	4
Final R indices [I>2sigma(I)]	R1=.0509 WR2= .1426	R1=.0516 WR2= .1425

Table 2.1. Crystal Data and Structure Refinement for $(py)_{16}Ce_{17}NaSe_{18}(SePh)_{16}$ and $(py)_{16}Nd_{17}NaSe_{18}(SePh)_{16}$

One of the unique features of the Ln_{17} system is the presence of both internal and surface lanthanide ions as well as the unique bond lengths and coordinations that permit a comparison with solid state Nd_2Se_3 species.[19] The key bond lengths and angles for **3** are summarized in tables 2.2 and 2.3 and reveal a narrow neodymium-selenium bond length range (3.131Å - 3.138 Å, avg. 3.135 Å), as well as a severely distorted coordination geometry for the internal neodymium ion.

Bond	Bond Distance (Å)	Bond	Bond Distance (Å)
Nd(1)-Se(8)’	2.871	Nd(5)-Se(15)’	3.147
Nd(1)-Se(2)	2.983	Nd(5)-Se(10)	2.987
Nd(1)-Se(14)’	3.03	Nd(5)-Se(1)	2.907
Nd(1)-Se(5)	2.888	Nd(5)-Se(25)’	2.981
Nd(1)-Se(12)	3.079	Nd(5)-Se(5)	2.877
Nd(1)-Se(4)’	3.114	Nd(5)-N(5)	2.636
Nd(1)-N(1)	2.549	Nd(5)-Se(27)	2.946
Na(1A)-N(9A)	3.363	Nd(5)-Se(17)	3.005
Na(1A)-Se(28)’	3.694	Na(1A)-Se(26)’	3.339
Na(1B)-N(9B)	3.385	Na(1B)-Se(25)’	3.298
Na(1B)-Se(27)/Se(27)’	3.184	Na(1A)-N(9A)’	3.363
Na(1A)-Se(9)	3.049	Na(1A)-Se(26)	3.339
Na(1A)-Se(28)	3.694	Na(1B)-N(9B)’	3.385
Na(1B)-Se(10)	3.141	Na(1B)-Se(25)	3.298
Nd(9)-Se(2)	3.13	Nd(9)-Se(1)’	3.138
Nd(9)-Se(4)’	3.132	Nd(9)-Se(3)	3.133
Nd(9)-Se(2)’	3.13	Nd(9)-Se(1)	3.138
Nd(9)-Se(4)	3.132	Nd(9)-Se(3)’	3.133

Table 2.2. Bond Distances for $(py)_{16}Nd_{17}NaSe_{18}(SePh)_{16}$

Coordination Angle	Angle (º)	Coordination Angle	Angle (º)
Se(2)-Nd(9)-Se(2)#1	123.94(4)	Se(4)#1-Nd(9)-Se(3)	140.82(2)
Se(2)-Nd(9)-Se(4)	140.06(2)	Se(3)#1-Nd(9)-Se(3)	123.99(4)
Se(2)#1-Nd(9)-Se(4)	71.39(2)	Se(2)-Nd(9)-Se(1)	70.69(2)
Se(2)-Nd(9)-Se(4)#1	71.39(2)	Se(2)#1-Nd(9)-Se(1)	141.00(2)
Se(2)#1-Nd(9)-Se(4)#1	140.06(2)	Se(4)-Nd(9)-Se(1)	76.82(2)
Se(4)-Nd(9)-Se(4)#1	123.10(4)	Se(4)#1-Nd(9)-Se(1)	77.02(2)
Se(2)-Nd(9)-Se(3)#1	77.52(2)	Se(3)#1-Nd(9)-Se(1)	140.45(2)
Se(2)#1-Nd(9)-Se(3)#1	76.98(2)	Se(3)-Nd(9)-Se(1)	71.04(2)
Se(4)-Nd(9)-Se(3)#1	140.82(2)	Se(2)-Nd(9)-Se(1)#1	141.00(2)
Se(4)#1-Nd(9)-Se(3)#1	70.86(2)	Se(2)#1-Nd(9)-Se(1)#1	70.69(2)
Se(2)-Nd(9)-Se(3)	76.98(2)	Se(4)-Nd(9)-Se(1)#1	77.02(2)
Se(2)#1-Nd(9)-Se(3)	77.52(2)	Se(4)#1-Nd(9)-Se(1)#1	76.82(2)
Se(4)-Nd(9)-Se(3)	70.86(2)	Se(3)#1-Nd(9)-Se(1)#1	71.04(2)
Se(3)-Nd(9)-Se(1)#1	140.45(2)		

Table 2.3. Coordination Angles for the Internal Nd^{3+} in $(py)_{16}Nd_{17}NaSe_{18}(SePh)_{16}$

The narrow bond lengths designated in red in Table 2.2 and non directional geometry for the internal Nd^{3+} (Figure 2.5), are a departure from the solid state counterpart (Nd_2Se_3). Nd_{17} and Nd_2Se_3 display internal neodymium ions with 8 selenido coordinations. However, the internal neodymium of the solid state product exhibits a wider Nd-Se bond length range (2.967- 3.173 Å), as well as a trigonal dodecahedron coordination sphere.

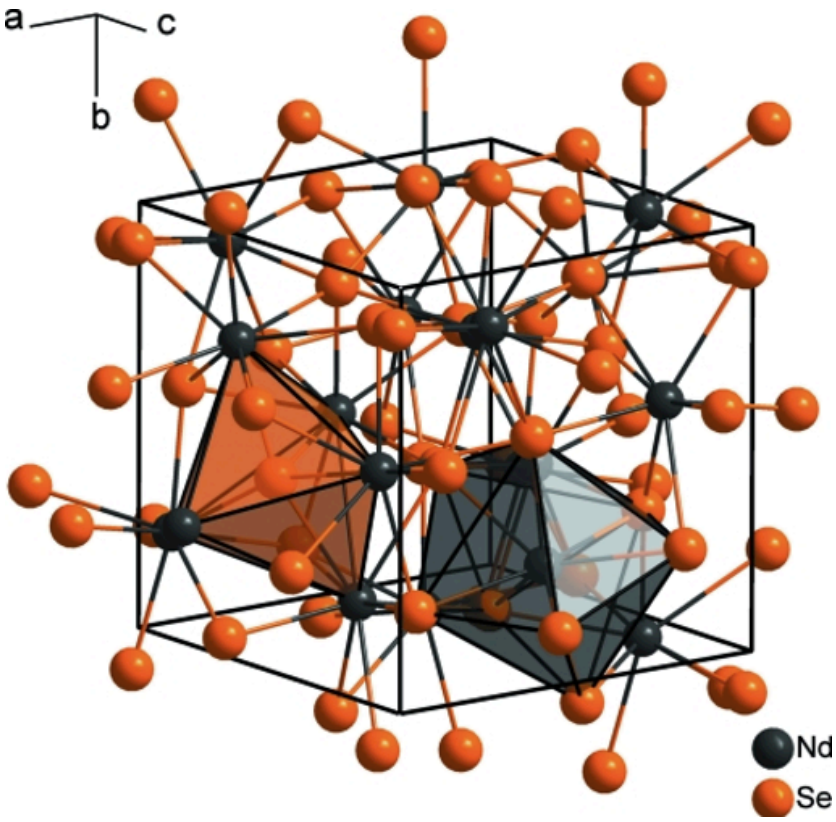

Figure 2.4. Nd_2Se_3 Structure.

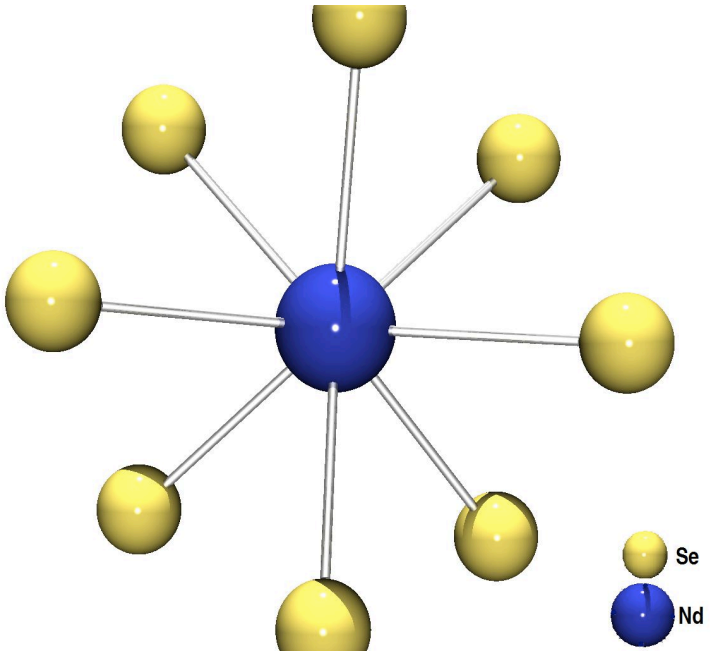

Figure 2.5. 8-Coordinate Internal $NdSe_8$ Unit of $(py)_{16}Nd_{17}NaSe_{18}(SePh)_{16}$.

Nevertheless, Nd_{17}'s similar coordination with Nd_2Se_3 and dissimilar coordination with other Nd-Se clusters produced through $Ln(EPh)_3$ + E reactions ($(THF)_8Nd_8Se_6(SePh)_{12}$,7-coordinate) led to the assertion that the presence of sodium in the Ln_{17} structure must play a role in stabilizing this structure.

Comparative experiments using alkali metals, alkali metal azides, alkali selenolates (Na, K, Li, NaN_3, KN_3, KSeph, and LiSePh) and lanthanides of varying ionic radii (Sm^{2+}, Sm^{3+}, Gd^{3+}, Er^{3+}, Yb^{3+}, Eu^{2+}, Dy^{3+}, and Ho^{3+}), were performed to evaluate the role of sodium in stabilizing $Ln_{17}Se$ structures. Only the well-studied Ln_8Se_6[20] and the respective alkali selenolates and selenides were isolated.

Observations from the comparative experiments, coupled with the reproducible differences in product crystallinity, yield and isolated phases between NaN_3 and NaSePh, provided support for the assertion that both sodium and azide ions play key roles in directing the formation of the Ln_{17} species. The most likely rationale for this phenomenon is that the marginally soluble nature of the azide salt in organic solvents, provides a slow delivery system for the sodium ion, while introducing a readily displaced and weakly coordinated anion into the chalcogenide system. This interaction favors the formation of the readily isolated $(py)_2Na(SePh)_2$, while providing additional anions that can readily form soluble lanthanide azido selenolate in solution (Figure 2.6).

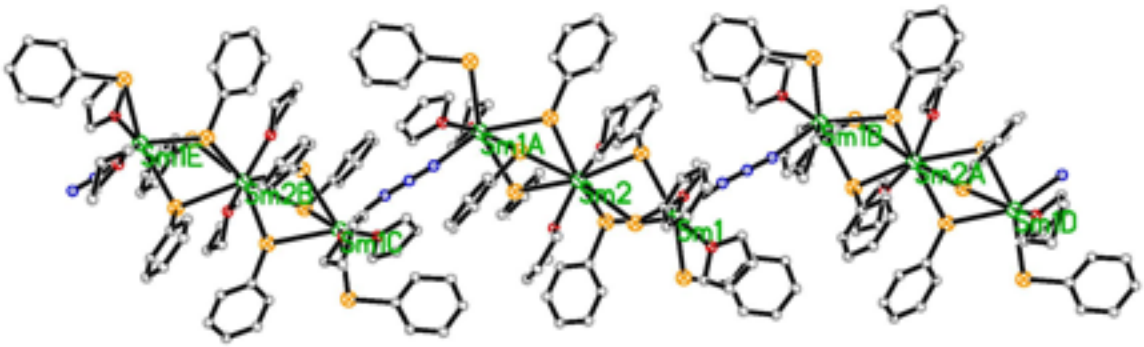

Figure 2.6. ORTEP Structure of $[(THF)_4\ Sm_3(SePh)_4(N_3)]_3$ Species.

The production of lanthanide azido selenolate intermediates is also influential in the formation of the Ln_{17} system. The structure depicted in Figure 2.6 is a samarium selenolate trimer with a single EE bridging azide. The product was isolated by adding a dilute iodide solution (10 mL of .05M I_2 in THF) to a concentrated $Sm(SePh)_3$ + NaN_3 reaction in order to coordinate with sodium ions. The Ln-SePh bridging moiety is a common occurrence and has been documented numerous times.[21,22] However, the presence of the bridging azide, does support the contention that stable azide incorporating intermediates are present and coordinating to large Ln species in solution. The larger quantity of lanthanides in close proximity due to the azide bridging between trimers allows larger Ln-Se fragments to form in solution when compared with previous work and explains Ln_{17} larger nuclearity. Next, the concentration of azide ions in solution, prevented the otherwise insoluble Ln-E species from precipitating by shifting the equilibrium towards the more soluble azide selenolates. This allowed larger numbers of fragments to coalesce and form the Ln_{17}. Finally, the matching of the sodium cations in limited number, with the structurally generated voids,

and the elimination of excess SePh and Se via Na_2Se and $(py)Na_2(SePh)_2$ formation provided the ideal environment for producing a system of greater nuclearity and high crystallinity.

2.3. Absorption and Emissions Studies of $(py)_{16}Ln_{17}NaSe_{18}(SePh)_{16}$.

Due to the potential utility of $(py)_{16}Nd_{17}NaSe_{18}(SePh)_{16}$ as a dopant in polymer amplifiers and a continuing interest in defining Ln-E cluster structure/ emission properties, a series of absorption and NIR emission studies were conducted. Absorption spectra for all three clusters in THF (Figures 2.7-2.9) displayed typical absorption transitions for solid state cerium praseodymium and neodymium 3^+ ions.[23] $(py)_{16}Ce_{17}NaSe_{18}(SePh)_{16}$ display offers a clear single broad absorption edge maxima at 442 nm and a transition at ~600 nm. This translates into a 2.81 eV band gap and is larger then the 1.85 eV value found for Ce_2Se_3.[24] Nevertheless, The value for $(py)_{16}Ce_{17}NaSe_{18}(SePh)_{16}$ is consistent with the band gap of a semiconducting material through an F to D band transition. The absorption peaks as well as the respective energy transitions for **2** and **3** are shown in Tables 2.4 & 2.5. The relatively few absorptions and low intensities of peaks in **1** and **2** can be rationalized by the lack of available energy transitions, (few energy states), within the visible-NIR absorption window for cerium and praseodymium ions in the 3^+ oxidation states. Given the absorption data only **3** was a viable system for photoluminescence studies.

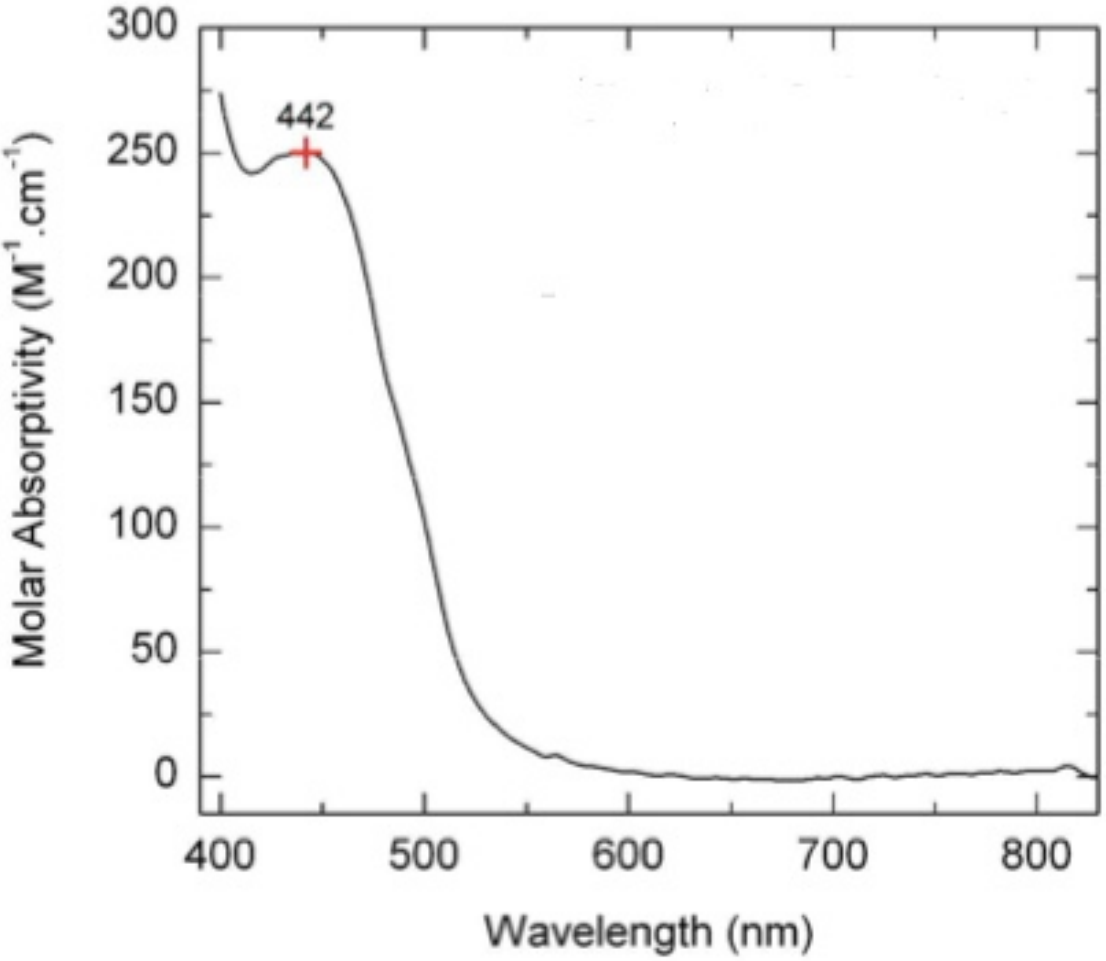

Figure 2.7. $(py)_{16}Ce_{17}NaSe_{18}(SePh)_{16}$ Absorption Spectrum.

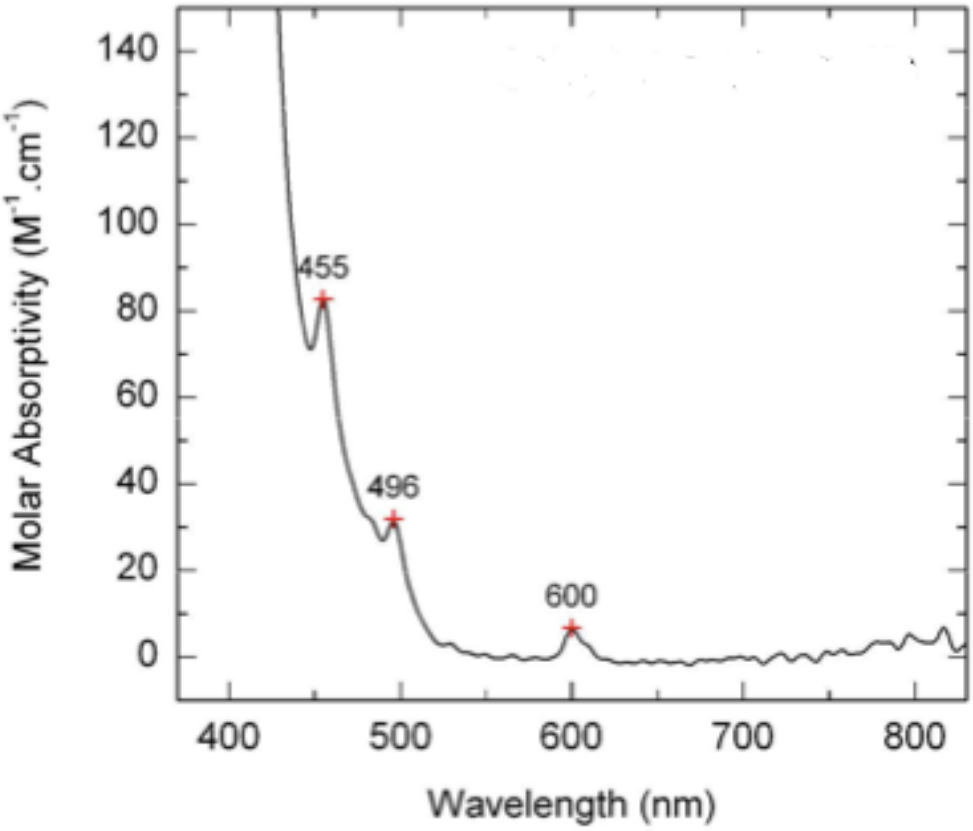

Figure 2.8. $(py)_{16}Pr_{17}NaSe_{18}(SePh)_{16}$ Absorption Spectrum.

Absorption Peak (nm)	Energy Transition
455	$^3H_4 \rightarrow {}^3P_2$
496	$^3H_4 \rightarrow {}^3P_6$
600	$^3H_4 \rightarrow {}^1D_2$

Table 2.4. Absorption Peaks & f-f Transitions for $(py)_{16}Pr_{17}NaSe_{18}(SePh)_{16}$.

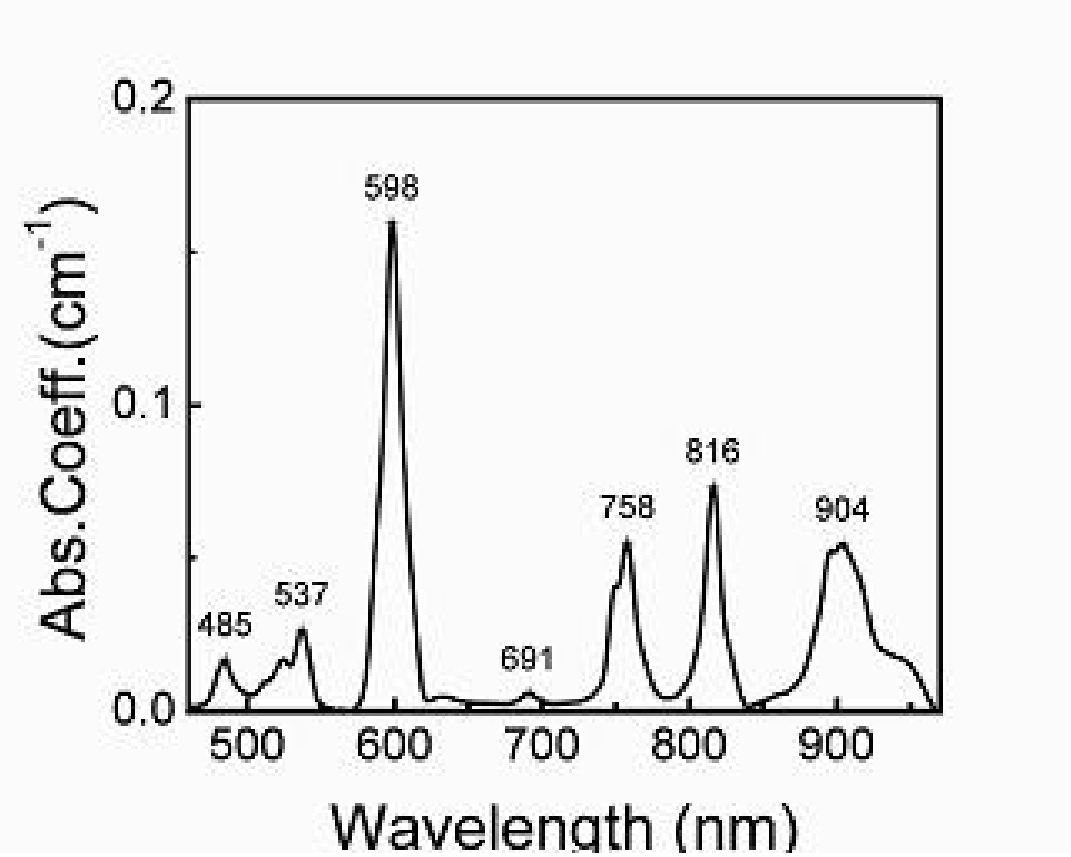

Figure 2.9. $(py)_{16}Nd_{17}NaSe_{18}(SePh)_{16}$ Absorption Spectrum.

Absorption Peak (nm)	Energy Transition
485	$^4I_{9/2} \rightarrow {}^2P_{1/2}$
537	$^4I_{9/2} \rightarrow {}^4G_{9/2}$
598	$^4I_{9/2} \rightarrow {}^4G_{5/2}$
691	$^4I_{9/2} \rightarrow {}^4F_{9/2}$
758	$^4I_{9/2} \rightarrow {}^4S_{3/2}$
816	$^4I_{9/2} \rightarrow {}^4F_{5/2}$
904	$^4I_{9/2} \rightarrow {}^4F_{3/2}$

Table 2.5. Absorption Peaks & f-f Transitions for $(py)_{16}Nd_{17}NaSe_{18}(SePh)_{16}$.

The strongest f-f absorption transition in **3** (598 nm) is found in all neodymium complexes and has been designated as a hypersensitive transition, ($^4I_{9/2} \rightarrow {}^4G_{5/2}$). Transition sensitivity, (variances in broadness and intensity of the peak as well as shifts in energy) arise from changes in solvent and coordination environment. The documented divergence of the $^4I_{9/2} \rightarrow {}^4G_{5/2}$ transition with coordinated pyridine and non coordinated solid state examples,[25] along with the possibility of increasing non radiative energy transfer through an increased Stokes shift, supported the notion that the $^4I_{9/2} \rightarrow {}^4G_{5/2}$ was an unsuitable choice for photon pumping. As a result, the 904 nm transition ($^4I_{9/2} \rightarrow {}^4F_{3/2}$), was targeted as the photon stimulated excited state for emission studies of **3**.

Dr. G. Ajith Kumar formerly of the Riman group in the department of material science and engineering at Rutgers university extracted the Judd-Ofelt parameters, (Ω) [26 27] from the absorption spectrum in order to calculate ($\tau_{(rad)}$). The results were the determination of three Ω_t values through a least square fitting between the measured oscillator strength and the theoretical oscillator strength performed by Dr. Kumar.[31,32,28] The quality of the fit was determined by the deviation between the experimental and theoretical oscillator values referred to as the RMS (equation 2.1) where Δf is the difference between the oscillator strengths, while N and m represent the number of transitions and fitting parameters.The theoretical and experimentally determined oscillator values for $(py)_{16}Nd_{17}NaSe_{18}(SePh)_{16}$ mixed absorption bands (table 2.6), resulted in Judd-Ofelt parameters with values of Ω_2= 0.928 x 10^{-20} cm^2, Ω_4= 2.548 x 10^{-20} cm^2, Ω_6= 0.479 x 10^{-20} cm^2; and an RMS = 0.529 x 10^{-6}.

$$RMS = \sqrt{\frac{(\sum \Delta f)^2}{(N-m)}}$$

Equation 2.1. RMS Equation.

Bands	λ(nm)	Energy(cm^{-1})	$f_{cal}(10^{-6})$	$f_{exp}(10^{-6})$
$^4G_{9/2}+^2K_{15/2}+^2G_{9/2}$	485	20619	0.792	0.714
$^4G_{7/2}$	537	18622	1.539	1.359
$^4G_{5/2}$	598	16722	4.978	4.999
$^4F_{9/2}$	691	14472	0.101	0.194
$^4F_{7/2} + ^4S_{3/2}$	758	13193	0.879	1.230
$^2H_{9/2} + ^4F_{5/2}$	816	12255	1.667	1.109
$^4F_{3/2}$	904	11062	1.061	1.862

Table 2.6. Theoretical and Experimentally Determined Oscillator Values for $(py)_{16}Nd_{17}NaSe_{18}(SePh)_{16}$ Mixed Absorption Bands.

Comparative emission measurements were collected on **3**, and LaF_3:Nd (0.5%) nanoparticles (10-50nm diameter) . The LaF_3:Nd nanoparticles have been well documented as having a 95% quantum efficiency and served as a viable standard[29] for evaluating the emission intensities and quantum efficiency of **3**.

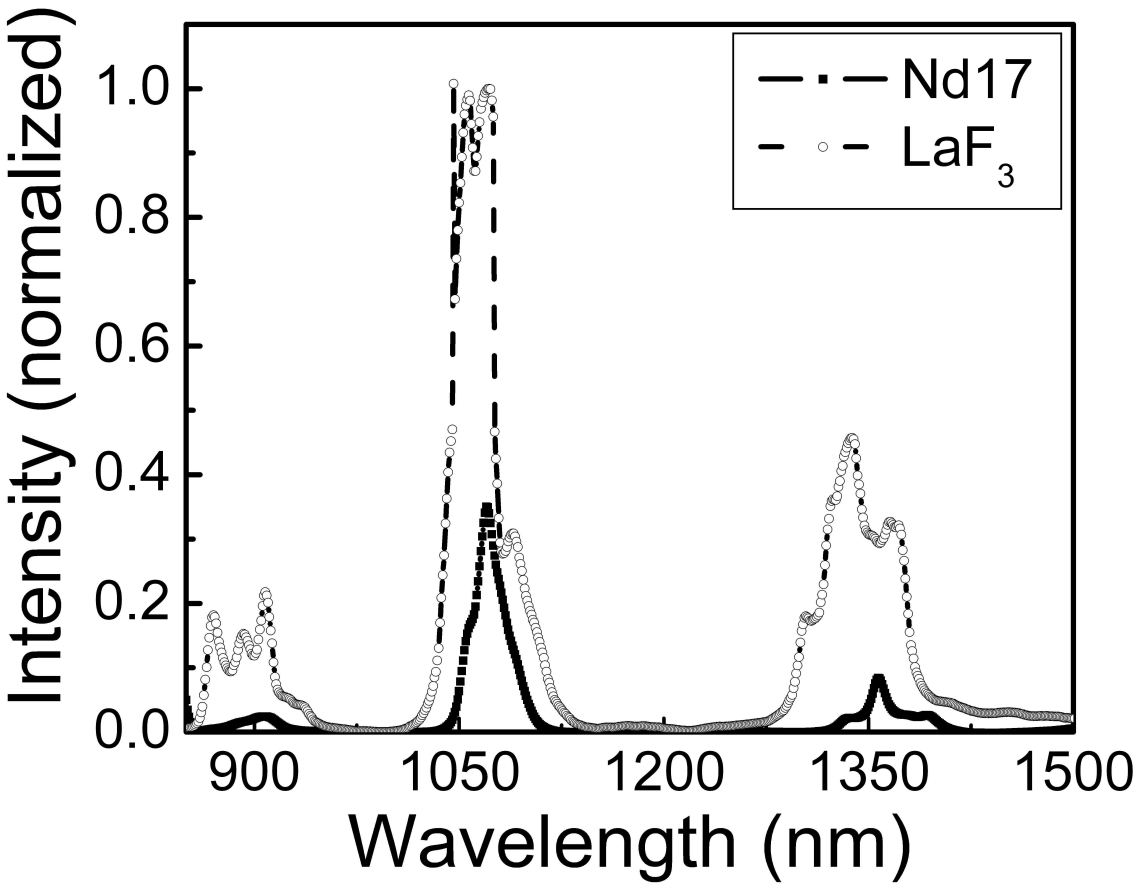

Figure 2.10. Emission Spectrum of $(py)_{16}Nd_{17}NaSe_{18}(SePh)_{16}$ Compared to LaF_3:Nd (0.5%) Nanoparticles

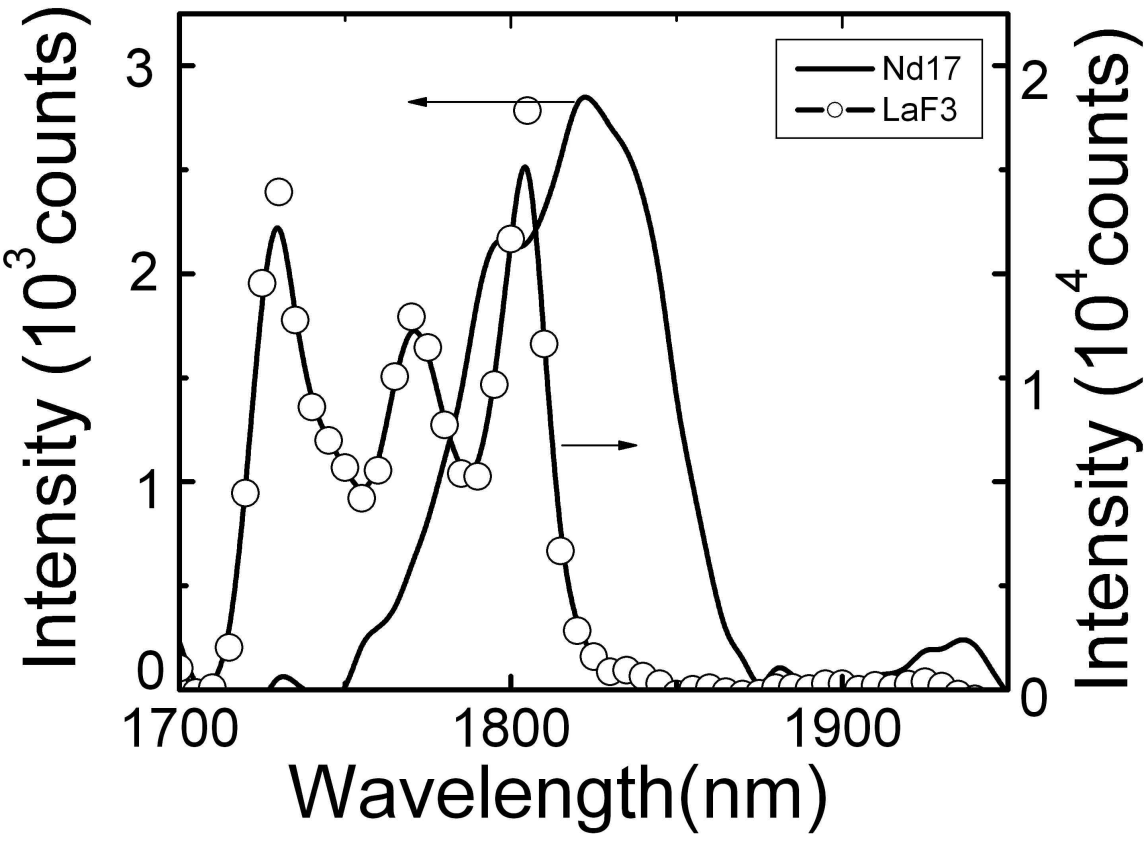

Figure 2.11. Low Energy Emission Spectrum of $(py)_{16}Nd_{17}NaSe_{18}(SePh)_{16}$ Compared to LaF_3:Nd (0.5%) Nanoparticles

Emission Peak (nm)	Energy Transition
907	$^4F_{3/2} \rightarrow {}^4I_{9/2}$
1070	$^4F_{3/2} \rightarrow {}^4I_{11/2}$
1357	$^4F_{3/2} \rightarrow {}^4I_{13/2}$
1822	$^4F_{3/2} \rightarrow {}^4I_{15/2}$

Table 2.7. Emission Peaks and f-f Transitions for $(py)_{16}Nd_{17}NaSe_{18}(SePh)_{16}$.

Along with a cascade of well resolved emission bands, the comparative solid state emission spectra (figure 2.10), revealed a unique emission feature with interesting implications. The majority of the intensities for the molecular species were considerably less intense then the solid state product as expected. However, the 1.8 μm (1822 nm) emission observed in **3**, was unique for several reasons. First, the $^4F_{3/2} \rightarrow {}^4I_{15/2}$ transition has been observed intermittently in Nd solid state products[30,31] and select Ln-E clusters.[32] [33] Nevertheless, it has been distinctly absent from the majority of higher nuclearity Ln-E cluster systems.[34, 35,36] Second, a side by side qualitative examination of the normalized low energy emissions for the two species (figure 2.11), displays a considerably greater intensity for **3**. This supports the notion that molecularly produced cluster species can provide high intensity emissions consistent with solid state products.

In order to have an accurate and comparable measure of a product's emissive performance, the quantum efficiency which reflects the extent to which non-radiative processes dominate the relaxation from a selected excited state had to be derived (Equation 2.2).

$$QE(\Phi) = \frac{\tau_{fl}}{\tau_{rad}}$$

Equation 2.2. Experimental Quantum Efficiency Determination.

The QE determination of **3** for the $^4F_{3/2} \rightarrow {}^4I_{11/2}$ (1070 nm emission), (also performed by Dr. Kumar) began with the extraction of the fluorescence decay time, (τ_{fl}) from the measured decay curve, (figure 2.12). The decay curve was

then fitted with a Monte Carlo Model[37] to yield a decay time of 330 μs for the 1070 nm emission. The fitting took into account all the cooperative energy transfer and cross relaxation processes between neodymium atoms located in the various crystallographic sites. The experimental decay time along with the calculated radiative decay time[31,32] resulted in a calculated quantum efficiency of 35% for **3**.

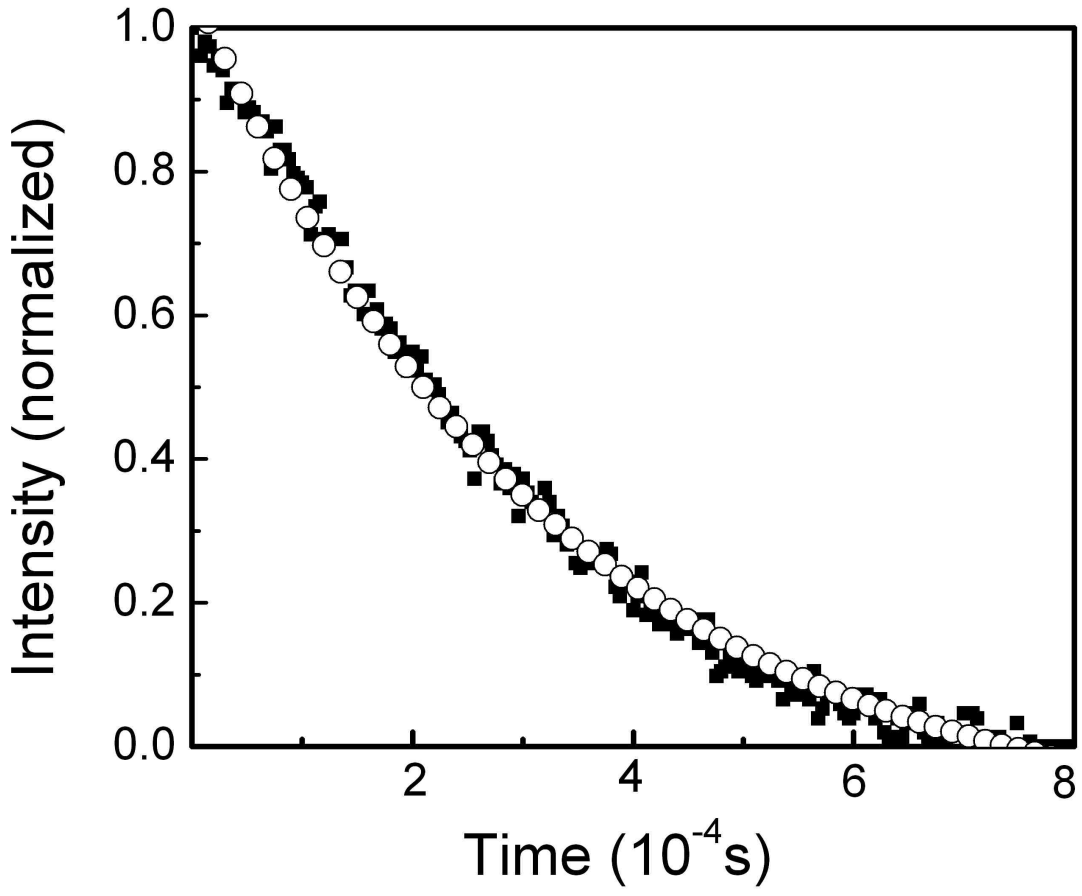

Figure 2.12. Monte-Carlo Model Fitted Fluorescence Decay Curve of $(py)_{16}Nd_{17}NaSe_{18}(SePh)_{16}$ 1074 nm Emission.

As with many properties in science the interrelationship between structure and QE can offer profound insights into both. The smaller the ΔE between the

emissive and highest sub-level of the ground or receiving multiplet, the easier it is for the gap to be “closed” by non-radiative relaxation processes (e.g, through high phonon energy bonds vibration, C-H, N-H, or O-H). Since the fluorescence lifetimes of lanthanide materials are mainly dependent upon the lattices’ vibrations and the Ln-Ln internuclear distance, **3** provided the opportunity to investigate the effect of both on the quantum efficiency.

Compound/Material	QE	CH/Nd^{3+}	Nd-Nd Distance (Å)
$(THF)_8Nd_8O_2Se_2(SePh)_{16}$	16%	17	3.82
$(py)_{18}Nd_{12}O_6(SeSe)_4(SePh)_4$...	12%	12	3.77
$(py)_{16}Nd_{17}Se_{17}Na(SePh)_{18}$	35%	10	3.75

Table 2.8. Nd-Se Cluster Properties.

When the efficiencies for $(py)_{18}Nd_{12}O_6(SeSe)_4(SePh)_4$ (**Nd_{12}**), (12%) and $(THF)_8Nd_8O_2Se_2(SePh)_{14}$ (**Nd_8**), (16%) are compared to the 35% value found for **3** a clear illustration of the correlation between the increasingly larger nuclearity molecules and brighter photo-physical properties can be seen (Figure 2.13). This assertion is understandable given that the number of emissive sources and QE increases with each system. In neodymium compounds, the $^4F_{3/2}$ - $^4I_{11/2}$ transition (1070 nm emission) is quenched by the third order vibrational overtone of C-H bonds. The number of C-H bonds found in the ligands (THF, Py, SePh) that are directly bound to the cluster surfaces of **Nd_{12}**, **Nd_8** and **3** (140,136 and 167 respectively), result in averages of 12, 17 and 10 for the number of C-H per neodymium ion in all three systems. Therefore, it is a reasonable conclusion that

one of the factors responsible for the higher quantum efficiencies in **3** is the decrease in non-radiative loses due to fewer quenching groups directly coordinated to the emissive centers.

An additional consideration in understanding the QE cluster dynamic is the lattice composition. As a rule of thumb, anions that have low phonon characteristics lead to brighter emissive materials. Typically oxide ligands generate high-phonon energy lattices, while the heavier chalcogenides provide low-phonon environments. In **Nd_8**, there are 50 Nd-Se and six Nd-O bonds; in **Nd_{12}** there are 56 Nd-Se bonds and 24 Nd-O bonds, and 107 Nd-Se bonds in **3**. Based upon these observation it is appropriate to say that the absence of high phonon anions, and the saturation of low phonon anions within the lattice of **3** is a significant contributor to its greater QE when compared with **Nd_8**, & **Nd_{12}**.

Finally, Nd-Nd separation dependence on QE provides the most ambiguous evidence for its relevance. The shortest Nd-Nd separations for **Nd_8**, and **3**, are 3.82 Å, and 3.75 Å respectively. Given that **3** has the shortest Nd-Nd distance, the highest QE, and no observed concentration quenching effects, it is reasonable to suggest that separation between Nd atoms within a selenide lattice should be less than 3.8 Å to maximize their QEs.

2.4. Conclusions.

Spectroscopically silent metal azide salts can be used to preferentially generate the larger molecular lanthanide cluster, $(py)_{16}Ln_{17}NaSe_{18}(SePh)_{16}$ by forming a lanthanide azido selenolate intermediate, shifting species solubility and

influencing product precipitation. The neodymium analogue is a particularly bright NIR emission source, that emits with high intensity in the 1.8 μm range of the NIR spectrum and a 35% quantum efficiency for the $^4F_{3/2}$ - $^4I_{11/2}$ transition (1070 nm emission) . The combined influence of a high concentration of neodymium encapsulated by a low-phonon environment, relatively few C-H bonds close to neodymium and significant Nd-Nd separation, make the systems quantum efficiency significantly higher than neodymium systems with higher quantities of oxide and C-H containing ligands.

References

[1] Yang, D.; Dai, Y.; Ma, P.; Kang, X.; Shang, M.; Cheng, Z.; Li, C.; Lin, J. *J. Mater. Chem.*, **2012**, 22,38, 20618-20625.

[2] Desurvire, E.; Simpson, J. R; Becker, P. C. Opt. Lett.,**1987,** 12,11, 888.

[3] Kuriki, K.; Kobayashi, T.; Imai, N.; Tamura, T.; Nishihara, S.; Tagaya, A.; Koike, Y.; Okamoto, Y. *IEEE Photonics Technol. Lett.,* **2000**, 12, 989.

Marzouk, M. A. *Journal of Molecular Structure.,* **2012**,1019, 80-90.

Kassab, L. R. P.; Assumpcao, T. A. A.;Czaja, P.; Gondek, E.;Plucinski, K. J. *J. Mater. Sci. Electron.*, **2012**, 23,5, 1122-1125.

[6] Zaitoun, M. A.; Al-Tarawneh, S. *J. Lumin.* **2011**, 131,8, 1795-1801.

[7] http://www.rp-photonics.com/erbium_doped_fiber_amplifiers.html

[8] Becker, P. C.; Olsson, N. A.; Simpson, J. R. *Erbium Doped Fiber Amplifiers Fundamentals and Technology*; Academic Press: San Diego, CA, **1999**.

[9] Park, S. H.; Lee, D. C.; Heo, J.; Kim, H. S. *J. Am. Ceram. Soc.* ,**2000**, 83,5,1284-1286.

[10] Peng, B.; Fan, Z.; Qiu, X.; Jiang, L.; Tang, G. H.; Ford, H. D.; Huang, W. *Adv. Mater. ,* **2005**, 17,7, 857-859.

[11] Kumta, P. N.; Risbud, S. H. *J. Mater. Sci.* **1994**, 29, 1135.

[12] Yang, Y.; Alexandratos, S. D. *Industrial & Engineering Chemistry Research* , **2009**, 48,13, 6173-6187.

[13] Moynihan, S.; Van Deun, R.; Binnemans, K.; Redmond, G. *Optical Materials*, **2007**, 29,12, 1821-1830.

[14] Ma, X.; Li, X.; Cha, Y. E.; Jin, L.-P. *Crystal Growth & Design* ,**2012**, 12,11, 5227-5232.

[15] Kumar, G. A.; Riman, R. E.; Chen, S.; Smith, D.; Ballato, J.; Banerjee, S.; Kornienko, A.; Brennan, J. G. *Appl. Phys. Lett.* **2006**, 88, 91902.

[16] Banerjee, S.; Kumar, G .A.; Emge,T. J.; Riman,R. E.; Brennan, J. G. *Chem. Mater.* **2008**, 20, 4367

[17] (a) Lee, J. S.; Emge, T. J.; Brennan,J. G. *Inorg. Chem.* **1997**, 36, 5064. (b) Berardini, M.; Emge, T.; Brennan, J. *Inorg. Chem.* **1995**, 34, 5327. (c) Berardini, M.; Emge, T.; Brennan, J. *J. Am. Chem. Soc.* **1994**, 116, 6941. (d) Banerjee, S.; Sheckelton, J.; Emge, T. J.; Brennan, J. G. *Inorg. Chem.* **2010**, 49, 1728. (e) Brewer, M.; Lee, J.; Brennan, J. G. *Inorg. Chem.,* **1995**, 34, 5919.

[18] a)Melman, J. H.; Emge, T. J.; Brennan, J. G. *Inorg. Chem.*,**1999**, 38,9, 2117. b)Freedman, D.; Emge, T. J.; Brennan, J. G. *Inorg. Chem.,* **2002**, 41,3, 492. c)Freedman, D.; Sayan, S.; Emge, T. J.; Croft, M.; Brennan, J. G. *J. Am Chem. Soc.,* **1999**, 121,50, 11713.

[19] Schneck, C.; Hoess, P.; Schleid, T. *Acta Crystallogr., Sect. E* **2009**, E65, 20.

[20] Freedman, D.; Emge,T. J.; Brennan, J. G. *Inorg. Chem.,* **1999**, 38,20,, 4400.

[21] Berardini, M.; Emge, T. J.; Brennan, J. G. *Inorg. Chem.,***1995**, 34,21, 5327.

[22] Lee, J.; Freedman, D.; Melman, J. H.; Brewer, M.; Sun, L.; Emge, T. J.; Long, F. H.; Brennan, J. G. *Inorg. Chem.,* **1998**, 37,10, 2512.

[23] (a) Oczko, G. *J. Alloys Comp.,* **2000**, 300, 414. (b) Lis,S. *J. Alloys Comp*. **2000**, 300, 88. (c) Gubina, K. E.; Shatrava, J. A.; Ovchynnikov, V. A.; Amirkhnov,V. M. *Polyhedron* **2000**, 19, 2203. (d) Legendz-iewicz, J.; Oczko, G.; Wiglusz, R.; Amirkhanov, V. *J. Alloys Comp.* **2001**, 323, 792.

[24] Prokofiev, A. V.; Shelykh, A. I.; Golubkov, A. V.; Smirnov, I. A. *J. Alloys Compd* **1995**, 219, 172.

[25] a)Ansari, A. A.; Irfanullah, M.; Iftikhar, K. *Spectrochimica Acta, Part A: Molecular and Biomolecular Spectroscopy*., **2007**, 67A(5), 1178-1188.b)Iftikhar, K. *Inorg. Chim. Acta* ,**1987**, 129, 2, 261.

[26] Ofelt, G. S. J. *Chem. Phys*., **1962**, 37, 511.

[27] Judd, B. R. *Phys. Rev B.,* **1962**, 127, 750.

[28] Carnall, W. T.; Hessler, J. P.; Wagner, F. *J. Phys. Chem*. **1978**, 82, 2152.

[29] Wang, X.; Zhuang, J.; Peng, Q.; Li, Y. *Inorg. Chem*. **2006**, 45, 6661.

[30] Tan, M.C .; Kumar, G. A.; Riman, R. E.; Brik, M. G.; Hommerich, U. *J. Appl. Phys.* **2009**,106, 063118.

[31] (a) Schweizer, T. Ph.D. Thesis, Universitat Hamburg, **1998.** (b) *Optical Fiber Amplifiers Materials, Devices, and Applications;* Sudo,S.,Ed; Artech House Inc.: Norwood, MA, **1997**.

[32] Kumar, G. A.; Kornienko, A.; Banerjee, S.; Riman, R. E.; Emge,T. J.; Brennan, J. G. *Chem. Mater.* **2005**, 17, 5130.

[33] Banerjee, S.; Huebner, L.; Romanelli, M. D.; Kumar, G. A.; Riman, R. E.; Emge,T. J.; Brennan, J. G. *J. Am. Chem. Soc.* **2005**, 127, 15900.

[34] Norton, K.; Kumar, G. A.; Dilks, J. L.; Emge,T. J.; Riman, R. E.; Brik, M. G.; Brennan, J. G. *Inorg. Chem.* **2009**, 48, 3573.

[35] Romanelli, M. D.; Kumar, G. A.; Riman, R. E.; Emge, T. J.; Brennan, J. G. *Angew. Chem.* **2008**, 47, 6049.

[36] Banerjee, S.; Kumar, G. A.; Riman, R.; Emge,T. J.; Brennan, J. *J. Am. Chem. Soc.* **2007**, 129, 5926.

[37] Dıaz Torres,L. A.; Barbosa-Garcia,O.; Meneses-Nava,M. A.; Struck,C.W.; Di Bartolo,B. *In Advances in Energy Transfer Processes*; Di Bartolo, B., Chen, X., Eds. World Scientific Publishing Co.: Singapore, **2000**; 523-552.

CHAPTER 3. Heterometallic Octahedral Europium Chalcogenolates

3.1 Introduction

Since europium 2^+ and 3^+ ions possess localized valence orbital configurations ($4f^7$ and $4f^6$ respectively) with unpaired electrons it should come as no surprise that europium chalcogenide systems exhibit magnetic properties. Magnetic europium monochalcogenide materials (EuE), have been an active area of research since the 1960's.[1]The well documented variances in the magnetic ordering of these species[2,3] (O and S = ferromagnetic; Se= metamagnetic ; Te=antiferromagnetic) led to their classification as magnetic ordering semiconductors[4]. Their potential to control conduction through direction of quantum spin states and electronic carriers (p- and n- type)[5] is an alluring target. As a result, current EuE materials research focuses on applications. From composite and phosphor lasers[6] to spintronics development (electronic devices using spin related phenomena)[7] the potential for europium chalcogenide materials is vast.

Despite their potential, europium chalcogenide systems face fundamental and application challenges. First, In binary europium chalcogenides (EuO T_c= 66.8K, EuS T_c=16.6K, EuSe T_n= 4.6K, and EuTe T_n= 9.6K)[8] T_c and T_n temperatures are well below the desired threshold for magneto-electronic applications. Spintronics seeks to take advantage of electrical resistance suppression induced by the application of a large magnetic fields.[9] These effects have been heightened through the use of multi-junction arrays consisting of alternating magnetic and nonmagnetic layers (Fe-Cr, figure 3.1).[10]

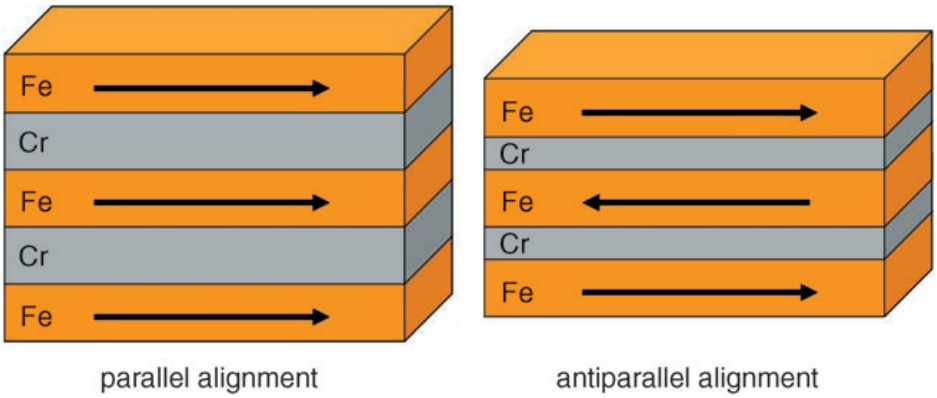

Figure 3.1. Fe-Cr Multilayer System.

However, even greater magneto resistance effects have been observed with changes in magnetic field direction (Current in Plane, CIP vs Current Perpendicular to the Plane, CPP) and field strength and necessitating modifications in device configurations (figure 3.2).[11]

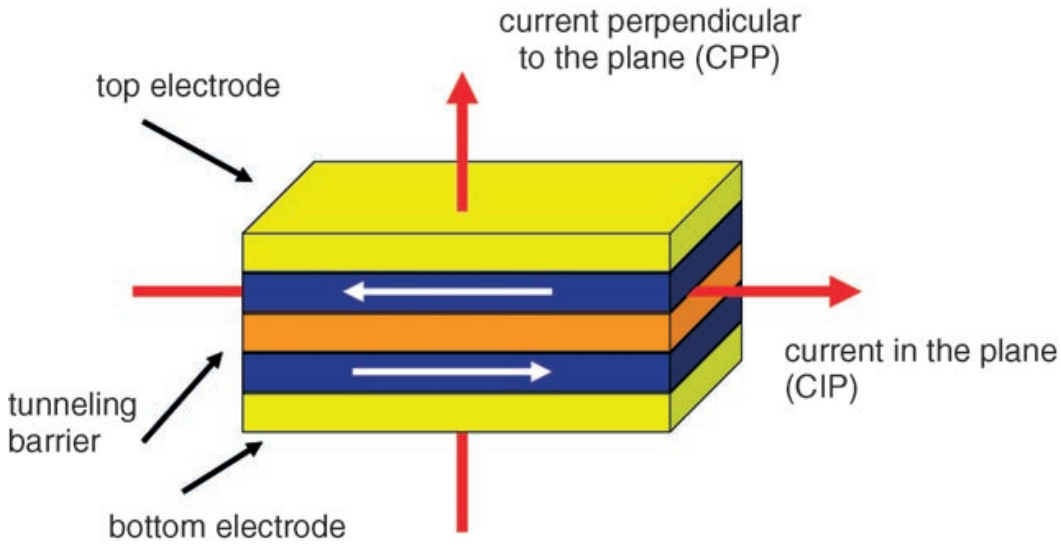

Figure 3.2. Fe-Cr Multilayer Configuration for CIP and CPP Magneto Resistant Platforms.

Maintaining the magnetic spins across metal/insulator and metal/magnet junctions requires unique materials with tunneling and magnetic spin filtering

capabilities. The internal magnetic fields generated by Eu^{2+} in europium monochalcogenides induce a splitting (Zeeman Effect)[12] of the generated spin sub bands.[13] The combination of ferromagnetic ordering and strong Zeeman effects make EuO and EuS viable candidates as field dependent spin filters in multi junction devices.[14] Unfortunately low Curie temperatures preclude their full implementation.

Based upon a fundamental understanding of magnetic ordering principles numerous attempts sought to improve EuE critical temperatures. The T_c and T_n [15] define the climate under which the magnetic moment (magnetic susceptibility, χ is the more commonly used metric) for magnetically ordered (ferromagnetic and antiferromagnetic respectively) materials become paramagnetic. The relation between temperature and χ are expressed by the Curie-Weiss law (equation 3.1). C represents the Curie constant while T and T_c represent the active temperature and the Curie temperature respectively. C is further defined in equation 3.2.

$$\chi = \frac{C}{T - T_c}$$

Equation 3.1. Curie-Weiss Law.

$$C = \frac{\mu_o \mu_b^2}{3k_b} N g^2 J(J+1)$$

$$\mu_{eff} = \sqrt{\frac{3k_b C}{(N/V)\mu_B^2}} = 2.828\sqrt{C}$$

Equation 3.2. Curie Constant and Effective Magnetic Equations.

In the above, N is the number of magnetic atoms per unit of volume, g is the Landé g-factor, μ_o is the permeability constant, μ_b is the bohr mangeton, J is the angular momentum and k_b is the Boltzmann's constant. Since, the magnitude of the Curie constant is proportional the number of magnetic atoms/molecules per unit of volume[13] varying the number of magnetic species was expected to effect the Curie and Neel temperatures as well. Gadolinium was successfully doped in EuO thin films and EuS nanoparticles by Ott[16]and Kar[17] respectively. The EuO materials displayed an increased T_c values from 67K to 170K in 4%Gd:EuO, while a decrease in T_c from 16.6K to 7.82K for 2%Gd:EuS was reported. Unfortunately, improved T_c and T_n values for nano and solid state materials have been few and far between. Oxide dopants [18] as well as systems with calcium[19] lead[20] and strontium[21] species have all been investigated. These materials offered profound insight into the relationships surrounding magnetic susceptibility and particle size[22] as well as the influence of phase and lattice parameters. Nevertheless, they did little to raise critical temperatures to within desired ranges, while maintaining the magneto-resistant properties desired.

The second issue confronting EuE is the lack of single crystalline divalent and trivalent models. Despite the advantages made through solid state[23] and nanofabrication [24] a clear understanding of the structural and valence influences on magnetic properties has eluded EuE researchers. To date nano and solid state EuE syntheses rely on colloidal, and thermolytic processes.[25] These products regularly display polycrystalline morphologies and colloid structures, unsuitable for determining more precise crystallographic information. This is particularly confounding since Mossbauer studies[26] of both material types reveal the presence of Eu^{2+} and Eu^{3+} ions in europium monochalcogenides[27]. Eu^{2+} and Eu^{3+} exhibit significant differences in ionic radii (Eu^{2+}: 1.31-1.49 Å and Eu^{3+}: 1.08-1.26 Å) according to shannon[28] and can lead to strained lattices[29] and interrupted/altered magnetic coupling interactions. Simultaneously, the $4f^7$ and $4f^6$ electronic configurations necessitate distinct total angular momenta (J-states). Equations 3.1 and 3.2 shows the interrelationship between J-states, the curie constant and magnetic susceptibilities. Therefore, the potential information gleened from individual valence vs magnetic studies could be invaluable in determining the coupling mechanism underlying the variances in EuE magnetic ordering. As a result, crystalline EuE coordinated models of a single valence provide a platform for the investigation of structural and valence influences on EuE magnetic ordering.

The introduction of sodium azide into a solution based EuE environments offers several opportunities. First, studies of the effect of sodium on the magnetic properties of EuE products is noticeably absent from the literature and could

provide additional insight into the optimization of T_c and T_n through doping. Second, the monovalent ions of the alkali metals regularly stabilize solid state and solution based rare earth single crystalline phases. The range of materials produced (clusters to ternary solids) makes the possibility of isolating species with unique Na-E-Eu architectures a viable one. Third, EuE products' notorious insolubility, in most solvents, could be overcome by the presence of additional cations as well soluble E anion sources such as chalcogenolates. This combination has already been shown to provide greater solubility to intermediates and promote single crystal formation through a slower nucleation process in the previous two chapters. Finally, the azide anion while an emissive quencher has been shown to serve as a non competitive leaving group in lanthanide chemistry when directed.

3.2 $Eu(EPh)_4(Na)_2 \cdot 2DME$: Synthesis, Structure, and Discussion

While investigating the potential of sodium azide in the formation of solution based europium chalcogenide clusters the title complexes were synthesized. The combination of 2 equivalents of $Eu(EPh)_2$, and 4 equivalents of sodium azide in DME (Scheme 3.1) resulted in the isolation of the $(DME)_2Eu(EPh)_4(Na)_2$ complexes.

$$2Eu + 2(EPh)_2 + Hg \xrightarrow[4NaN_3]{45ml\ DME} (DME)_2Eu(EPh)_4(Na)_2$$

$$E = S, Se$$

Scheme 3.1. Synthesis of $(DME)_2Eu(EPh)_4(Na)_2$.

The isostructural $(DME)_2Eu(SPh)_4(Na)_2$ and $(DME)_2Eu(SePh)_4(Na)_2$ complexes were produced in good yield (73% and 61% respectively), with r-factors of 7% and 4% for each. A tellurium analogue of the above system was attempted but could not be isolated.

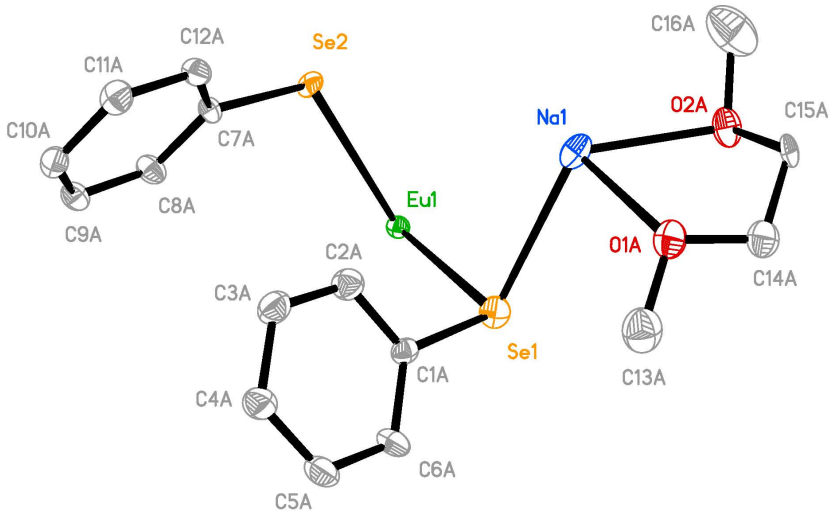

Figure 3.1 ORTEP Structure of $(DME)_2Eu(SePh)_4(Na)_2$ Motif.

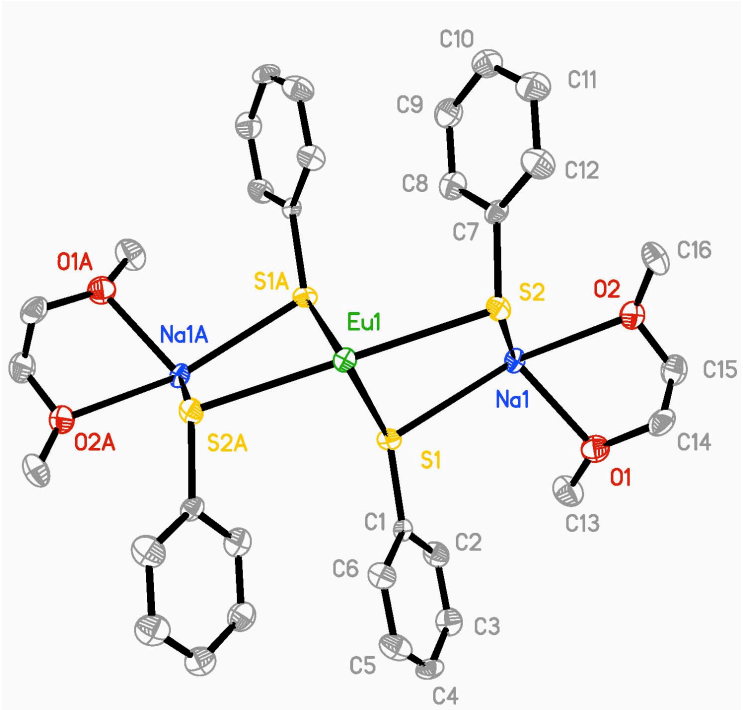

Figure 3.2. ORTEP of $(DME)_2Eu(SPh)_4(Na)_2$ Unit Cell Structure.

Empirical Formula	$C_{32}H_{40}Na_2EuO_4S_4$	$C_{32}H_{40}Na_2EuO_4Se_4$
Formula Weight	814.82	1002.42
Temperature (K)	100	100
Wavelength (Å)	0.71073	0.710703
Crystal System	monoclinic	monoclinic
Space Group	P2	P2
a (Å)	13.4272(14)	13.5182(6)
b (Å)	5.2238(5)	5.3571(2)
c (Å)	14.2150(15)	14.3881(6)
β (deg)	117.35(3)	117.277(1)
volume ($Å^3$)	885.60(16)	926.10(7)
Density (calculated) (Mg/m^3)	1.528	1.797
Z	1	1
Final R indices [I>2sigma(I)]	R1=.0746 WR2= .1733	R1=.0395 WR2= .0959

Table 3.1. Crystal Data and Structure Refinement for $(DME)_2Eu(SPh)_4(Na)_2$ and $(DME)_2Eu(SePh)_4(Na)_2$

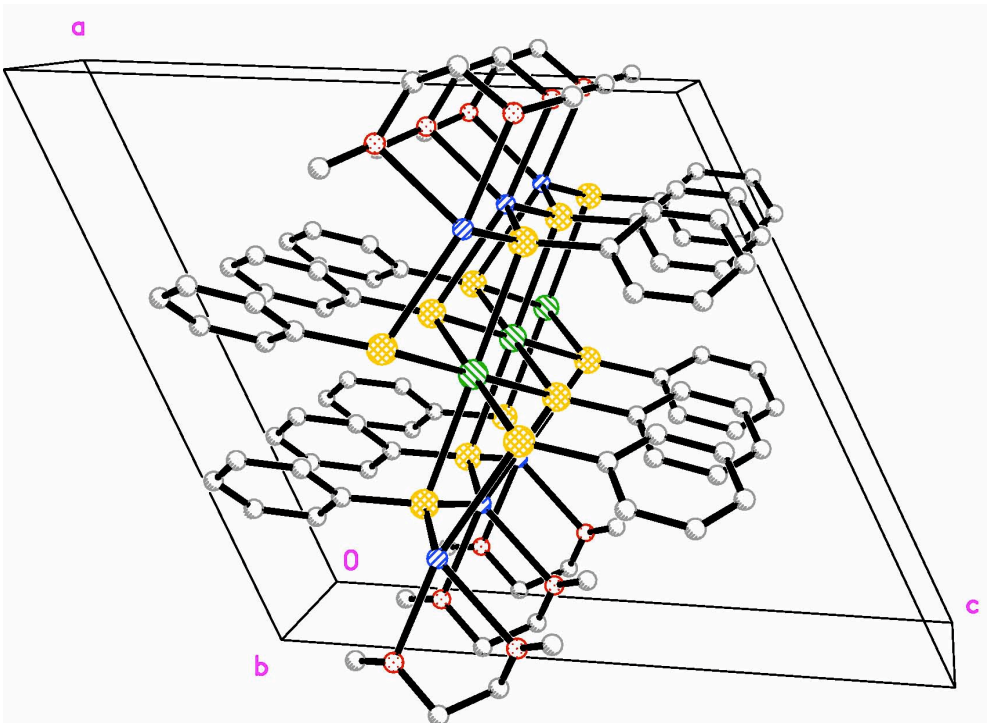

Figure 3.3. ORTEP of $(DME)_2Eu(SePh)_4(Na)_2$ Trimer Sideview.

$(DME)_2Eu(EPh)_4(Na)_2$ (E= S, Se) consists of a single core europium ion on a crystallographic 2-fold axis, coordinated to 2 pairs of μ_3-chalcogenolates. The four chalcogenolates form a distorted planar confirmation around the central europium, while the phenyl rings are oriented trans to the plane (figure 3.2). The pairs are coordinated to two 5 coordinate (DME) Na(EPh) end caps, with two μ_3-EPh groups bound to europium atoms on adjacent complexes. As a result, each europium exists in a distorted octahedral chalcogenide environment (figure 3.3-3.4). A comparison of bond distances for the two systems (table 3.2) displays bond ranges of 2.97-3.10 for $(DME)_2Eu(SPh)_4(Na)_2$ and 3.08-3.17 for $(DME)_2Eu(SePh)_4(Na)_2$. These bond distributions were consistent with previously published EuEPh systems.[30]

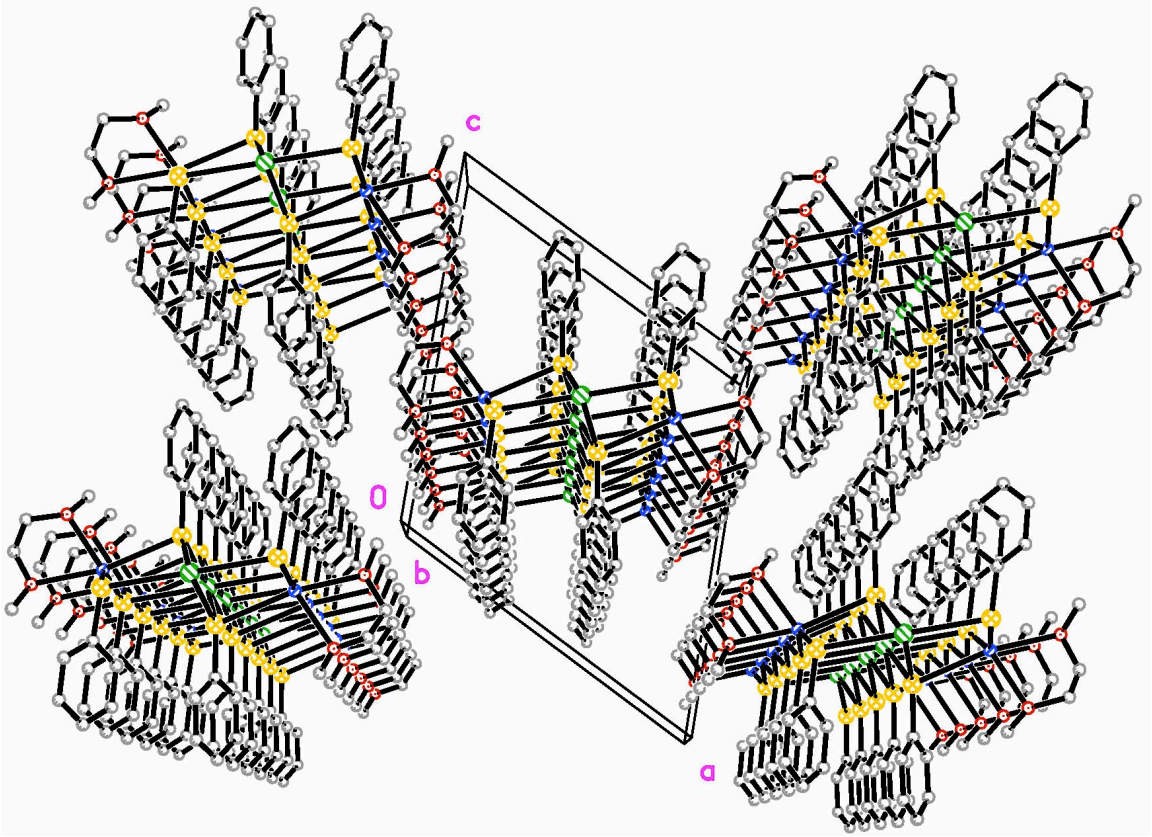

Figure 3.4. ORTEP of $(DME)_2Eu(SPh)_4(Na)_2$ Extended Lattice Packing.

Bonds: $Eu(SPh)_4(Na)_2$•2DME	Bond Distance (Å)	Bonds: $Eu(SePh)_4(Na)_2$•2DME	Bond Distance (Å)
Eu(1)-S(2)	2.974(3)	Eu(1)-Se(1)1	3.0809(4)
Eu(1)-S(2)1	2.974(3)	Eu(1)-Se(1)	3.0809(4)
Eu(1)-S(1)1	3.064(10)	Eu(1)-Se(2)1	3.1597(14)
Eu(1)-S(1)	3.064(10)	Eu(1)-Se(2)	3.1597(14)
Eu(1)-S(1)2	3.100(9)	Eu(1)-Se(2)2	3.1747(15)
Eu(1)-S(1)3	3.100(10)	Eu(1)-Se(2)3	3.1747(15)
Eu(1)4-S(1)	3.100(9)	Eu(1)4-Se(2)	3.1747(15)
Na(1)-O(1)	2.397(12)	Na(1)-O(2A)	2.368(6)
Na(1)-O(2)	2.460(10)	Na(1)-O(1A)	2.437(6)
Na(1)-S(2)4	2.748(17)	Na(1)-Se(1)	2.876(8)
Na(1)-S(2)	2.800(18)	Na(1)-Se(2)1	3.0374(16)
Na(1)-S(1)	2.927(5)	Na(1)2-Se(1)	2.838(7)
Na(1)3-S(2)	2.748(18)	Na(1)1-Se(2)	3.0375(16)

Table 3.2. Select Bond Distances for $(DME)_2Eu(SPh)_4(Na)_2$ and $(DME)_2Eu(SePh)_4(Na)_2$.

Bonds: $Eu(SPh)_4(Na)_2$·2DME	Angle (deg)	Bonds: $Eu(SePh)_4(Na)_2$·2DME	Angle (deg)
S(2)-Eu(1)-S(2)1	179.8(4)	Se(1)1-Eu(1)-Se(1)	179.94(8)
S(2)-Eu(1)-S(1)1	96.5(2)	Se(1)1-Eu(1)-Se(2)1	96.30(4)
S(2)1-Eu(1)-S(1)1	83.7(2)	Se(1)-Eu(1)-Se(2)1	83.76(4)
S(2)-Eu(1)-S(1)	83.7(2)	Se(1)1-Eu(1)-Se(2)	83.76(4)
S(2)1-Eu(1)-S(1)	96.48(19)	Se(1)-Eu(1)-Se(2)	96.30(4)
S(1)1-Eu(1)-S(1)	64.6(2)	Se(2)1-Eu(1)-Se(2)	64.67(4)
S(2)-Eu(1)-S(1)2	96.26(19)	Se(1)1-Eu(1)-Se(2)2	83.73(4)
S(2)1-Eu(1)-S(1)2	83.6(2)	Se(1)-Eu(1)-Se(2)2	96.21(4)
S(1)1-Eu(1)-S(1)2	115.87(9)	Se(2)1-Eu(1)-Se(2)2	179.83(3)
S(1)-Eu(1)-S(1)2	179.6(2)	Se(2)-Eu(1)-Se(2)2	115.497(10)
S(2)-Eu(1)-S(1)3	83.6(2)	Se(1)1-Eu(1)-Se(2)3	96.21(4)
S(2)1-Eu(1)-S(1)3	96.26(19)	Se(1)-Eu(1)-Se(2)3	83.73(4)
S(1)1-Eu(1)-S(1)3	179.6(2)	Se(2)1-Eu(1)-Se(2)3	115.497(10)
S(1)-Eu(1)-S(1)3	115.87(9)	Se(2)-Eu(1)-Se(2)3	179.83(3)
S(1)2-Eu(1)-S(1)3	63.7(2)	Se(2)2-Eu(1)-Se(2)3	64.33(3)

Table 3.3. Coordination Angles for the Central Eu^{2+} in $(DME)_2Eu(SPh)_4(Na)_2$ and $(DME)_2Eu(SePh)_4(Na)_2$

While nearly analogous to previous work in bridging motifs and extended structures, the presence of the rarely seen solvent free octahedral europium coordination environment in $(DME)_2Eu(EPh)_4(Na)_2$ products supports the idea of an additional structural influence in the reaction. The ability to modify the bridging modes and nuclearity of lanthanide chalcogenolate complexes through ionic radii and chalcogenolate selection has been throughly explored and characterized.[31]

Beradini's $[(THF)_3Eu(\mu\text{-}SePh)_2]_\infty$ and $[\{(py)_2Eu(\mu\text{-}SePh)_2\}_4]_\infty$ (figure 3.4) Brewer's $[(py)_3Eu(\mu_2\text{-}SPh)_2(\mu_3\text{-}SPh)M(SPh)]_2 \cdot 2py$ (figure 3.6) and Khasnis' $[(THF)_3Eu(TeC_6H_5)_2NaTePh]_\infty$ and $[(THF)_2Eu^{II}(TeC_6H_5)_2]_\infty$(figure 3.7 and figure 3.8)[32] complexes highlight the structural preferences of molecular europium species' (specific chalcogenolate bridging modes (μ_2 and μ_3) and discrete coordination numbers (6,7,8) with non directional geometries). A particularly interesting observation is the absence of neutral donor free octahedral coordination in any of the above structures including $[(THF)_3Eu(TeC_6H_5)_2NaTePh]_\infty$ where sodium was present. The presence of μ_3 chalcogenolate bridges, and a 1-D polymeric configuration in the $(DME)_2Eu(EPh)_4(Na)_2$ structure highlights similarities between the systems. Conversely, the solvent-free octahedral coordination sphere suggests the presence of additional influences on structure determination since the presence of Na and chalcogenolate alone did not yield a similar motifs.

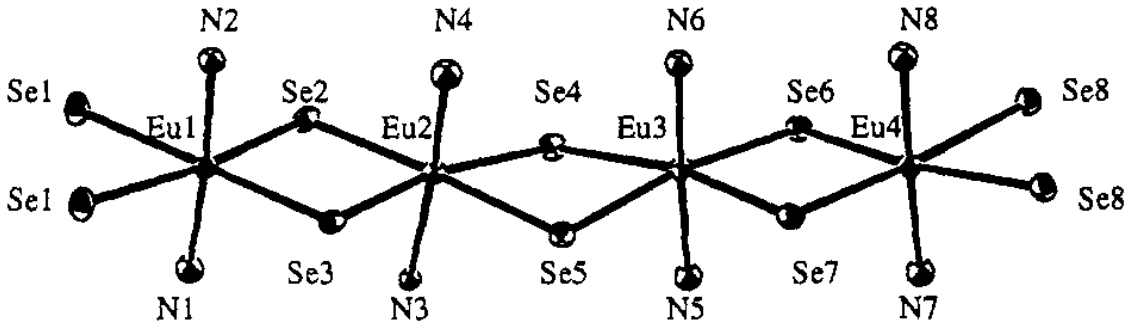

Figure 3.5. Extended Coordination Sphere of $[\{(py)_2Eu(\mu\text{-}SePh)_2\}_4]_\infty$.

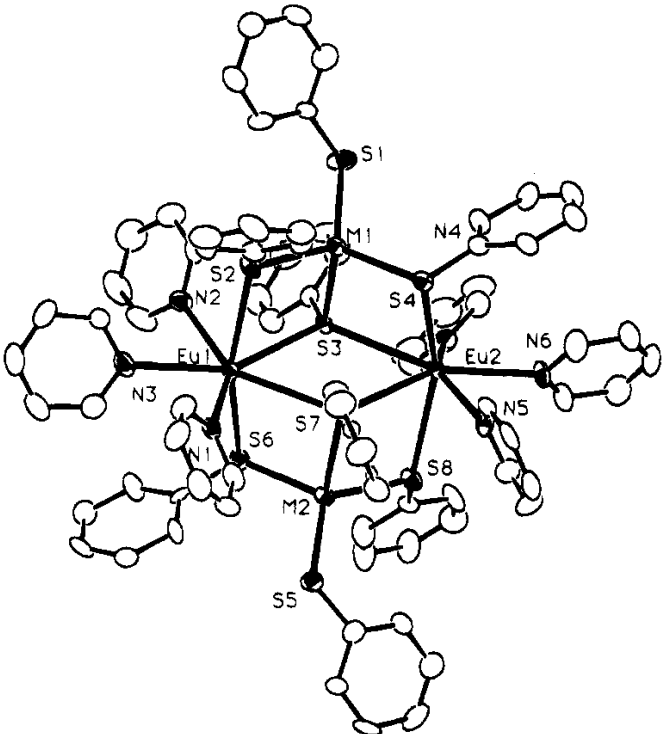

Figure 3.6. Molecular Structure of $[(py)_3Eu(\mu_2\text{-}SPh)_2(\mu_3\text{-}SPh)M(SPh)]_2 \cdot 2py$ (M= Cd, Hg).

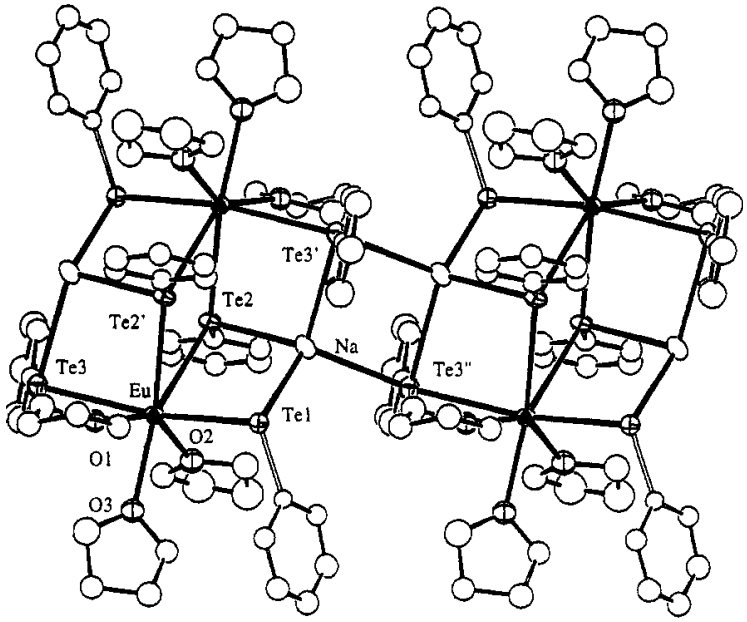

Figure 3.7. Molecular Structure of $[(THF)_3Eu(TePh)_2NaTePh]_\infty$.

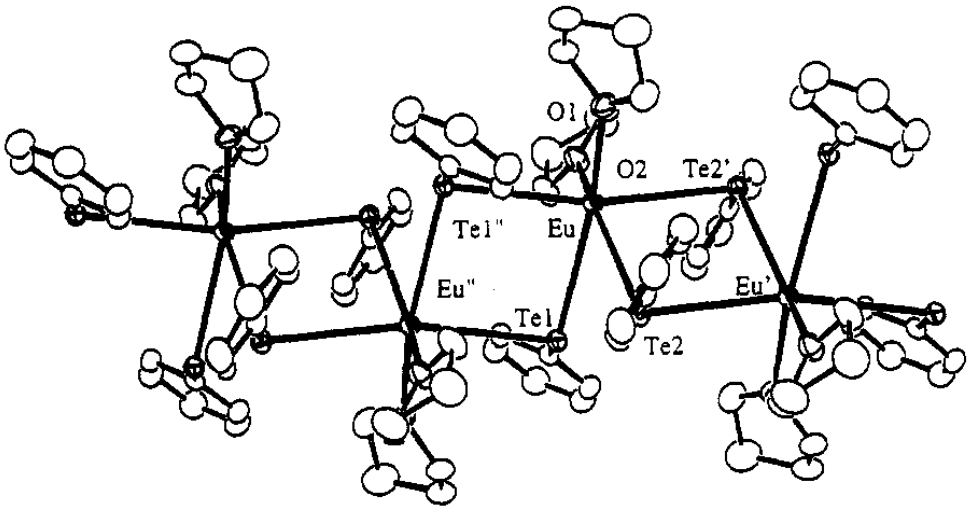

Figure 3.8. Molecular Structure of $[(THF)_2Eu^{II}(TeC_6H_5)_2]_\infty$

The presence of sodium and azide ions in a chalcogenolate deficient environment and careful solvent selection provided an ideal environment for the octahedral europium chalcogenolate coordination observed. First, the reaction equilibrium favored a mixed Eu/Na product because the anion/cation molar ratio was stoichiometrically deficient of enough EPh ligands to favor the production of $Eu(EPh)_2$ and $Na_2(EPh)_2$ in solution (4 mmol of Eu and 4 mmol of Na vs 8 mmol of EPh). As a result mixed Eu/Na EPh molecules were the more viable outcome since azides can be readily replaced on sodium by chalcogenolate ligands. Next, the inability of azide anions to stabilize the Eu^{3+} or Eu^{2+} oxidation states also precluded the formation of alternate products. This was supported by the inability to form any europium (II) azide complexes during the course of this entire body of research and the absence of any $Eu^{II/III}(N_3)_x$ in the literature without the presence of hard donor anion coordinations. An example of the latter , is found in the $[Na_2\{Mn^{3+}{}_3(\mu_3\text{-}O^{2-})\}_2Ln^{3+}(hmmp)_6(O_2CPh)_4(N_3)_2]OH{\cdot}0.5\ CH_3CN{\cdot}1.5H_2O$[33] species. As

one of the few europium (III) complexes made containing azide coordinations, the europium sphere is stabilized by two types of hard donor species (O_2CPh^{-1} OH^-), while the lone azide occupies a single μ_2 bridging site between Mn atoms. The use of sodium azide was also critical since direct addition of sodium metal in place of sodium azide resulted in the isolation of Na_2E and NaEPh species due to reduction of the C-E chalcogenolate bonds and the greater electronegativity of sodium ions vs europium ions. Finally, DME's bidentate coordination ability, low polarity, and absence of bulky cyclic rings (as opposed to THF and pyridine) provided an excellent surface stabilizer for the sodium end caps of the system while not imposing any steric strain. Overall, the unique coordination environment of $(DME)_2Eu(EPh)_4(Na)_2$ is the result of a directed synergy between sodium azide, DME and the well established lanthanide chalcogenolate architecture.

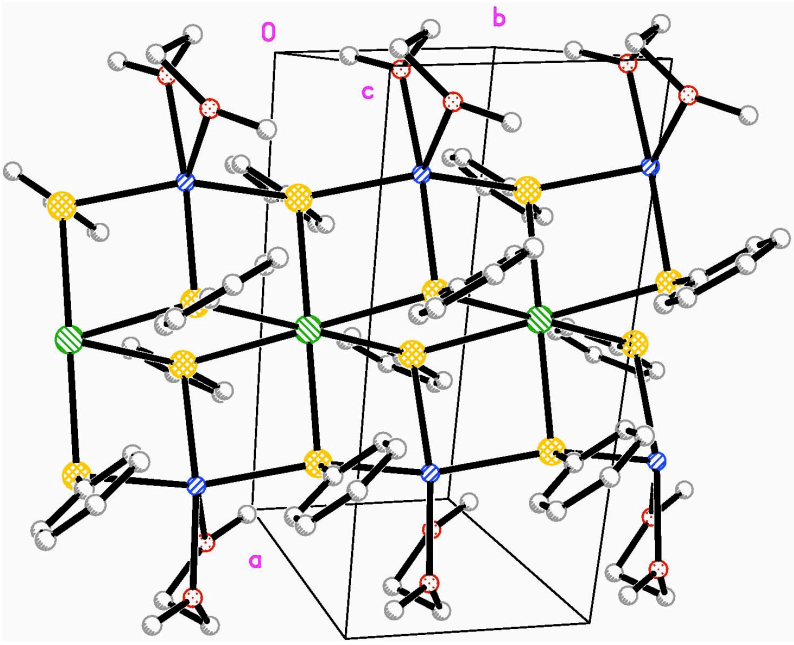

Figure 3.9. ORTEP of $Eu(SPh)_4(Na)_2$•2DME Trimer.

A comparison of $(DME)_2Eu(EPh)_4(Na)_2$'s extended structure with solid state EuE and MEuE (M= Na,K),provided confirmation that the solution based complex coordination and bond lengths were consistent with similar solid state products. The Eu-S bond ranges for $(DME)_2Eu(SPh)_4(Na)_2$(2.97-3.10 Å) and $Na_{1.515}EuGeS_4$[34] (2.955-3.082 Å) showed significant overlap. A similar congruency was observed for the Eu-Se bond distances found in $(DME)_2Eu(SePh)_4(Na)_2$ (3.08-3.17 Å) $EuSe_2$ [35] (3.175 Å) and to a lesser degree in the multivalent $K_2EuGeSe_5$[36] (3.12-3.48 Å). This trend was expected given that even with variances in chalcogenide species coordinated to the metal centers (EPh^{-1}, EE^- and E^{2-}) no significant differences in bond length could be found. Second, the presence of varied coordination numbers between the chalcogenide rich solid state products and the solution based products (CN=7 for $Na_{1.515}EuGeS_4$ and $K_2EuGeSe_5$; CN=9 for $EuSe_2$ and CN=6 for $(DME)_2Eu(EPh)_4(Na)_2$) is an explainable feature of EuE products. According to Shannon the ionic radii associated with Eu^{2+} with chalcogenide coordinations of 6,7,8,& 9 differ by ~0.04 Å each. Variations in CN are reasonable provided their are no significantly longer or shorter bond lengths (indicates a significant ionic radii difference), which would have been a potential indicator of mixed valence as in $K_2EuGeSe_5$. In summary, the observed consistency of $(DME)_2Eu(EPh)_4(Na)_2$ with similar solid state species supports the validity of using the complex as model for examining the structural/property relationships for EuE systems.

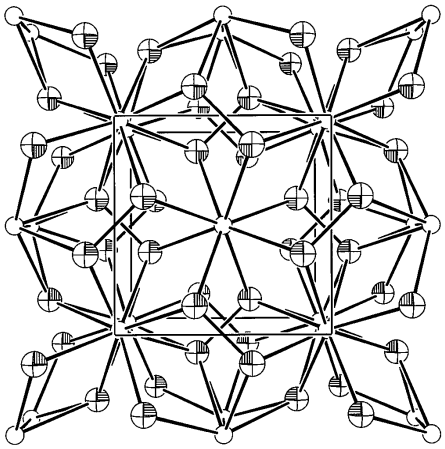

Figure 3.10. $EuSe_2$ Viewed rom the C-Axis with 90% Ellipsoids.[34]

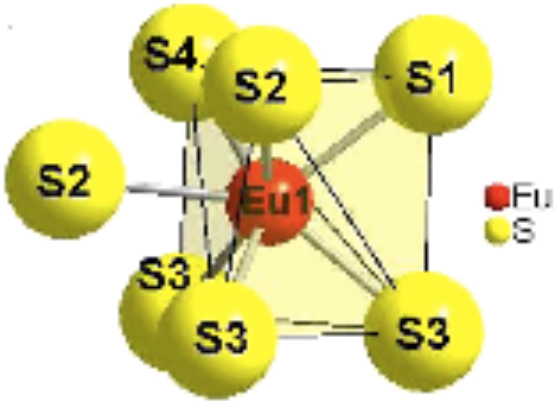

Figure 3.11. $Na_{1.515}EuGeS_4$ Europium Coordination Geometry. [35]

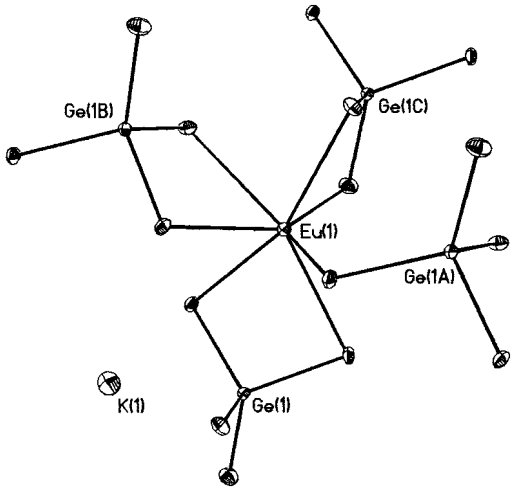

Figure 3.12. Europium Coordination Environment in $K_2EuGeSe_5$. [36]

3.3 Magnetic Susceptibility Studies

In an effort to investigate the magnetic properties of Eu-E containing systems, low temperature magnetization studies were carried out. Crystal samples of $(DME)_2Eu(EPh)_4(Na)_2$ (E=S,Se) and the unpublished Eu^{3+} product $(py)_6Eu_2(\mu_3\text{-}S_2)_2(OC_6F_5)_2$, (Figure 3.13) were studied from 0 to 200K within a 1000 Oe field under zero field cooling conditions (ZFC). The magnetic moment vs temperature plots revealed paramagnetic magnetization curves with little to no distinct features for the $(DME)_2Eu(SePh)_4(Na)_2$ (figure 3.14). $(DME)_2Eu(SPh)_4(Na)_2$ (figure 3.15) displayed a series of small interactions from 0-20K, and 60-68K, while a clear magnetic transition for $(py)_6Eu_2(\mu_3\text{-}S_2)_2(OC_6F_5)_2$ (figure 3.16) was observed from 0-20K.

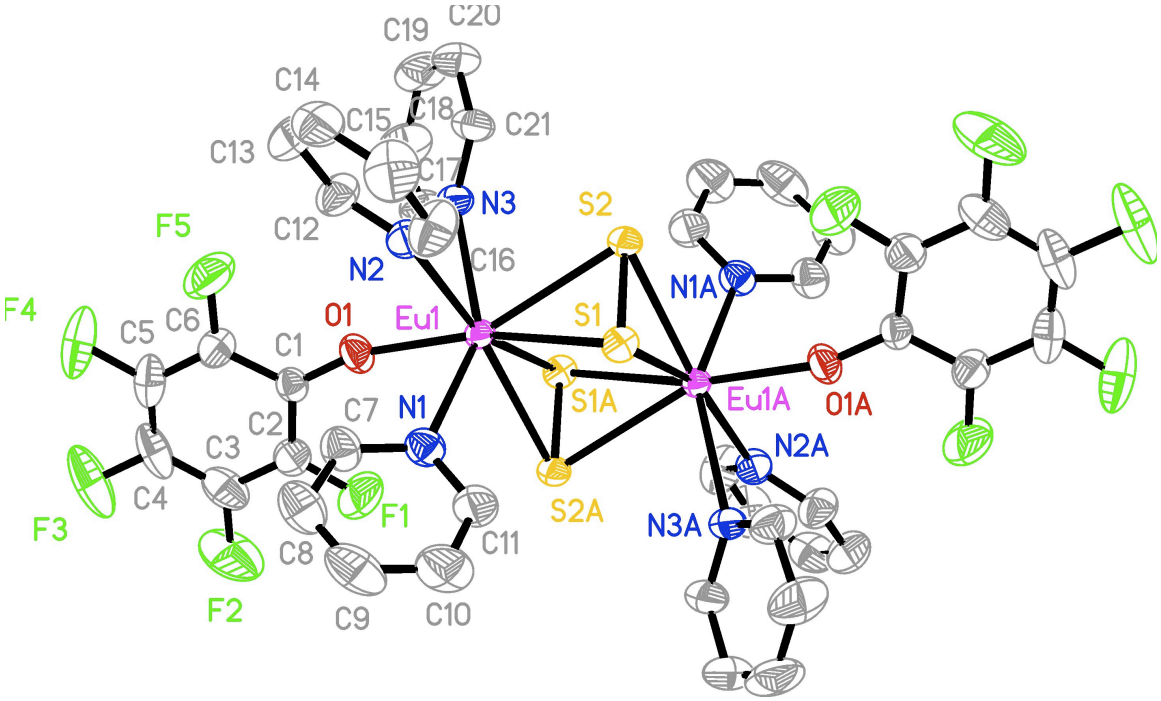

Figure 3.13. $(py)_6Eu_2(\mu_4\text{-}S_2)_2(OC_6F_5)_2$ ORTEP Structure.

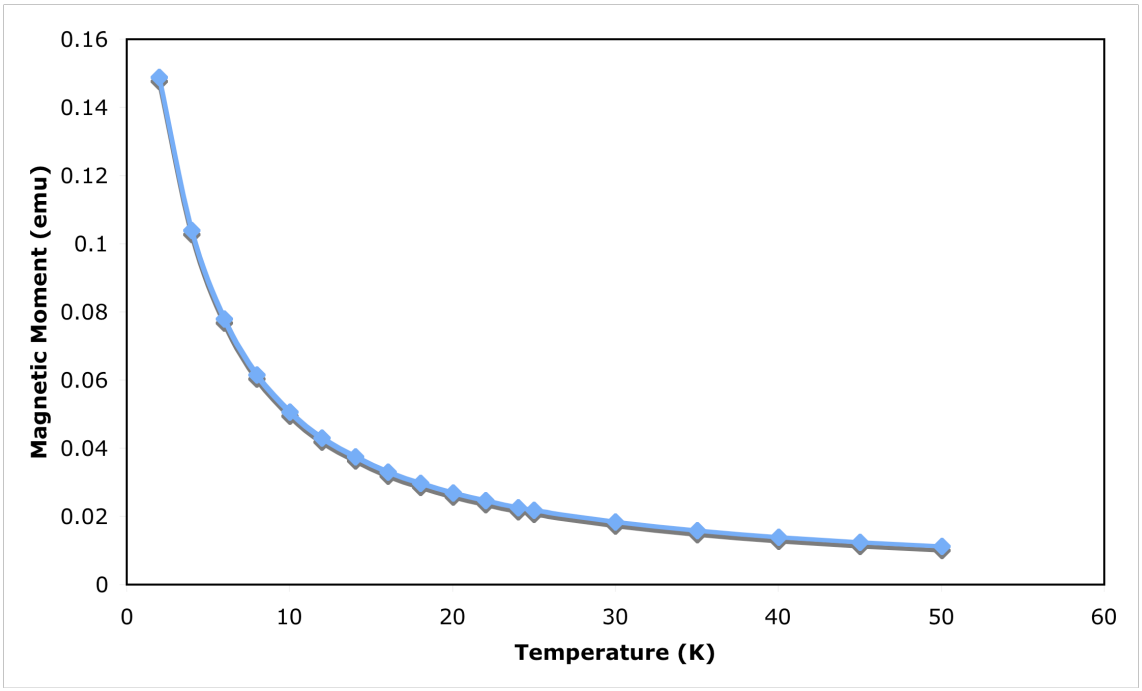

Figure 3.14. $(DME)_2Eu(SePh)_4(Na)_2$ Magnetic Moment vs Temperature Plot.

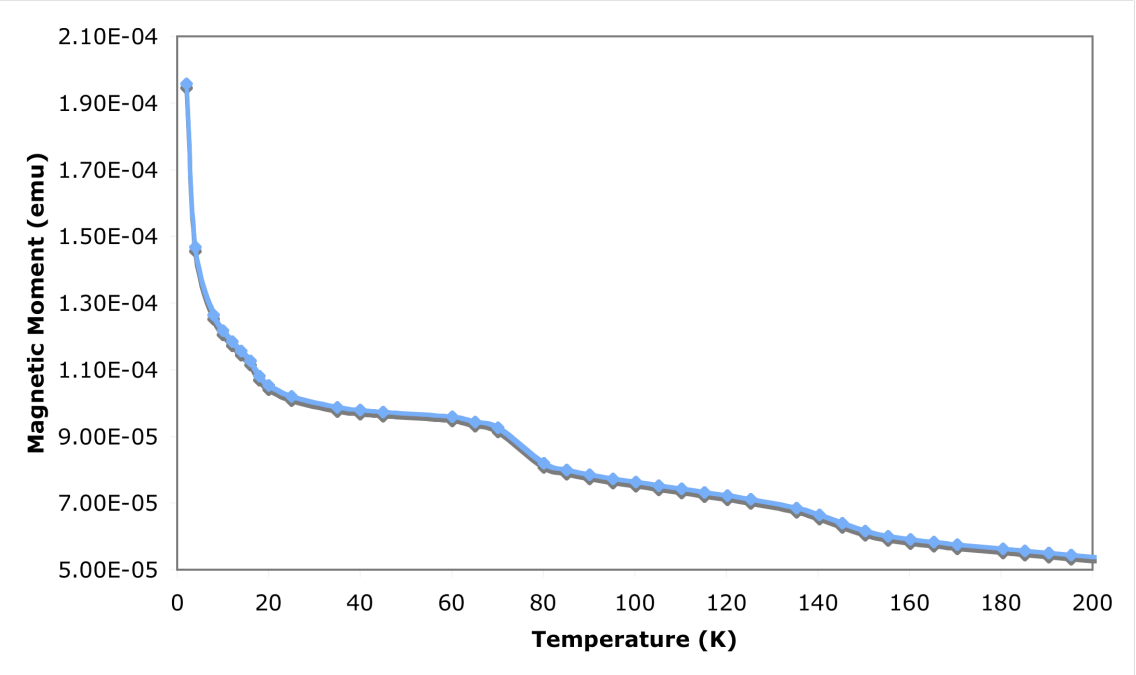

Figure 3.15. $(DME)_2Eu(SPh)_4(Na)_2$ Magnetic Moment vs Temperature Plot.

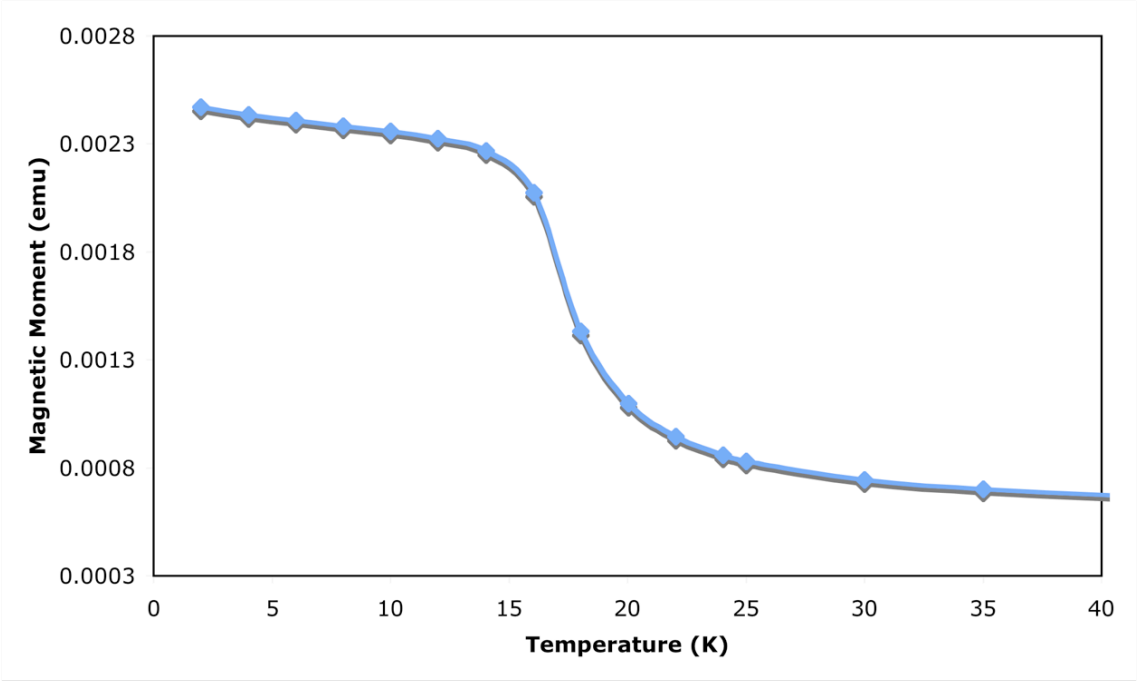

Figure 3.16. $(py)_6Eu_2(\mu_4\text{-}S_2)_2(OC_6F_5)_2$ Magnetic Moment vs Temperature Plot.

χ_m vs T plots were used to give a more refined picture of the low magnetic ordering in all three samples. χ_m values (Equation 3.4) were calculated from the raw magnetic moment data. In the χ_m determination, M= magnetization moment, H is the applied magnetic field, m is the mass of the sample and m_{mole} is the molar mass of the complex.

$$\chi_m = \frac{M}{H} \Big/ \frac{m}{m_{mole}}$$

Equation 3.4. Chi (χ_m) Determination

A ferrimagnetic ordering plot was found for $(py)_6Eu_2(\mu_4\text{-}S_2)_2(OC_6F_5)_2$. (figure 3.17). The previously described aberrations in the $(DME)_2Eu(SPh)_4(Na)_2$ (figure 3.18) magnetic moment data were absent revealing a paramagnetic curve,

similar to the one observed for $(DME)_2Eu(SePh)_4(Na)_2$ (figure 3.19). The first order derivation of χ_m with respect to T (d χ_m/dT) was plotted vs T for $(py)_6Eu_2(\mu_4\text{-}S_2)_2(OC_6F_5)_2$ to ascertain the T_c= 18.03 K (Figure 3.20).

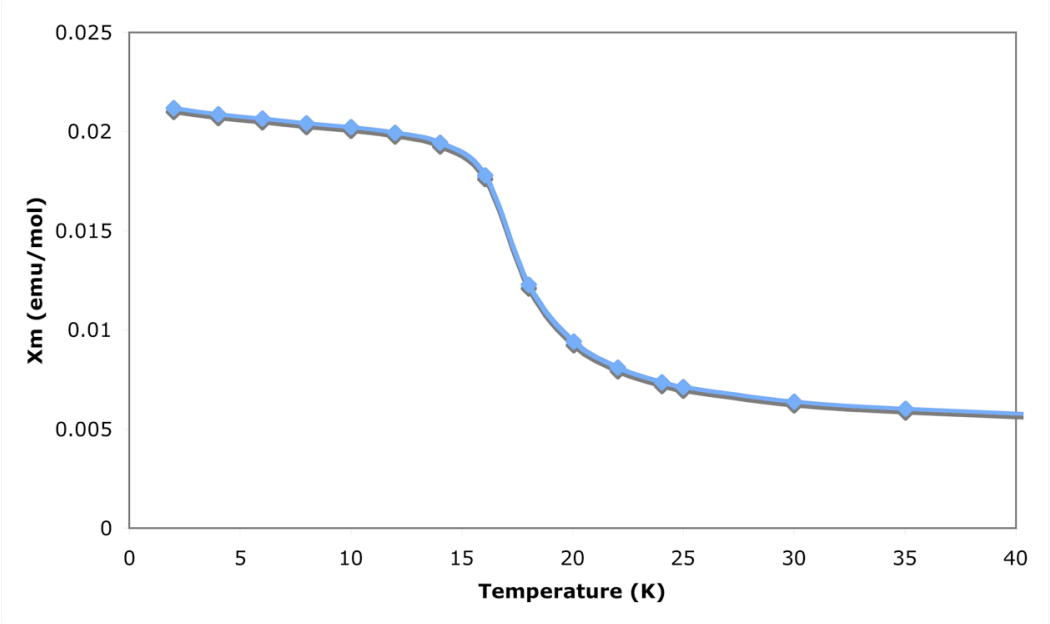

Figure 3.17. $(py)_6Eu_2(\mu_4\text{-}S_2)_2(OC_6F_5)_2$ χ_m vs T plot.

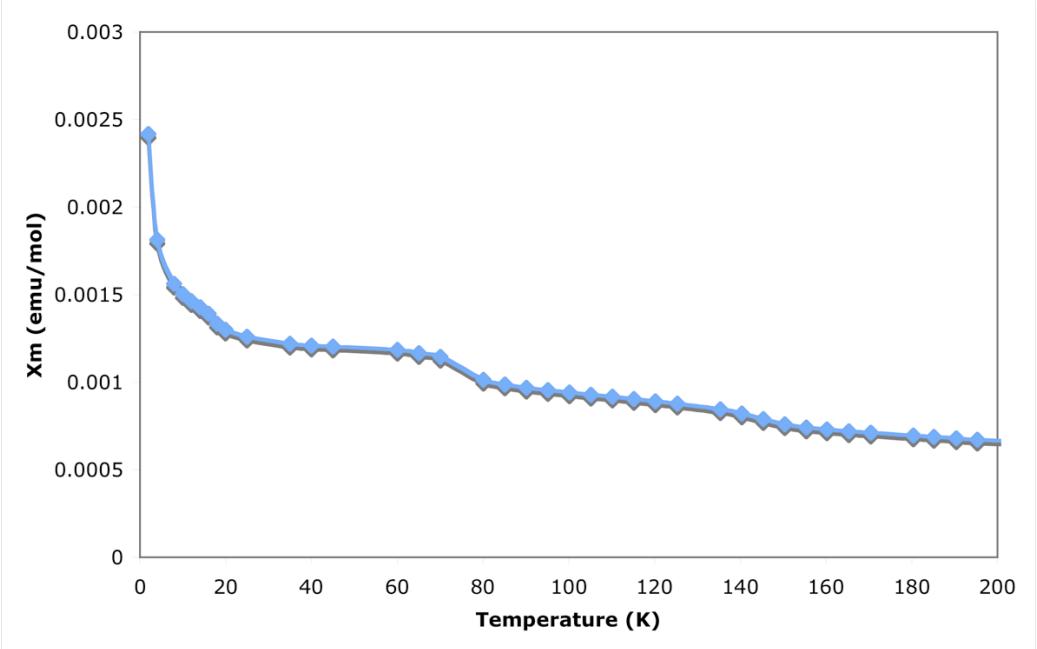

Figure 3.18. $(DME)_2Eu(SPh)_4(Na)_2$ χ_m vs T plot.

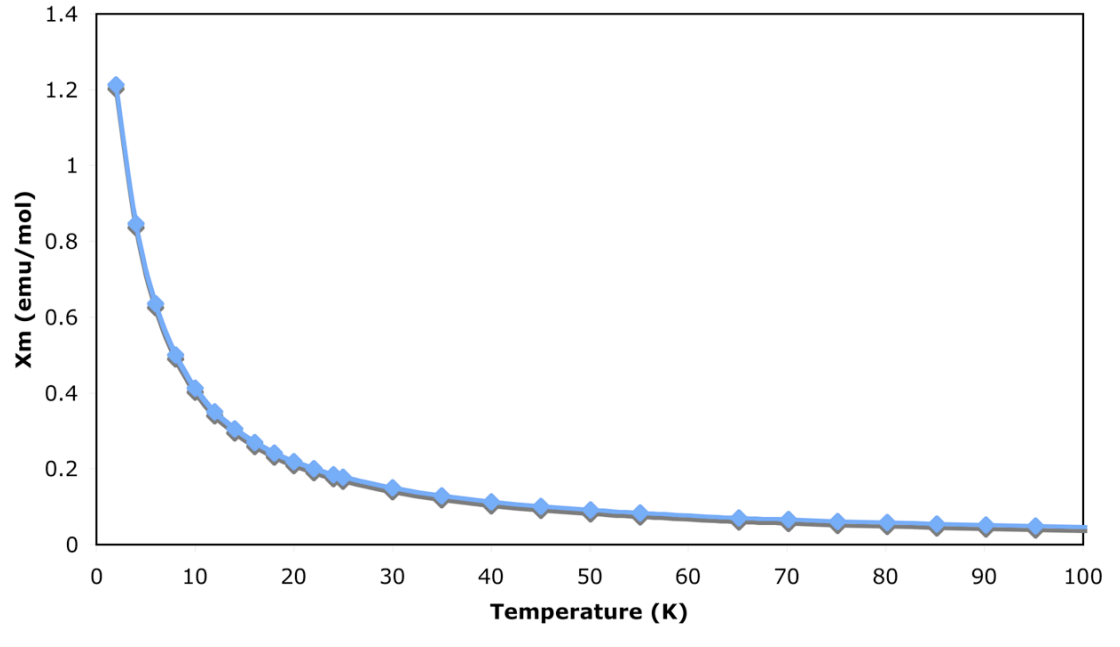

Figure 3.19. $(DME)_2Eu(SePh)_4(Na)_2$ χ_m vs T plot.

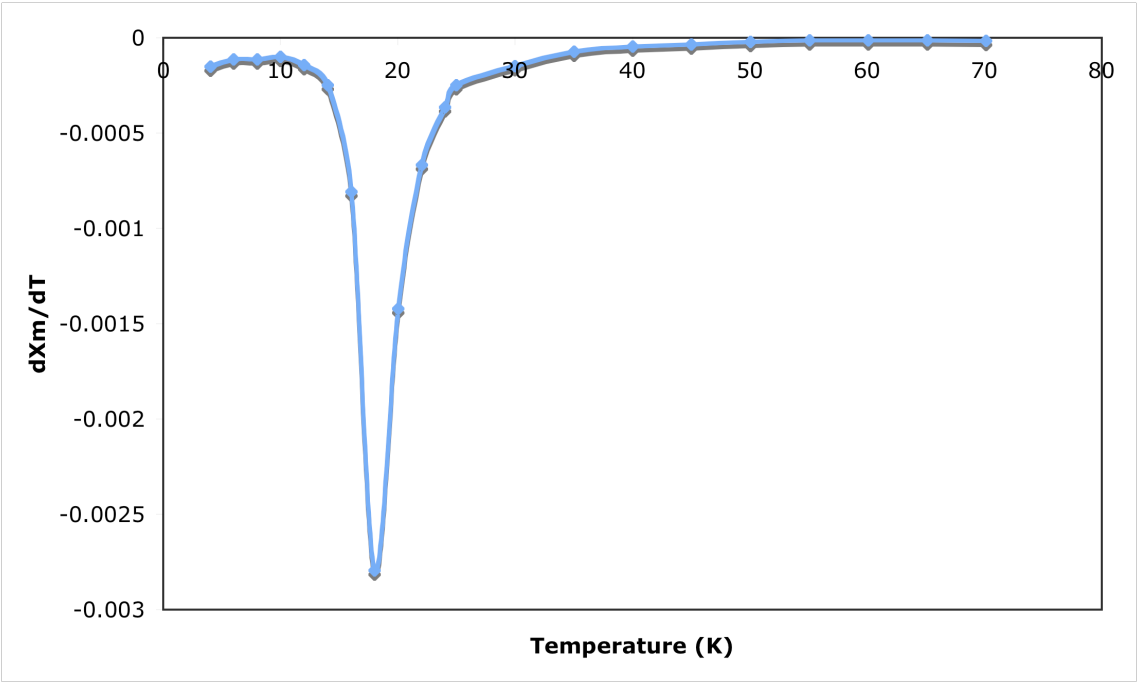

Figure 3.20. $(py)_6Eu_2(\mu_4\text{-}S_2)_2(OC_6F_5)_2$ (d χ_m/dT) vs T Plot.

Curie-Weiss (Inverse Chi ($1/\chi_m$) vs Temperature (T)) plots revealed unexpected antiferromagnetic magnetic interactions at higher temperatures. The $1/\chi_m$ values were plotted as a function of T from 50K to either 100K or 200K (Figures 3.21-3.23). The data was fit to a linear regression to determine the curie (C) and weiss constants (θ) for all three samples (table 3.4). The experimental weiss constants presented large negative numbers consistent with anti-ferromagnetic interactions for $(DME)_2Eu(SPh)_4(Na)_2$ and $(py)_6Eu_2(\mu_4\text{-}S_2)_2(OC_6F_5)_2$. These results deviated from expected behavior since Curie-Weiss law predicts paramagnetic ordering above the critical Curie or Neel temperatures in bulk EuS. The comparatively small value for $(DME)_2Eu(SePh)_4(Na)_2$ was in agreement with the localized paramagnetic ordering predicted by the M and $\chi_m T$ plots described above. All of the data fittings displayed sound agreement through their high R^2 values. The small C values (0.21, and 1.60) were more consistent with noninteracting Eu centers. The observed larger C value for $(py)_6Eu_2(\mu_4\text{-}S_2)_2(OC_6F_5)_2$ is explained by the difference in Eu per complex as the curie constant reflects the effective magnetic moment per formula unit.

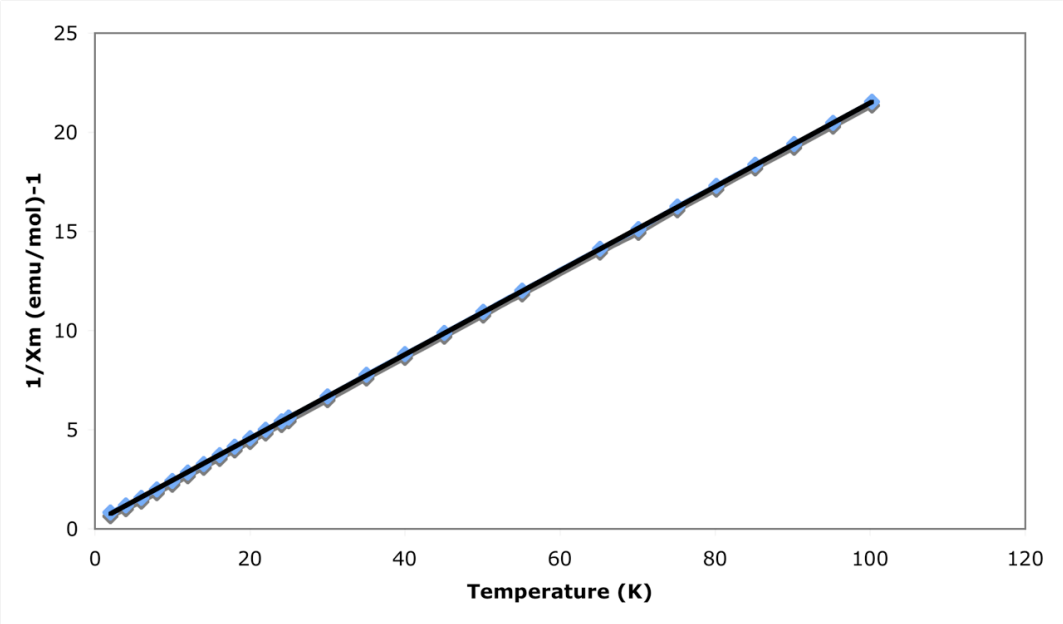

Figure 3.21. $(DME)_2Eu(SePh)_4(Na)_2$ Curie-Weiss Plot With Linear Regression Fitting.

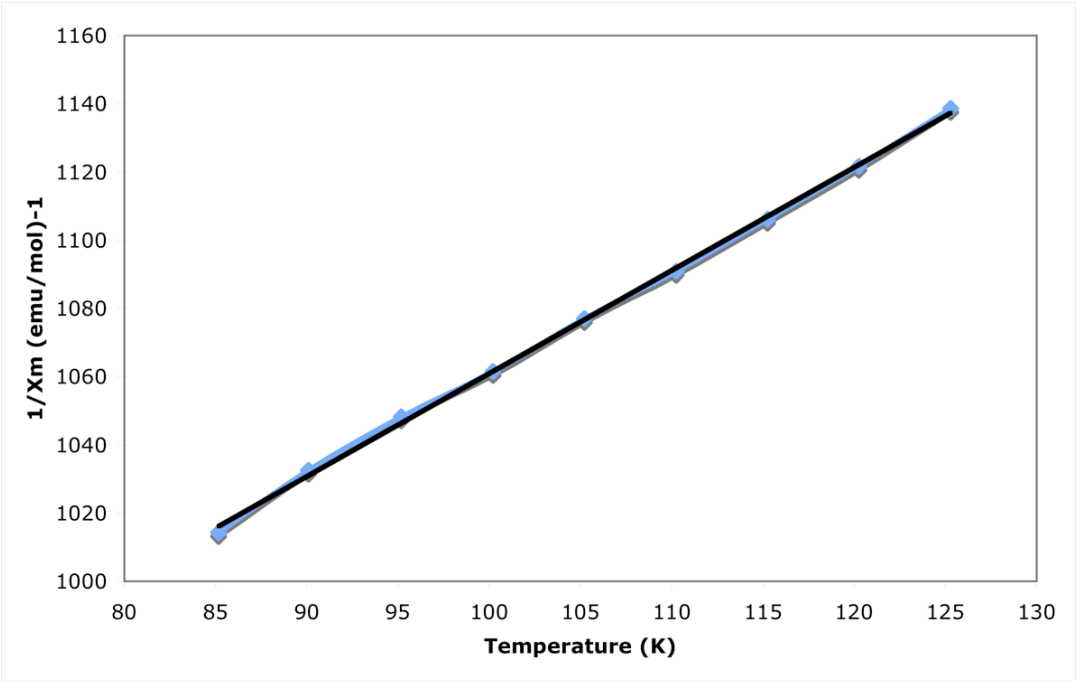

Figure 3.22. $(DME)_2Eu(SPh)_4(Na)_2$ Curie-Weiss Plot With Linear Regression Fitting.

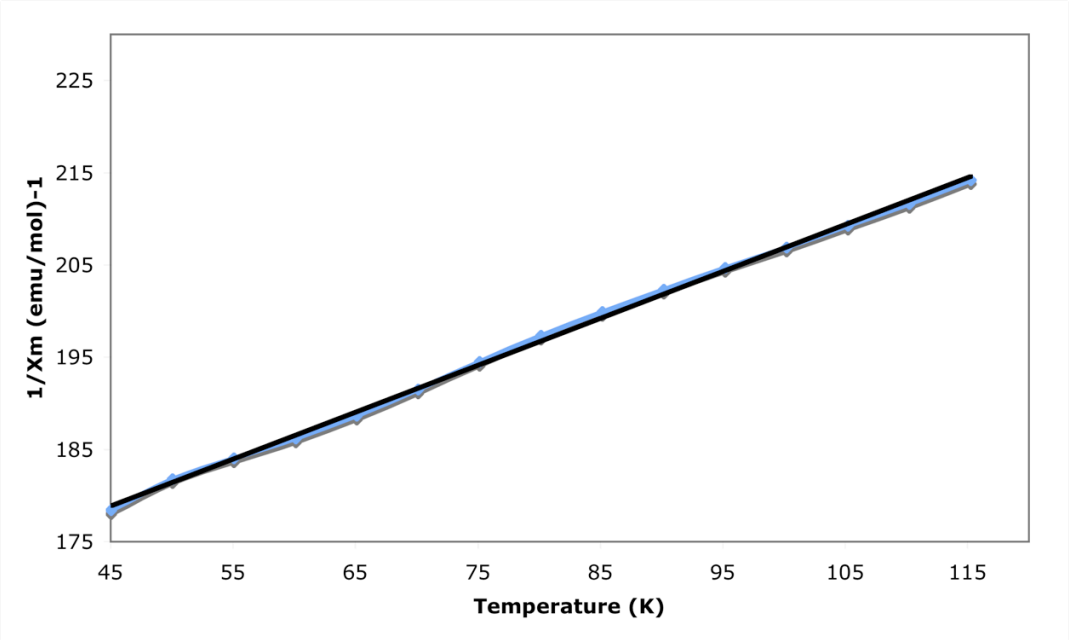

Figure 3.23. $(py)_6Eu_2(\mu_4\text{-}S_2)_2(OC_6F_5)_2$ Curie-Weiss Plot With Linear Regression Fitting.

Complex	Curie Constant (C)	R^2	Weiss Constant (θ)
$(DME)_2Eu(SePh)_4(Na)_2$	4.72	1.000	-1.56
$(DME)_2Eu(SPh)_4(Na)_2$	0.33	0.999	-251.17
$(py)_6Eu_2(\mu_4\text{-}S_2)_2(OC_6F_5)_2$	1.91	0.999	-307.15

Table 3.4. Summary of Curie-Weiss Plot Data.

The temperature related magnetic interactions of $(py)_6Eu_2(\mu_4\text{-}S_2)_2(OC_6F_5)_2$, and $(DME)_2Eu(EPh)_4(Na)_2$ undergird the position that EuE products magnetic profiles consist of two coupling mechanisms. Typically, low temperature magnetic ordering is associated with M coupling to conduction band electrons.[37] However, the determined curie constant (1.60) for $(py)_6Eu_2(\mu_4\text{-}S_2)_2(OC_6F_5)_2$ was well below expected values for an Eu^{3+} effective magnetic moment with a spin ground state

of S= 6/2, and a coupling to the disulfido conduction band electrons. This incongruency effectively eliminated the likelihood of a magnetic moment to conduction band coupling and may be the result of a tunneling mechanism. Similar mechanisms in EuS[38] and EuO[39] have been studied by Moodera and Mersevey in epitaxially grown thin films.

The presence of a second interaction mechanism is substantiated by the high weiss constants observed for all three compounds above 50K. Given the long Eu-Eu distances for, $(py)_6Eu_2(\mu_4\text{-}S_2)_2(OC_6F_5)_2$, $(DME)_2Eu(SPh)_4(Na)_2$ and $(DME)_2Eu(SePh)_4(Na)_2$ (3.718Å, 5.224 Å and 5.357 Å respectively) and the established poor 4f-4f overlap due to shielding effects between Eu-Eu neighbors, the superexchange mechanism for such ordering (via bridging thiolates and selenolates) becomes likely. Melman[40] and Woodruff[41] have detailed similar magnetic interactions for Eu^{2+} and [Li(thf)4][Ln4{N- (SiMe3)2}4(μ-SEt)8(μ4-SEt)], (Ln= Gd, Tb, Dy) clusters with related bridging motifs.

The ferrimagnetic ordering of Eu^{3+} at low temperature in $(Py)_6Eu_2(\mu_4\text{-}S_2)_2(OC_6F_5)_2$ also provides a sound support for the partial dependence of magnetic ordering on a ratio of Eu^{2+}/Eu^{3+} ions. This makes sense given the significant differences in ionic radii between Eu^{2+} (1.31-1.49 Å) and Eu^{3+} (1.08-1.26 Å) coordinated centers.[28] Extensions of lattice parameters and distortions of bond angles would be a natural outcome of mixed valence Eu. Anderson [42] related a similar viewpoint to the expression of magnetic ordering when he reported variances in ionic radii induced distortions in the Eu-E-Eu angles and the expression of ferro (90°) vs antiferromagnetic (76° and 140°) behaviors. This

relationship gains some justification by the near 110°, and 80° Eu-S-Eu angles found in $(DME)_2Eu(SPh)_4(Na)_2$ and $(py)_6Eu_2(\mu_4\text{-}S_2)_2(OC_6F_5)_2$ respectively. The Eu^{3+} ferrimagnetic results reported are also in slight contrast to the ferromagnetic ordering previously observed in $Eu^{2+}S$ (ref 36) and mixed valence EuS materials (Table 3.5).

Compound	Curie Constant (C)	Weiss Parameter (K)	effective magnetic moment (μ_b)	Curie Temperature (K)
$(DME)_2Eu(SePh)_4(Na)_2$	4.72	-1.56	6.12	------
$EuSe_2$	7.4	14	7.7	8
$(DME)_2Eu(SPh)_4(Na)_2$	0.33	-251.17	1.62	------
$(py)_6Eu_2(\mu_4\text{-}S_2)_2(OC_6F_5)_2$	1.91	-307.15	3.90	18.03
Na:EuS nanoparticles	------	(-248) - 25.09	7.39-4.3	12.6
Bulk EuS	7.14	18	7.59	16.6

Table 3.5. Comparison of Eu-S and Eu-Se Materials Magnetic Data.

The observed weiss parameters for $(DME)_2Eu(SPh)_4(Na)_2$ and $(py)_6Eu_2(\mu_4\text{-}S_2)_2(OC_6F_5)_2$ are within the range of values observed for EuS nanoparticles with various doping levels of sodium. Additionally the calculated 6.12 effective magnetic moment for $(DME)_2Eu(SePh)_4(Na)_2$ when compared to $EuSe_2$ is close to the 7.7 value, supporting the accuracy of the calculations. While the elevated curie temperature found for $(py)_6Eu_2(\mu_4\text{-}S_2)_2(OC_6F_5)_2$ deviates from the 16.6 value observed for bulk EuS its proximity to the bulk value does support valence

determined property shifts. Therefore, the influence of Eu^{3+} valence on magnetic ordering in EuE appears to be a delicate interplay between structurally related distortions of magnetic coupling mechanisms, and a competitive bulk expression of Eu^{2+} and Eu^{3+} magnetic orderings.

3.4 Conclusion

Two novel octahedral europium chalcogenolate complexes $(DME)_2Eu(SPh)_4(Na)_2$ and $(DME)_2Eu(SePh)_4(Na)_2$ have been isolated through a sodium azide directed pathway. Each posses a solid state like EuE coordination sphere free of solvent coordination and possessing a divalent core. Comparative magnetic susceptibility studies with the trivalent $(py)_6Eu_2(\mu_4\text{-}S_2)_2(OC_6F_5)_2$ revealed paramagnetic ordering at low temperatures, but a weak antiferromagnetic ordering above the bulk EuE Neel and Curie temperatures. Simultaneously, support for the influence of Eu^{3+} in expression of the documented magnetic ordering in bulk and nano EuE products was presented.

References

[1] Matthias, B. T.; Bozorth, R. M.; Van Vleck, J. H. *Phys. Rev. Lett.***1961**, 7, 160.

[2] Wan, X.; Dong, J.; Savrasov, S.Y. *Phys. Rev. B.* **2011**,83, 205201.

[3] Mauger, A.; Godart, C. *Phys. Rep.* **1986** 141, 51.

[4] Fert, A. *Rev. Mod. Phys.* **2008**, 80, 1517.

[5] Behin-Aein, B.; Datta, D.; Salahuddin, S.; Datta, S. *Nat. Nano.* **2010 ,** 5,4, 266.

[6] Duan, C.G.; Sabiryanov, R.F.; Liu, J.; Mei, W.N.; Dowben, P.A. ; Hardy, J.R. *Phys. Rev. Lett.* **2005**, 94, 237201.

[7] Schmehl A. et al. *Nat. Mater*. **2007,** 6, 882 .

[8] Regulacio, M.D.; Bussman, K.; Lewis, B.; Stoll, S.L. *J.Am.Chem.Soc* **2006**,128, 11174

[9] Thomson, W. *Proc. R. Soc. London Ser. A* **1857**, 8, 546.

[10] Baibich, M.N.; Broto, J.M.; Fert, A.; Dau, F.N.V.; Petroff, F. *Phys. Rev. Lett.* **1988**, 61, 2472.

[11] Binasch, G.; Grunberg, P.; saurenbach, F.; Zinn, W. *Phys. Rev. B.* **1989**, 39, 4828.

[12] Holtzberg, F.; von Molnar, S.; Coey, J. M. D. *Handb. Semicond.* **1980**, 3, 815.

[13] Wachter, T. *Crit. Rev. Solid State Sci.* **1972**, 3, 189.

[14] Esaki, L.; Stiles, P.J.; von Molnar, S. *Phys. Rev. Lett.* **1967**, 19, 852.

[15] Kittel, C. *Introduction to Solid State Physics, 8th ed.;* Wiley; New York , **2004**, 302.

[16] Ott, H.; Heise, S. J.; Sutarto, R.; Hu, Z.; Chang, C. F.; Hsieh, H. H.; Lin, H.-J.; Chen, C. T.; Tjeng, L. H. *Phys. Rev. B.* **2006**, 73, 099407.

[17] Kar, S.; Boncher, W. L.; Olszewski, D.; Dollahon, N.; Ash, R.; Stoll, S. L. *J. Am. Chem. Soc.* **2010,** 132, 13962.

[18] Wang, X.; Liu, P.; Fox, K.A.; Tang, J.; Colon Santana, J.A.; Belashchenko, K.; Dowben, P.A.; Sui, Y. *IEEE. Trans. Mag*. **2010**, 46. 1879.

[19] Methfessel, S.; Eastman, D. E.; Holtzberg, F.; Mcguire, T.R.; Penney, T.; Shafer, M. W.; von Molnar, S. *Colloque Inter. Terres Rares,* **1969**, 565.

[20] Kepa, H.; Majkrzak, C. F.; Sipatov, A.; Fedorov, A.G.; Samburskaya, T. A.; Giebultowicz, T. M. Cond. Matt. **2008**, 1.

[21] Eiselt, G.; Koetzler, J.; Maletta, H.; Binder, K.; Stauffer, D. *J. Magn. Magn. Mater.* **1979**, 13, 146.

[22] Kar, S.; Boncher, W.L.; Olszewski, D.; Dollahon, N.; Ash, R.; Stoll, S.L. *J. Am. Chem. Soc.* **2010,** 132, 13962.

[23] a)Echard, J.C. *Compt. Rend*. **1957**, 244, 3059. b) Shafer, M. W. *J. Appl. Phys*. **1965**, 36, 1145. c) Shafer, M. *Mater. Res. Bull*. **1972**, 7, 603. d) Kaldis, E *J. Cryst. Growth* **1968**, 3, 146.

[24] a) Chen, W.; Zhang, X.; Huang, Y. *Appl. Phys. Lett.* **2000**, 76, 2328. b) Tanaka, K.; Fujita, K.; Soga, N.; Qui, J.; Hirao, K. *J. Appl. Phys.***1997**, 82, 840. c) Hasegawa, Y.; Thongchant, S.; Wada, Y.; Tanaka, H.; Kawai, T.;Sakata, T.; Mori, H.; Shozo, Y. *Angew. Chem., Int. Ed*. **2002**, 42, 2073.

[25] Somarajan, S.; Harrison, M. A.; Koktysh, D. S.; He, W.; Hasan, S. A.; Park, J.-H.; Stillwell, R. L.; Payzant, E. A.; Dickerson, J. H. *Mater. Chem. Phys.* **2012**, 1.

[26] Holtzberg, F.; Francavilla, T. L.; Huang, C. Y.; Tholence, J. L. *J. Appl. Phys.* **1982**, 53, 2229.

[27] Berry, F. J.; Perry, D. L. *Hyper. Inter.* **1992**, 68, 245.

[28] Shannon, R.D. *Acta. Crysta.***1976**, A32, 752.

[29] Redigolo, M. L.; Koktysh, D. S.; Rosentahl, S. J.; Dickerson, J. H.; Gai, Z.; Gao, L.; Shen, J. *App. Phys. Lett.* **2006**, 89, 22250.

[30] Beradini, M.; Emge, T.; Brennan, J.G. *J. Am. Chem.Soc.* **1993**, 115, 8501.

[31] a)Berardini, M.; Lee, J.; Freedman, D.; Lee, J.; Emge, T. J.; Brennan, J. G. *Inorg. Chem.* **1997**, 36(25), 5772-5776. b) Brewer, M.; Khasnis, D.; Buretea, M.; Berardini, M.; Emge, T. J.; Brennan, J. G. *Inorg. Chem.* **1994**, 33, 2743. c) Lee, J.; Freedman, D.; Melman, J.H.; Brewer, M.; Sun, L.; Emge, T. J.; Long, F.H.; Brennan, J.G. *Inorg. Chem*. **1998**, 37, 2512

[32] Khasnis, D.V.; Brewer, M.; Lee, J.; Emge, T.J.; Brennan, J.G. *J. Am. Chem. Soc.* **1994**, 116, 7132.

[33] Viciano-Chumillas, M.; Tanase, S.; Jos de Jongh, L.; Reedjik, J; *Eur, J. Inorg. Chem.* **2010**, 3403.

[34] Choudhury, A.; Grandjean, F.; Long, G.J.; Dorhout, P.K. *Inorg. Chem*. **2012**, 51,11779.

[35] Aitken, J.A.; Cowen, J.A; Kanatzidis, M.G. *Chem. Mater.* **1998**, 10, 3928.

[36] Evenson, C.R.,IV; Dorhout, P. K. *Inorg. Chem.* **2001**, 40,10, 2409.

[37] Al'tshuler, T. S.; Goryunov, Y. V.; Dukhnenko, A. V.; Shitsevalova, N. Y. *JETP Lett* **2008**, 88, 224.

[38] Santos, T. S.;Moodera, J. S. *Phys. Rev. B.* **2004**, 69,24,241203

[39] Hao, X.; Moodera, J. S.; Meservey, R. *Phys. Rev. B* **1990**, 42, 8235.

[40] Melman, J. H. Molecules, clusters, and solid-state materials with lanthanide-sulfur bonds :synthesis, structure, and reactivity. Ph.D. Dissertation, Rutgers the State University of New Jersey, New Brunswick, NJ, **2004**.

[41] Woodruff, D.N.; Tuna, F.; Bodensteiner, M.; Winpenny, R. E. P.; Layfield, R. A. *Organometallics,* **2013,** Ahead of Print.

[42] Anderson, P. W. *Magnetism, Vol. 1*; New York, **1963**; pg 25-85.

Chapter 4: Experimental Section.

4.1 General Procedures

All syntheses were carried out under high purity nitrogen (WELCO Praxair) using conventional drybox or Schlenk techniques. Solvents (Aldrich) were purified with a dual column Solv-Tek Solvent Purification System. Lanthanide, Na, K, Li and Hg were all purchased from Strem. Cd was purchased from J.T. Baker. Elemental Se, Te, S, NaN_3, PhMgBr, NH_4Cl, Na_2So_4, DETA (Diethylenetriamine) and $[NO]PF_6$, were purchased from Aldrich. NaN_3 was dried under vacuum for 24hrs at room temperature before use. PhSSPh ,and PhSeSePh, was purchased from Acros while PhSeSePh was recrystallized from hexanes.PhTeTePh, was synthesized from a modified Grignard reaction and recrystallized in warm hexanes. Light sensitive conditions consisted of Night time reaction workups and wrapping each reaction in aluminum foil during all reaction stirrings, crystallizations and reagent additions. IR spectra were taken on a Thermo Nicolet Avatar 360 FTIR spectrometer and were recorded from 4000 to 600 cm^{-1} as a Nujol mull or solid powder on CsI plates. Electronic spectra were recorded on a Varian DMS 100S spectrometer with the samples in a 0.10 cm quartz cell attached to a Teflon stopcock. Single crystal XRD data was collected on a Bruker Smart APEX CCD diffractometer with graphite monochromatized Mo Kα radiation (λ = 0.71073 Å). All crystals were immersed in Paratone oil and examined at low temperature, except for crystals of Nd_{17} which was loaded in 1.0 mm glass capillaries at room temperature. The data was corrected for Lorenz effects , polarization, and absorption. The latter by a multi-scan (SADABS)3

method. The structures was solved by direct methods (SHELXS86). All non-hydrogen atoms were refined (SHELXL97)5 based upon F_{obs2}. All hydrogen atom coordinates were calculated with idealized geometries (SHELXL97). Scattering factors (fo, f', f") are as described in SHELXL97. Elemental analyses were performed by Quantitative Technologies, Inc. (Whitehouse Station, NJ). The dc magnetic susceptibility measurements were carried out on crystalline samples with a Quantum Design MPMS-XL superconducting quantum interference device (SQUID) magnetometer. Crystal samples were placed in a gelatin capsule fastened in a plastic straw for immersion into the SQUID. Typical field-cooling (FC) magnetization in the temperature range of 5-300 K was performed under external magnetic fields of 1 kOe. Absorption measurements were carried out with crystalline powder dissolved in THF using a double beam spectrophotometer (Perkin-Elmer Lambda 9, Wellesley, MA) in a 1 cm cuvette using THF as the reference solvent. The emission spectra of the crystalline samples were recorded by exciting the samples with the 800 nm band of a titanium-sapphire laser (Coherent, Inc., Santa Clara, CA) in the 90°-excitation geometry. The emission from the sample was focused onto a 0.55 m monochromator (Jobin Yvon, Triax 550, Edison, NJ) and detected by a thermoelectrically cooled InGaAs detector. The signal was intensified with a lock-in amplifier (SR 850 DSP, Stanford Research System, Sunnyvale, CA) and processed with a computer controlled by the Spectramax commercial software (GRAMS 32, Galactic Corp., Salem, NH). To measure the decay time, the laser beam was modulated by a chopper and the signal was collected on a digital oscilloscope (model 54520A, 500 MHz, Hewlett-

Packard, Palo Alto, CA). The spectroscopic measurements and calculations were performed by Dr. Ajith Kumar, Dr. Mei-Che Tan, Jesse Kohl and Dr. R. Riman from the Materials Science and Engineering Department at Rutgers University. Dc magnetic susceptibility measurements were performed by Dr. Yoon Seok Oh and Dr. Sang-Wook Cheong in collaboration with the Rutgers Center for Emergent Materials in the Department of Physics at Rutgers University and Dr. Kai Filsinger from the Greenblatt Group in the Department of Chemistry and Chemical Biology at Rutgers Unversity. XRD was performed by Dr. Thomas J. Emge from the Department of Chemistry and Chemical Biology at Rutgers University.

Synthesis of $(py)_{10}Sm_6O_2(N_3)_{16}Na_2$ scheme a.

Sm (160 mg, 1.06 mmol), Hg (39 mg, 0.19 mmol), and diphenyl diselenide (478 mg, 1.53 mmol) were combined in pyridine (30 mL) and the mixture was stirred for 24 hrs to give a clear light orange solution. undried sodium azide (132 mg, 2.10 mmol) was then added, the mixture was stirred for 3 days in a dark environment to give a yellow solution and a white precipitate. The solution was filtered, concentrated to 20 mL, and layered with hexanes (4 mL) in the dark to give hexagonal colorless crystals (46 mg, 8.3%) that become white and amorphous when removed from mother liquor, turn brown at 119ºC, and detonate at 295ºC. IR: (bridging azide) 2115 (w), (terminal) 2052 (m), cm-1 . Anal Calcd for $C_{125}H_{125}N_{73}Na_2O_2Sm_6$; C, 37.1(33.3); H, 3.12(2.5); N, 29.5(17.9). Found: C, 32.9; H, 2.31; N, 24.2.

Synthesis of $(py)_{10}Sm_6O_2(N_3)_{16}Na_2$ scheme b.

Sm (160 mg, 1.06 mmol), Hg (39 mg, 0.19 mmol), and diphenyl diselenide (478 mg, 1.53 mmol) were combined in pyridine (30 mL) and the mixture was stirred for 24 hrs to give a clear light orange solution. Sodium azide (137 mg, 2.10 mmol) and sodium oxide (63 mg, 1.01 mmol) were then added, the mixture was stirred for 3 days in a dark environment to give a yellow solution and a white precipitate. The solution was filtered, concentrated to 20 mL, and layered with hexanes (4 mL) in the dark to give hexagonal colorless crystals (46 mg, 8.3%) that become white and amorphous when removed from mother liquor, turn brown at 119ºC, and detonate at 295ºC. IR: (bridging azide) 2115 (w), (terminal) 2052 (m), cm-1 . Anal Calcd for $C_{100}H_{100}N_{68}Na_2O_2Sm_6$; C, 37.1 (33.1); H, 3.12 (2.77); N, 29.5 (23.5). Found: C, 32.9; H, 2.31; N, 24.2. (3 azides lost)

Synthesis of $(py)_{10}Ho_6O_2(N_3)_{12}(SePh)_2$.

Diphenyl diselenide (650 mg, 2.08 mmol), Hg (17 mg, 0.084 mmol), and Ho (333 mg, 2.01 mmol) were combined in pyridine (25 mL), and the mixture was stirred for 24 hours to give a dark brown clear solution with no visible metal. Sodium azide (65 mg, 1.05 mmol) and sodium oxide (68 mg, 1.10 mmol) were then added, and after stirring for 72 hrs the opaque reddish brown solution was filtered (20 mL), concentrated (18 mL) and layered with hexanes (3 mL) in the dark to give faint pinkish micro crystals. (251 mg, 33.8%) that become opaque when removed from solvent, and detonate at 310ºC. IR: (bridging azide) 2121

(w) , (terminal azide) 2053 (m) cm-1. Anal Calcd for $C_{102}H_{100}N_{54}Se_2O_2Ho_6$; C, 37.6 (36.4); H, 3.10 (2.93); N, 23.2 (20.3). Found: C, 36.7; H, 3.20; N, 20.6. (2 pyridines and 5 azides lost)

Synthesis of $(py)_{10}Er_6O_2(N_3)_{12}(SePh)_2$.

Diphenyl diselenide (630 mg, 2.01 mmol) and Hg (420 mg, 2.09 mmol) were combined in pyridine (40 mL) and the mixture was stirred for 24 hours to give a yellow clear solution. Er (178 mg, 1.06 mmol) was added and after 14 hrs sodium azide (how much) and sodium oxide (73 mg, 1.17 mmol) were added. After 2 days the opaque greenish grey mixture was filtered to give a yellow solution that was concentrated (10 mL) and layered with hexanes (3 mL) in the dark to produce faint purple crystals (90 mg, 15%), that degrade at 85ºC, further degrade at 270ºC and detonate at 336 ºC. IR: (bridging azide) 2125 (m), (terminal azide) 2054 (m) cm-1. Anal Calcd for $C_{102}H_{100}N_{54}Se_2O_2Er_6$; C, 37.4 (34.1); H, 3.08 (2.9); N, 23.1(17.3). Found: C, 34.5; H, 3.60; N, 17.5. (6 pyridines lost)

Synthesis of $(py)_{10}Er_6O_2(Se_2)_2(N_3)_{10}$.

Cd (110 mg, 2.09 mmol) and diphenyl diselenide (1300 mg, 4.16 mmol) were combined in pyridine (50 mL), while stirring for 24 hours to give a dark yellow clear solution. Er (167 mg, 1.00 mmol) & Hg (50 mg, 0.25mmol) were added to the solution and after stirring for 5 hours the dark yellow-green solution was filtered to remove a grey precipitate. Elemental Se (160 mg, 2.02 mmol),

sodium azide (65 mg, 1.05 mmol), and sodium oxide (63 mg, 1.01 mmol) were then added, and after two days the dark red solution was filtered to remove the yellow precipitate that had formed. Layering with hexanes in the dark gave pink-orange plates (60 mg, 4.2%) that flash and detonate at 312ºC. IR: (bridging azide) 2107 (m), (terminal azide) 2082 (m) (terminal azide) 2057 (w) cm-1. Anal Calcd for $C_{65}H_{65}N_{39}Se_5O_2Er_6$; C, 27.4 (25.3); H, 2.30 (2.12); N, 19.2 (16.0). Found: C, 26.6; H, 2.00; N, 16.3. (2 pyridines and 4 azides lost)

Synthesis of $(py)_{16}Sm_8SeO_4Na_2(TeTe)_6(N_3)_8$.

Hg (45 mg, 0.22 mmol) Sm (453 mg, 3.01 mmol) diphenyl diselenide (936 mg, 2.99 mmol) were combined in pyridine (30 mL) and allowed to stir for 12h. A dark blackish solution was observed. Elemental Te (516 mg, 4.04 mmol) and sodium azide (133 mg, 2.04 mmol) were added to the solution, which was wrapped in foil and stirred for 72 hrs to give a dark reddish orange solution. The solution was filtered in the dark and layered with hexanes (5 mL) to give dark red crystals, (0.10 g, 5.2%) that melt at 297 ºC. IR: (bridging azide) 2167 (w) , (bridging azide) 2100 (m), (terminal azide) 2066 (w) cm-1. Anal Calcd for $C_{120}H_{81}N_{39}Na_2O_2SeSm_6$; C, 28.1(22.2); H, 2.36(9.2); N, 12.8 (2.12). Found: C, 22.8; H, 3.22; N, 3.02. (5 pyridines and 1 azide lost)

Synthesis of $(py)_{16}Ce_{17}Se_{18}(SePh)_{16}Na$ Method A.

Ce (937 mg, 6.68 mmol), PhSeSePh (960 mg, 3.07 mmol), and Hg (23 mg, 0.11 mmol) (added to increase the rate of the reaction) were combined in pyridine (40 mL), and the mixture was stirred for 24 h to give a clear dark yellow solution with some visible metal (solution 1). NaN_3 (195 mg, 3 mmol), and Se (450 mg, 5.69 mmol) ,were added to the solution simultaneously and allowed to stir for 3 days wrapped in foil. The mixture was filtered, concentrated to 20 mL, and layered with hexanes (4 mL) to give reddish orange crystals (2.33 g, 17%) of 1 that turn brown at 220 °C, and melt between 290 and 295 °C. Anal. Calcd for $C_{176}H_{160}N_{16}Se_{34}NaCe_{17}$: C, 25.9(30.4); H, 1.96(2.37); N, 2.57(3.94); Na, 0.24 (0.26).Found: C, 26.2; H, 1.46; N, 3.37; Na, 0.26. UV-vis: λmax) 442 nm (ε) 250 M-1 cm-1). IR: 2853 (s), 2726 (w), 2359 (m), 2341(m), 2051(w), 1594 (w),1574 (w), 1462 (s), 1377(s), 1260 (m), 1217 (w), 1146 (w), 1065 (w), 1020 (w), 800 (m), 731 (m), 700 (m) cm^{-1}.

Synthesis of $(py)_{16}Ce_{17}Se_{18}(SePh)_{16}Na$ Method B.

Ce (937 mg, 6.68 mmol), PhSeSePh (960 mg, 3.07 mmol), and Hg (23 mg, 0.11 mmol) (added to increase the rate of the reaction) were combined in pyridine (40 mL), and the mixture was stirred for 24 h to give a clear dark yellow solution with some visible metal (solution 1). In a separate Schlenk flask, Na (68.9 mg, 2.99 mmol) and PhSeSePh (468 mg, 1.50 mmol) were combined in pyridine (30 mL) and allowed to stir for 24 h to give a clear yellow solution (solution 2). Selenium (490 mg, 6.20 mmol) was added to solution 1 and stirred

for 1 min, and then solution 2 was added to solution 1 and the mixture was stirred for 3 days. The mixture was filtered, concentrated to 20 mL, and layered with hexanes (4 mL) to give reddish orange crystals (2.33 g, 81%) of 1 that turn brown at 220 °C, and melt between 290 and 295 °C.

Synthesis of $(py)_{16}Pr_{17}Se_{18}(SePh)_{16}Na$ Method A.

Pr (940 mg, 6.70 mmol), Diphenyl Diselenide (960 mg, 3.07 mmol), and Hg (45 mg, 0.22 mmol) were combined in pyridine (45 mL), and were allowed to stir for 24 hours to give a dark yellow clear solution with some visible metal. Selenium (470 mg, 5.95 mmol) was added to the solution and stirred for 1 minute. Sodium azide (209 mg, 3.22 mmol) was then added producing a dark red opaque solution with grey precipitate which was allowed to stir for 3 days. The solution was filtered, concentrated to 30 mL and layered with hexanes (5 mL) to give yellow green crystals, (1.01g, 40.2%) that turn brown at 200 ºC, and melt between 216-220 ºC. IR: 2922 (s), 2720 (w), 2666 (w), 2059 (w), 1908 (w), 1594 (m), 1573 (m), 1462 (s), 1376 (s), 1298 (m), 1259 (m) , 1217 (m), 1147 (m), 1069 (m), 1015 (m), 936 (w), 888 (w), 803 (m), 731 (s) , 689 (m).

Synthesis of $(py)_{16}Pr_{17}Se_{18}(SePh)_{16}Na$ Method B.

Pr (940 mg, 6.70 mmol), PhSeSePh (960 mg, 3.07 mmol), and Hg (45 mg, 0.22 mmol) were combined in pyridine (45 mL), and were allowed to stir for 24 h to give a dark yellow clear solution with some visible metal (solution 1). In a separate Schlenk flask, Na (69 mg, 3.00 mmol) and PhSeSePh, (468 mg, 1.50

mmol) were combined in pyridine (30 mL) and allowed to stir for 24 h to give a clear yellow solution with no visible metal (solution 2). Selenium (470 mg, 5.95 mmol) was added to the solution and the mixture was stirred for 1 min. Solution 2 was then added to solution 1 and this mixture was stirred for 3 days. The solution was filtered, concentrated to 20 mL, and layered with hexanes (4 mL) to give yellow green crystals (2.02 g, 93%) that turn brown at 200 °C, and melt between 216 and 220 °C. Anal. Calcd for $C_{176}H_{160}N_{16}Se_{34}NaPr_{17}$: C, 25.9(30.4); H, 1.96 (2.36); N, 2.57(3.94); Na, 0.24(0.26). Found: C, 26.9; H, 2.31; N, 2.69; Na, 0.37. UV-vis: λmax) 600 (ε) 6.7 M^{-1} cm^{-1}), 496, 455 nm. IR: 2922 (s), 2720 (w), 2666 (w), 2059 (w), 1908 (w), 1594 (m), 1573 (m), 1462 (s), 1376 (s), 1298 (m), 1259 (m), 1217 (m), 1147 (m), 1069 (m), 1015 (m), 936 (w), 888 (w), 803 (m), 731 (s), 689 (m) cm-1. Unit cell data (Mo KR, 100K): a) 22.60(2) Å, b) 42.11(3) Å, c) 31.10(2) Å,) 108.58(5)°, V) 28059(46) $Å^3$.

Synthesis of $(py)_{16}Nd_{17}Se_{18}(SePh)_{16}Na$ Method A.

Nd (960 mg, 6.65 mmol), Diphenyl Diselenide (963 mg, 3.08 mmol), and Hg (30 mg, 0.15 mmol) were combined in Pyridine (40mL), and were allowed to stir for 24 hours to give a dark green clear solution with some visible metal. Selenium (450 mg, 5.69 mmol) was added to the solution and stirred for 5 minutes. sodium azide (195 mg, 3 mmol) was then added producing a dark green opaque solution with grey precipitate which was allowed to stir for 3 days. The solution was filtered, and concentrated (20 mL) and layered with Hexanes (4 mL) to give light green crystals, (.906 g, 36%) that rapidly lose crystallinity

once removed from solution and becomes a green amorphous solid that turns brown between 216-219 ºC, and does not melt. IR: 2954 (s), 2925 (s), 2853 (s), 1576 (w), 1459 (m), 1376 (m), 1260 (m), 1091(m), 1020 (m), 799 (m), 700 (m).

Synthesis of $(py)_{16}Nd_{17}Se_{18}(SePh)_{16}Na$ Method B.

Nd (960 mg, 6.65 mmol), PhSeSePh (963 mg, 3.08 mmol), and Hg (30 mg, 0.15 mmol) were combined in pyridine (40 mL), and the mixture was allowed to stir for 24 h to give a dark green clear solution with some visible metal (solution 1). In a separate Schlenk flask, Na (69 mg, 3.00 mmol) and PhSeSePh, (468 mg, 1.50 mmol) were combined in pyridine (30 mL) and allowed to stir for 24 h to give a clear yellow solution with no visible metal (solution 2). Selenium (450 mg, 5.69 mmol) was added to solution 1 and the mixture was stirred for 5 min. Solution 2 was then added to solution 1 and this was stirred for 3 days. The combined solution was filtered, concentrated to 20 mL, and layered with hexanes (4 mL) to give light green crystals (2.03 g, 76%) that turn brown between 216 and 219 °C, and do not melt. Anal. Calcd for $C_{176}H_{160}N_{16}Se_{34}NaNd_{17}$: C, 25.7(30.2); H, 1.95(2.35); N, 2.55(3.92); Na, 0.24(0.26). Found: C, 29.9; H, 1.97; N, 3.67; Na, 0.15. IR: 2954 (s), 2925 (s) cm^{-1}.

Synthesis of $Eu(SPh)_4(Na)_2$•2DME.

Eu (302 mg, 2 mmol) PhSSPh (438 mg, 4.01 mmol), and Hg (23 mg, 0.11 mmol) were combined in DME (45 mL) and allowed to stir for 24 hrs to give a bright yellow solution with yellow precipitate. Dry NaN_3 (267 mg, 4.05 mmol) was added

to the opaque yellow solution wrapped in foil and allowed to stir at room temperature for 3 days. The solution was allowed to stand for 3 hrs to foster phase separation. The solution was filtered, concentrated and layered with hexanes to produce brown orange crystals (0.13 g, 8.0%) that become colorless at 120 °C turn dark brown at 295 °C and do not melt up to 350 °C. Anal Calcd. $C_{32}H_{40}EuNa_2O_4S_4$: C, 47.6; H, 4.9; N, 0.0; . Found: C, 47.62; H, 4.63; N, 0.30; IR: 3752 (w), 3702 (w), 2962.76 (s), 2903 (w), 2851 (m), 2658.21 (m), 2499.14 (m), 2359.81(m), 2341.37 (m), 2053.03(w), 2008.07(w), 1944.02 (w), 1412.42 (m), 1260.70 (s), 1091.43 (s), 1019.68 (s), 861.63 (m), 797.69(s), 685.31(m), 474.24 (m) cm^{-1}.

Synthesis of $Eu(SePh)_4(Na)_2$•2DME.

Eu (307 mg, 2.03 mmol) PhSeSePh (624 mg, 4 mmol), and Hg (27 mg, 0.13 mmol) were combined in DME (45 mL) and allowed to stir for 24 hrs to give a bright yellow solution with yellow precipitate. Dry NaN_3 (139 mg, 2.10 mmol) was added to the opaque solution wrapped in foil and allowed to stir at room temperature for 3 days. The solution was allowed to stand for 3 hrs to foster phase separation. The solution was filtered, concentrated and layered with hexanes to produce yellow orange crystals (0.27 g, 13%) that turn light brown at 110 °C turn dark red at 250 °C and become dark red/black in color at 350 °C but do not melt. Anal Calcd. for $C_{32}H_{40}EuNa_2O_4Se_4$: C, 38.3; H, 4.0; N, 0.0; . Found: C, 38.58; H, 3.74; N, 0.14; IR: 3741 (m), 3320.2 (w), 2962.47 (m), 2903 (m),

2809.06 (m), 2661.21 (m), 2498.37 (m), 2124.64 (w), 2049.94 (m),1944.52 (m), 1599.04 (w), 1260.70 (s), 1018.82 (w), 798.87 (s), 684.15 (s) cm^{-1}.

Synthesis of $[Sm_3(SePh)_4(N_3)THF_4]_3$.

Hg (36 mg, 0.18 mmol) Sm (148 mg, 0.99 mmol) Er (173 mg, 1.03 mmol) PhSeSePh (780 mg, 5 mmol) were combined in pyridine (25 mL) and allowed to stir for 24 hrs to produce an opaque green solution. NaN_3 (66 mg, 1 mmol) was added, the solution was wrapped in foil and allowed to stir for 4 days. The reaction was cooled to -10 °C and 10 ml of a 0.05M Iodine solution in pyridine was added via cannulla. Solution became light brown to yellow in color after addition. Solution was allowed to stir for another 6 days wrapped in foil. The dark reddish orange solution was filtered and concentrated and layered with hexanes and placed in the dark to crystallize reddish orange block crystals.

Synthesis of $Na_2(SePh)_2THF$.

Hg (24 mg, 0.18 mmol) Sm (150 mg, 1 mmol) PhSeSePh (156 mg, 1 mmol) and NaN_3 (195 mg, 3 mmol) were combined in THF (30 mL) and allowed to stir for 24 hrs to produce a dark green/blue solution. reaction was filtered, concentrated (15 mL) and layered with diethyl ether 2:1 to produce colorless rod crystals.

Reaction of Sm + PhSeSePh + Li_3N in Pyridine.

Hg (20 mg, 0.18 mmol), Sm (150 mg, 1 mmol), and PhSeSePh (468 mg, 3 mmol) were combined in pyridine (20 mL) and allowed to stir for 24 hrs. Li_3N (34 mg, 1 mmol) was added to a dark orange solution, that began to evolve gas immediately, and was allowed to stir for 24 hrs. wrapped in foil. Under light sensitive conditions, a dark purple solution that becomes brown with prolonged light exposure was filtered, concentrated (15 mL) and layered with hexanes in a 2:1 ratio. Dark purple precipitate was recovered.

Reaction of Sm + PhSeSePh + Li_3N in DME.

Hg (20 mg, 0.18 mmol), Sm (150 mg, 1 mmol) and PhSeSePh (468 mg, 3 mmol) were combined in DME (40 mL) and allowed to stir for 24hrs. Li_3N (50 mg, 1.43 mmol) was added to a dark green solution, and was allowed to stir for 24 hrs. wrapped in foil. Under light sensitive conditions, the yellow solution and dark green precipitate was filtered, concentrated (25 mL) and layered with diethyl ether(10 ml). An orange precipitate was isolated.

Reaction of Er + PhSeSePh + Li_3N + Se in Pyridine.

Hg (20 mg, .18 mmol), Er (335 mg, 1 mmol), PhSeSePh (313mg, 1mmol) and Li_3N (34 mg, 1 mmol) were combined in pyridine (30 mL) and allowed to stir for 24 hrs. Se (312 mg, 3.95 mmol) was added to the dark brown solution, and allowed to stir for 3 days wrapped in foil. The resulting purple solution was

filtered, concentrated (25 mL) and layered with hexanes (3 mL) under light sensitive conditions. Dark brown precipitate was isolated.

Reaction of Sm + PhSeSePh+ AlN in Pyridine.

Hg (30 mg, 0.18 mmol), Sm (150 mg, 1 mmol) and PhSeSePh (313 mg, 1 mmol) were combined in pyridine (20 ml) and allowed to stir for 24 hrs. AlN (127 mg, 3 mmol) was added to an orange solution, and the combined reaction was allowed to stir for 3 days wrapped in foil. The orange solution and white precipitate was placed in a 100 °C oil bath for 36 hrs. the reaction was filtered, concentrated (10 mL) and allowed to crystallize at -10 °C. White precipitate was recovered.

Reaction of Sm + PhSeSePh+ Ca_3N_2 in Pyridine.

Hg (30 mg, 0.18 mmol), Sm (150 mg, 1 mmol) and PhSeSePh (468 mg, 3.5 mmol) were combined in pyridine (20 mL) and allowed to stir for 24 hrs. Ca_3N_2 (148 mg, 1 mmol) was added to an orange solution,(with no gas evolution) wrapped in foil and allowed to stir for another 24 hrs. Solution was placed in 80 °C oil bath for 36 hrs and under light sensitive conditions, the dark red solution was filtered (12 mL), layered with hexanes (8 mL) and place in a cabinet to crystallize. Dark red precipitate was recovered .

Reaction of Sm + PhSeSePh+ Ca_3N_2 in THF.

Hg (30 mg, 0.18 mmol), Sm (150 mg, 1 mmol) and PhSeSePh (468 mg, 3.5 mmol) were combined in THF (20 mL) and allowed to stir for 24 hrs. Ca_3N_2 (148 mg, 1 mmol) was added to an orange solution, wrapped in foil and allowed to stir for 24 hrs. Solution was placed in 80 °C oil bath for 36 hrs under light sensitive conditions. The dark red solution with tan precipitate was filtered and concentrated (11 mL) (filtrate became cloudy rapidly after filtering). Reaction was layered with hexanes (8 mL) and place in a cabinet to crystallize. Dark red precipitate was recovered. Dark reddish crystals were isolated and determined to be samarium selenolate dimers.

Reaction of ErI_3 + Sr_3N_2 +DETA in THF

ErI_3 (401 mg, 0.73 mmol), Sr_3N_2 (316 mg, 1.08 mmol), and PhSeSePh (468 mg, 3.5 mmol) were combined in THF(25 mL) and allowed to stir for 24hrs. DETA (0.5 mL ,4.62 mmol) was added drop wise to the stirring green opaque solution , placed in a 60 °C oil bath and allowed to stir for 24 hrs. The reddish brown clear solution with aquamarine precipitate was allowed to stand filtered and placed in -10 °C freezer to crystallize. Aquamarine precipitate was recovered.

Reaction of $Er(SePh)_3$ + Sr_3N_2 +DETA in THF

Hg (30 mg, 0.18 mmol), Er (503 mg, 3 mmol) and PhSeSePh (1403 mg, 3.5 mmol) were combined in THF (25 mL) and allowed to stir for 24 hrs. Sr_3N_2

(316 mg, 1.08 mmol) and allowed to stir for 6 days. DETA (0.5 mL, 4.62 mmol) was added drop wise to the solution, which became purple. reaction was wrapped in foil and allowed to stir overnight. A dark reddish brown solution was observed. placed in a 60 °C oil bath and allowed to stir for 24 hrs. The reddish brown clear solution with was allowed to stand, filtered and concentrated (15 mL) . Small reddish crystal like structures that did not diffract were obtained after 10 days.

Reaction of Sm + P_5Ph_5 + in Pyridine.

Sm (923 mg, 1 mmol) and P_5Ph_5 (1,023 mg, 2 mmol) were combined in pyridine (50 ml) and allowed to stir for 4 days while wrapped in foil. The opaque pea green colored solution with grey precipitate was filtered and concentrated (20 mL) layered with diethyl ether (10 mL) and allowed to crystallize. Green precipitate was isolated.

Reaction of Sm + PhSeSePh + $[NO]PF_6$ in CH_3CN.

Hg(30 mg, 0.18 mmol), Sm (458 mg, 3.2 mmol) and PhSeSePh (938 mg, 2 mmol) were combined in CH_3CN (20 mL) **(A)** and in a seperate schlenk flask $[NO]PF_6$ was combined with CH_3CN (10 mL) **(B)**. Both solutions were allowed to stir for 48hrs. **A** (greenish/yellow, with copious grey precipitate) was refiltered into a new flask and placed in a stirring dry ice/acetone bath. **B** was added dropwise to stirring A over 45 minutes. Reaction was allowed to come to room

temperature, filtered, concentrated (15 mL) and layered with hexanes (10 mL). Grey precipitate, and diphenyl diselenide were isolated.

Reaction of Nd + PhSeSePh + Se + K(SePh) in Pyridine.

Nd (960 mg, 6.65 mmol), PhSeSePh (936 mg, 3.00 mmol), and Hg (30 mg, 0.15 mmol) were combined in pyridine (40 mL), and the mixture was allowed to stir for 24 hr to give a dark green clear solution with some visible metal (solution 1). In a separate Schlenk flask, Ca (130 mg, 3.00 mmol) and PhSeSePh (468 mg, 1.50 mmol) were combined in pyridine (30 mL) and allowed to stir for 24 h to give a clear yellow solution with no visible metal (solution 2). Selenium (450 mg, 5.69 mmol) was added to solution 1 and the mixture was stirred for 5 min. Solution 2 was then added to solution 1 and this was stirred for 3 days. The combined solution was filtered, concentrated to 20 mL, and layered with hexanes. $(py)_8Nd_8Se_6(SePh)_{12}$ was isolated and identified by unit cell.

Reaction of Nd + PhSeSePh + Se + $Ca(SePh)_2$ in Pyridine.

Nd (960 mg, 6.65 mmol), PhSeSePh (963 mg, 3.08 mmol), and Hg (40 mg, 0.20 mmol) were combined in pyridine (40 mL), and the mixture was allowed to stir for 24 h to give a dark green clear solution with some visible metal (solution 1). In a separate Schlenk flask, Ca (130 mg, 3.24 mmol) and PhSeSePh (468 mg, 1.50 mmol) were combined in pyridine (30 mL) and allowed to stir for 24 hrs to give a clear yellow solution with no visible metal (solution 2). Selenium (460 mg, 5.82 mmol) was added to solution 1 and the mixture was stirred for 5 min. Solution 2

was then added to solution 1 and this was stirred for 3 days. The combined solution was filtered, concentrated to 20 mL, and layered with hexanes. $(py)_8Nd_8Se_6(SePh)_{12}$ was isolated and identified by unit cell.

Reaction of Nd + PhSeSePh + Se + $Mg(SePh)_2$ in Pyridine.

Nd (960 mg, 6.65 mmol), PhSeSePh (963 mg, 3.08 mmol), and Hg (40 mg, 0.20 mmol) were combined in pyridine (40 mL), and the mixture was allowed to stir for 24 h to give a dark green clear solution with some visible metal (solution 1). In a separate Schlenk flask, Mg (75 mg, 3.08 mmol) and PhSeSePh, (940 mg, 11.89 mmol) were combined in pyridine (30 mL) and allowed to stir for 24 h to give a clear yellow solution with no visible metal (solution 2). Selenium (460 mg, 5.82 mmol) was added to solution 1 and the mixture was stirred for 5 min. Solution 2 was then added to solution 1 and this was stirred for 3 days. The combined solution was filtered, concentrated to 20 mL, and layered with hexanes. $(py)_8Nd_8Se_6(SePh)_{12}$ was isolated and identified by unit cell..

Reaction of Gd + Eu + PhSSPh + NaN_3 + S + Pyridine

Eu (165 mg, 1.08 mmol), Gd (473 mg, 3.00 mmol) PhSeSePh (963 mg, 3.08 mmol), and Hg (23 mg, 0.20 mmol) were combined in pyridine (40 mL), and the mixture was allowed to stir for 24 h to produce a reddish orange clear solution. NaN_3 and S were added wrapped in foil and allowed to stir for 3 days. The reaction was filtered concentrated (30 mL) and layered with hexanes (20 mL) and

allowed to crystallize at -10 °C to yield red plate crystals, $Gd_{8-x}Eu_xSe_6$ confirmed by unit cell and color.

Brian Freeman Moore

Education

Doctor of Philosophy, Inorganic Chemistry
Rutgers University, Piscataway NJ, May 2013

Post Baccalaureate Study, Chemistry Minor in Physics
La Salle University, Philadelphia PA, May 2007

Bachelor of Science, Psychology/ Africana Studies
Morehouse College, Atlanta GA, May 2001

Research Experience

Graduate Research Assistant, Department of Chemistry & Chemical Biology
Rutgers University, Piscataway, NJ August 2007- December 2012

Visiting Scientist, National Centre for Nanostructured Materials
CSIR, Brummeria – Pretoria, South Africa February 2011- June 2011

Research Consultant, Salene Technologies; South Africa
Rutgers University, Piscataway, NJ August 2010- November 2010

Summer Research Assistant, Department of Chemistry
La Salle University, Philadelphia, PA May 2006- May 2007

Teaching Experience

Teaching Assistant, Department of Chemistry & Chemical Biology
Rutgers University, Piscataway, NJ August 2007- May 2008

Teaching Assistant, Department of Chemistry
La Salle University, Philadelphia, PA August 2005- May 2007

Publications

Moore, B.F.; Emge, T.J.; Brennan, J.G.; Lanthanide Clusters with Azide Capping Ligands. *Inorganic Chemistry,* 2013, In Press.

Moore, B.F.; Kumar, G.A.; Tan, M.C.; Kohl, J.; Riman, R.E.; Brik, M.G.; Emge, T.J.;Brennan, J.G.; Lanthanide Clusters with Chalcogen Encapsulated Ln: Near IR Emission from Nanoscale $NdSe_x$. *Journal of The American Chemical Society,* 2011, 133(2), 373-378

Kornienko, A.; Moore, B.F.; Kumar, G.A.; Tan, M.C.; Riman, R.E.; Brik, M.G.; Emge, T.J.;Brennan, J.G.; Highly NIR Emissive Lanthanide Polyselenides. *Inorganic Chemistry*, 2011, 50(18), 9184-9190

Emge, T.J.;Romanelli, M.D.; Moore, B.F.;Brennan, J.G.; Zinc, Cadmium and Mercury Complexes with fluorinated Selenolate Ligands, *Inorganic Chemistry*, 2010, 49(16), 7304-7312.